A pursuit of Fast Radio Transients with the UTMOST and Parkes radio telescopes

Manisha Pranati Caleb

A thesis submitted for the degree of Doctor of Philosophy
of The Australian National University

January 2017

Research School of Astronomy and Astrophysics
The Australian National University
Canberra ACT 0200
Australia

"So the universe is not quite as you thought it was. You'd better rearrange your beliefs, then. Because you certainly can't rearrange the universe."

Isaac Asimov

Declaration

The work presented in this thesis was carried out in the Research School of Astronomy and Astrophysics at the Australian National University under the supervision of Prof. Franklin H. Briggs and Prof. Brian P. Schmidt and as a visitor to the Swinburne University of Technology, under the supervision of Prof. Matthew Bailes and Dr. Chris Flynn, between 2013 and 2016. This thesis contains no material that has been accepted for the award of any other degree or diploma. To the best of my knowledge, this thesis contains no material previously published or written by another author, except where due reference is made in the text of the thesis. The content of the chapters listed below has appeared in refereed journals. Minor alterations have been made to the published papers in order to maintain argument continuity and consistency of spelling and style.

- Chapter 4 has been published in The Monthly Notices of the Royal Astronomical Society as **Caleb, M.**, Flynn, C., Bailes, M., Barr, E. D., Hunstead, R. W., Keane, E. F., Ravi, V., van Straten, W., 2016, *Are the distributions of Fast Radio Burst properties consistent with a cosmological population?*, MNRAS, 458, 708-717.

  The codes for the simulations and analysis described in this paper were written by the candidate in collaboration with supervisor Dr. Chris Flynn. The candidate performed all the scientific analyses of the simulations and the comparison of simulations with observational data. The paper was written entirely by the candidate, with suggestions from co-authors.

- Chapter 5 has been published in The Monthly Notices of the Royal Astronomical Society as **Caleb, M.**; Flynn, C.; Bailes, M, Barr, E. D., Bateman, T., Bhandari, S., Campbell-Wilson, D., Green, A. J., Hunstead, R. W., Jameson, A., Jankowski, F., Keane, E. F., Ravi, V., van Straten, W., Krishnan, V. Venkataraman, 2016, *Fast transient searches with UTMOST at 843 MHz*, MNRAS, 458, 718-725.

  The data were taken using the UTMOST telescope by the UTMOST collaboration, in which the candidate is a full member. All the data were processed using the offline single pulse search pipeline designed by the candidate. All the data reduction and scientific analyses were performed by the candidate. The corresponding papers were written entirely by the candidate with suggestions from co-authors.

- Chapter 6 has been published in The Monthly Notices of the Royal Astronomical Society as **Caleb, M.**, Flynn, C., Bailes, M., Barr, E. D., Bateman, T., Bhandari,

S., Campbell-Wilson, D., Farah, W., Green, A. J., Hunstead, R. W., Jameson, A., Jankowski, F., Keane, E. F., Parthasarathy, A., Ravi, V., Rosado, P. A., van Straten, W., Venkatraman Krishnan, V., 2017, *The first interferometric detections of Fast Radio bursts*, MNRAS, 468, 3746-3756.

The data presented were taken using the UTMOST telescope by the UTMOST collaboration, in which the candidate is a full member. The three FRB discoveries were made using the offline single pulse search pipeline designed by the candidate. All the data reduction and scientific analyses were performed by the candidate. The corresponding papers were written entirely by the candidate with suggestions from co-authors.

The candidate also made contributions to the following articles during the course of the candidature:

- Petroff, E., Bailes, M., Barr, E. D., et al. 2015a, MNRAS, 447, 246
- Petroff, E., Johnston, S., Keane, E. F., et al. 2015b, MNRAS, 454, 457
- Keane, E. F., Johnston, S., Bhandari, S., et al. 2016, Nature, 530, 453
- Ravi, V., Shannon, R. M., Bailes, M., et al. 2016, Science, 354, 1249
- Petroff, E., Burke-Spolaor, S., Keane, E. F., et al. 2017, MNRAS, 469, 4465
- Keane, E. F., Barr, E. D., Jameson, A., et al. 2017, ArXiv e-prints
- Bailes, M., Jameson, A., Flynn, C., et al. submitted, PASA.
- Bhandari, S., Keane, E. F., Barr, E. D., et al. *in preparation.*

These articles do not form a part of this thesis.

Manisha Pranati Caleb
January 2017

Acknowledgments

This thesis would not have been possible without the help and support from several people. I would like to thank the ANU and the RSAA for supporting me in pursuing a collaborative PhD. I would like to thank my supervisors, Matthew Bailes, Chris Flynn, Frank Briggs and advisor Brian Schmidt. Matthew, for introducing me to the exciting fast radio bursts and being an inspiration. You motivated me and made me believe. Chris, you have been a mentor and a supervisor. Words cannot express how deeply grateful I am for all your help and advice. You taught me that there are absolutely no silly questions. I will always cherish the countless student trips to Molonglo in the Molonglo mobile. I dedicate the first fast radio burst to you. Frank, for introducing me to Matthew and being a source of constant support. You have been instrumental in me being able to pursue a collaborative PhD. Brian, for believing in me and standing by me throughout my PhD. I would like to thank the Centre for Astrophysics and Supercomputing at Swinburne for making me feel included. A special thanks to the staff onsite at the Molonglo Observatory and to the pulsar group at Swinburne for welcoming me as one of their own. Emily, Ewan, Evan, AJ, Willem, Fabian, Pablo, Adam, Vikram, Ian, Stefan, Shivani, Vivek, Aditya, Wael, Jamie, Renee, Kathryn - you've been absolutely brilliant to work with.

Willem - most of my polarisation knowledge is because of you. Not to mention that my PhD would have not have been the same without PSRCHIVE. Thank you! Evan - thanks for being there when I've needed someone to talk to. It means a lot to me. AJ - none of this would have been possible without all the effort and hard work you've put in, to keep the backend going. You're a star! Shivani - thanks for being there when I ran into hurdles and for covering my observing slots at short notice. Not to mention the long spice chai latte walks. You kept me going! Vivek - you've been exceptional when I needed someone to bounce ideas off, run to for coding problems and when I've just been plain homesick for good South Indian food. You're the best! Aditya - thank you for the lighter moments in the office and the long movie marathons at home. You made things more fun. George - my PhD would not have been the same without your ukelele playing, Greek salads, jokes, and rants about how great Canada is. You're the man! I owe the beginning of my fascination with pulsars to Roberto, Desh and Wasim. Roberto, you were a friend and supervisor and I learned so much from you on the drives from the Mullard Space Science Lab to Guildford station. Thank you! Desh, you played an integral part in and inspired me to pursue a PhD in radio astronomy. You taught me that anything can be explained in simple terms. Wasim, my stint at RRI would not have been the same without your support. My penchant for polarisation is because of you.

Thanks to my parents and family to whom I owe all my accomplishments. Divi - you're the sister I never had. You've always been there to give me that little push, motivate me to do my best and encourage me when I've lost hope. Kevy - you've always rooted for me and only been a phone call away no matter the time zone. I will always be grateful for that. Momma, you taught me to be a strong and independent woman like you, not afraid to challenge the norm. You are truly inspirational. Papa, everything I am today is because of you. Your constant love, support and guidance has made me the person I am today. You are my best friend. Finally, Themiya for your love and for being who you are.

Abstract

Radio astronomy is currently exploring an intriguing new phase space that probes the dynamic Universe on timescales of milliseconds. Recent development of sensitive, high time resolution instruments has enabled the discovery of millisecond duration fast radio bursts (FRBs) and the erratic rotating radio transients (RRATs). A key distinguishing factor between FRBs and RRATs lies in the dispersion measure (DM) contribution along the line-of-sight through the Milky Way Galaxy's interstellar ionised plasma. The DMs of RRATs are consistent with them being a Galactic population, whereas FRBs have DMs well in excess of the expectation for a Galactic population. It is a decade since the discovery of FRBs and despite several clarifying discoveries and hypothetical explanations, no consensus has emerged regarding their origin. In this thesis I explore the possibility of using these FRBs as unique probes of the intergalactic magnetic field (IGMF) by studying their polarisation via Faraday rotation. A robust method to obtain rotation measures (RMs) through Faraday rotation of single pulses was devised and tested on RRATs. This method enabled the first RM measurements of 18 known RRATs and has been applied to several FRBs.

This thesis takes advantage of the recent upgrade to the Molonglo Observatory Synthesis Telescope (UTMOST) to conduct surveys for FRB discoveries. I performed Monte Carlo simulations of a cosmological population of FRBs to determine the detection rate at UTMOST. The UTMOST, with its large instantaneous field-of-view and high duty cycle, is being transformed into an FRB discovery machine that will be capable of detecting an FRB a week. The null detections during the initial two surveys, which were performed as part of commissioning science, enabled estimations of upper limits of FRB rates at 843 MHz. The third survey period at UTMOST resulted in the first interferometric detections of 3 FRBs, placing their origin at beyond the ~ 10000 km far-field region of the telescope, thus ruling out terrestrial radio interference as a source. Based on these detections we estimate a rate of $\gtrsim 78$ events/sky/day above a fluence of 11 Jy ms, at 843 MHz.

For my family.

Acronyms, Abbreviations and Conventions

AGN Active Galactic Nucleus

ATA Allen Telescope Array

ATNF Australia Telescope National Facility

BPSR Berkley-Parkes-Swinburne Recorder

CSIRO Commonwealth Scientific and Industrial Research Organisation

DEC Declination

DM Dispersion Measure

EOS Equation of State

FRB Fast Radio Burst

FPGA Field Programmable Gate Arrays

FWHM Full-Width Half-Maximum

GPU Graphics Processing Unit

GBT Green Bank Telescope

Hilat High latitude

HTRU High Time Resolution Universe

IAU International Astronomical Union

IGM Intergalactic Medium

ISM Interstellar Medium

LNA Low Noise Amplifier

LOFAR Low Frequency Array for Radio Astronomy

LF Luminosity Function

Medlat Intermediate latitude

MB Multi-beam

MWA Murchison Widefield Array

NS Neutron Star

PA Position Angle

PAF Phased-Array Feed

PDFB Parkes Digital Filterbank System

PFB Polyphase Filterbanks

PSR Pulsar

PSRCAT Pulsar Catalogue

RA Right Ascension

RRAT Rotating Radio Transient

RM Rotation Measure

RFI Radio Frequency Interference

RVM Rotating Vector Model

SFH Star Formation History

SFR Star Formation Rate

SUMSS Sydney University Molonglo Sky Survey

SUPERB SUrvey for Pulsars and Extragalactic Radio Bursts

SGR Soft Gamma-ray Repeater

UTC Coordinated Universal Time

VLA Very Large Array

S/N Signal-to-Noise

$M_\odot$ One Solar mass (1.99×10^{30} kg)

P Pulsar spin period (s or ms)

$\dot{P}$ Pulsar spin period derivative (s s^{-1})

$\dot{E}_{rot}$ Rotational kinetic energy (erg s^{-1})

$\dot{E}_{dipole}$ Magnetic dipole energy (erg s^{-1})

B Magnetic field (G)

n Braking index

τ Characteristic age of the pulsar (yrs)

$T_{\rm b}$ Brightness temperature (K)

$S_{\rm peak}$ Peak flux density (Jy)

ν Frequency (Hz)

W Pulse width (ms)

D Distance (kpc, Mpc or Gpc)

$\mathcal{R}$ events sky^{-1} day^{-1}

$\mathcal{F}$ Fluence (Jy ms)

z Redshift

μ Refractive index

$\nu_{\rm p}$ Plasma frequency (Hz)

e Charge of an electron ($4.80320451 \times 10^{-10}$ statcoulomb)

$n_{\rm e}$ Electron density (cm^{-3})

$m_{\rm e}$ Mass of an electron ($9.10938356 \times 10^{-28}$ g)

$\nu_{\rm g}$ Group velocity

Δt Dispersive delay (ms)

$\mathcal{D}$ Dispersion constant ($4.158808 \pm 0.000003 \times 10^3$ MHz^2 pc^1 cm^3 s)

$\tau_{\rm DM}$ Dispersive smearing (μs)

G Telescope gain (K Jy^{-1})

$T_{\rm sys}$ System temperature (K)

$D_{\rm L}$ Luminosity distance (Gpc)

E Isotropic energy (J)

β Digitisation factor

$\tau_{\rm ISM}$ Scattering due to the interstellar media (ms)

$\tau_{\rm IGM}$ Scattering due to the intergalactic media (ms)

α Slope of the integral source count distribution

δ Dispersion index

γ Spectral index

Contents

List of Figures

List of Tables

1 Introduction

1.1 Transient radio emission

The dynamic radio Universe is a stimulating and rapidly evolving area within radio astronomy. Recent successes in the transient radio Universe explorations have been important to expanding the frontiers of knowledge. The X-ray, γ-ray and optical frequency regions of the electromagnetic spectrum are possibly the most well explored with several space-based instruments scanning the sky for unfamiliar exotic events. Whilst recent advancements in radio astronomy instrumentation and signal processing have led to the benefits of high time resolution, we have been hampered by the immense overheads required for signal processing and the dearth of appropriate wide-field survey instrumentation and systems, thus resulting in a large unexplored domain of transients.

Recognized transient phenomena occur on timescales of nanoseconds a.k.a 'fast' to years a.k.a 'slow' thus spreading over a wide range of time domain phase space. For example, the signal strength of single 'nanoshot' pulses from the Crab pulsar can exceed 2 MJy and are unresolved to $<$0.4 ns timescales (Hankins & Eilek, 2007). Phenomena like afterglows of supernovae and γ-ray bursts have timescales on the order of years. Simply put, fast transients are sources that can be easily missed at the blink of an eye and necessitate high frequency and time resolutions, whereas slow transients are sources that require imaging or sampling in a raster-scan over various timescales such as a daily snapshot.

There are several sources that emit in the radio in addition to other wavelengths, the most commonly known of which are the Sun and planets in the solar system. Radio sources that show variability and a range of transient phenomena are shown in Figure 1.1 and include:

1. *Planetary and stellar emission*: The Sun, flare stars, ultracool brown dwarfs and

Jovian planets are well known sources of transient radio emission.

(a) The Sun is the brightest radio emitter in the sky and its flux varies over an 11-year solar cycle. The Solar bursts occur between 20 kHz - 2 GHz and are classified as Type I-V (Bai & Sturrock, 1989). The short narrow-band bursts last about a second, while the broadband continuum bursts can last days. Type I bursts are due to plasma radiation during high sunspot activity and last typically a second (Wild et al., 1963); Type II bursts last $\sim$ 30 minutes and are caused by shock waves propagating outwards (Wild et al., 1963); Type III bursts last several seconds and are due to sub-relativistic particles accelerating away from the Sun's surface (Bastian et al., 1998); Type IV bursts are related to the decay phase of solar flares and are observed as broadband quasi-continuum features and aren't as common as Type II and III bursts (Cane & Reames, 1988; LaBelle et al., 2003; Pick et al., 2005); Type V bursts are seen as an extended phase to Type III bursts at low frequencies and last up to a minute. These types of bursts are relatively rare. Almost all the flares and bursts are due to plasma variations and instabilities seen below 200 MHz (Melrose, 1980).

(b) The Jovian decametric radio emissions occur between $\sim$ 4 to 40 MHz with two distinct categories – short and long. The short bursts last between 1 and 10 ms and the long bursts between 0.5 and 5 s. One of the moons of Jupiter, Io has been found to amplify Jupiter's emission in the decameter regime. These Io-dependent bursts have brightness temperatures $T_{\rm b} \sim 20$ K and belong in the 'short burst' burst regime. The Jovian planets and the Earth also show auroral radio emission due to their magnetic fields (Zarka, 1998). These emissions are thought to be due to cyclotron maser instabilities in the magnetosphere and the incident solar radiation controls the radiated power (Djorgovski & King, 1984).

(c) In addition to the Jovian decametric radiation mentioned above, another example of cyclotron maser radiation is Auroral Kilometric Radiation (AKR) from the Earth's auroral regions at a radial distance of 2 to 3 times the radius of the earth (Kaiser & Alexander, 1976). They are extremely powerful terrestrial electromagnetic radiation with intensities typically around 10^7 W but occasionally up to 10^9 W (Gurnett, 1974) and extend from 50 to 500 kHz (Mutel et al., 2000). Based on *in situ* satellite observations, Ergun et al. (1998) show that the emission arises primarily in electron density depleted cavities where the ratio of electron plasma frequency (ω_p) to cyclotron

frequency (ω_c), is less than or equal to 0.2.

(d) Flare stars are nearby M type dwarf stars that occasionally produce strong incoherent radio outbursts. Coherent flares lasting a few minutes, have been observed with a high degree of circular polarisation at ~ 1 GHz (Osten, 2008; Osten & Bastian, 2008). A small number of bright brown dwarfs have also been seen to exhibit periodic flares on timescales of 2-3 hours and last for several minutes (Hallinan et al., 2008). These pulses have been observed between 3 and 5 GHz. Electron cyclotron maser instability originating at the magnetic poles has been proposed as the emission mechanism for both flare stars and brown dwarfs (Osten, 2008).

2. *Extragalactic objects*: Violent activity visible throughout the entire electromagnetic spectrum is produced by the nuclei of a variety of objects at the centres of galaxies. A characterisation of the energy source from such activity has proven to be a challenge. Blazars, quasars, Seyfert galaxies, radio galaxies and milder forms such as our Milky Way can be broadly grouped as Active Galactic Nuclei (AGN), with supermassive black holes having masses $10^5 - 10^{10}$ times the mass of the sun, at their cores (Kellermann & Moran, 2001). The surrounding accretion disk region and bipolar jets of the black hole are visible on AU and Mpc scales and as the accretion energy is converted into high energy radiation it is seen over most of the electromagnetic spectrum (Ulrich et al., 1997; Netzer, 2015). The radio galaxies, both radio-loud and radio-quiet are characterized by bipolar outflows of streams of energetic particles that reveal themselves through radio emission on a range of scales through incoherent synchrotron radiation from ultra-relativistic electrons spiralling in a weak magnetic field (Zensus, 1997). This emission has been observed to arise on scales of a parsec to a Mpc. The process by which this energy is produced still remains an intriguing problem leading to several models being proposed for the possible methods of production (Ulrich et al., 1997). The luminosity of a radio-loud AGN is attributed to the emission of jets and the radio lobes they launch. The jets are most easily detected at radio wavelengths due to synchrotron radiation. The bright knots, hot-spots and jets that are launched from these systems, produce X-ray flares (Netzer, 2015). Simultaneous radio and X-ray observations of these flares could provide valuable information about the central engine and the physics of the jets.

3. *Explosive events*: Supernovae (SNe, Weiler et al., 2002) and gamma-ray bursts

(GRBs, Kulkarni et al., 1998) produce long-lived transient radio emission, visible as lingering afterglows following the bursts observed at optical wavelengths for SNe and in X-rays and gamma-rays for GRBs. The radio afterglow is typically seen in Type Ib/c and Type II a.k.a core collapse SNe events peaking nearly simultaneously and months after the optical respectively (Weiler et al., 2002). In supernovae, the radio afterglow is thought to be due to the collision of the supernova shock wave into the ionized circumstellar medium, generating incoherent synchrotron radiation over a range of radio frequencies (Weiler et al., 1982). GRBs however are only visible for seconds at gamma-ray frequencies (Weiler et al., 2002) with only a few having detectable radio counterparts. These afterglows which are visible as jets from the GRB, traverse the interstellar medium (ISM) and produce incoherent synchrotron emission. The emission peaks first in the X-rays, optical and finally in the radio with increasing radial distance from the source (van Paradijs et al., 2000). The radio afterglows are typically visible between 0 - 80 days after the burst (Chandra & Frail, 2012).

4. *Serendipity*: In 2007, a 5-ms wide, 30-Jy highly dispersed pulse named the 'Lorimer' burst was discovered. This appeared to be an one-off event with no repeat pulses seen in ~ 80 hours of follow-up observations. Since then several similar bursts have been discovered almost exclusively at 1400 and 800 MHz and have been termed 'Fast Radio Bursts' (FRBs) (see Section 1.4 for more information).

The work undertaken for this thesis focuses on fast transients, particularly single pulses from fast radio bursts and neutron stars, which are discussed in detail in the following sections. This thesis primarily aims to contribute towards our understanding of the nature and origin of fast radio bursts.

1.2 Neutron stars and their observed manifestations

The idea of neutron stars (NSs) as a consequence of supernova explosions occurring in stars that are $10M_{\odot}$ or more was initially proposed by astronomers Walter Baade and Fritz Zwicky in 1933 (Baade & Zwicky, 1934), long before observational evidence for them became remotely possible. Following this, (Oppenheimer & Volkoff, 1939) published the theory of neutron stars, with sizes of 10 km and surface temperatures of 10 million degrees. The prospect that NSs might one day be detectable resulted from the discovery of cosmic X-rays from the compact star Scorpius X-1 in the 1960s. Following this discovery, precision modeling of probable NS observational properties began (Tsuruta, 1964). Franco

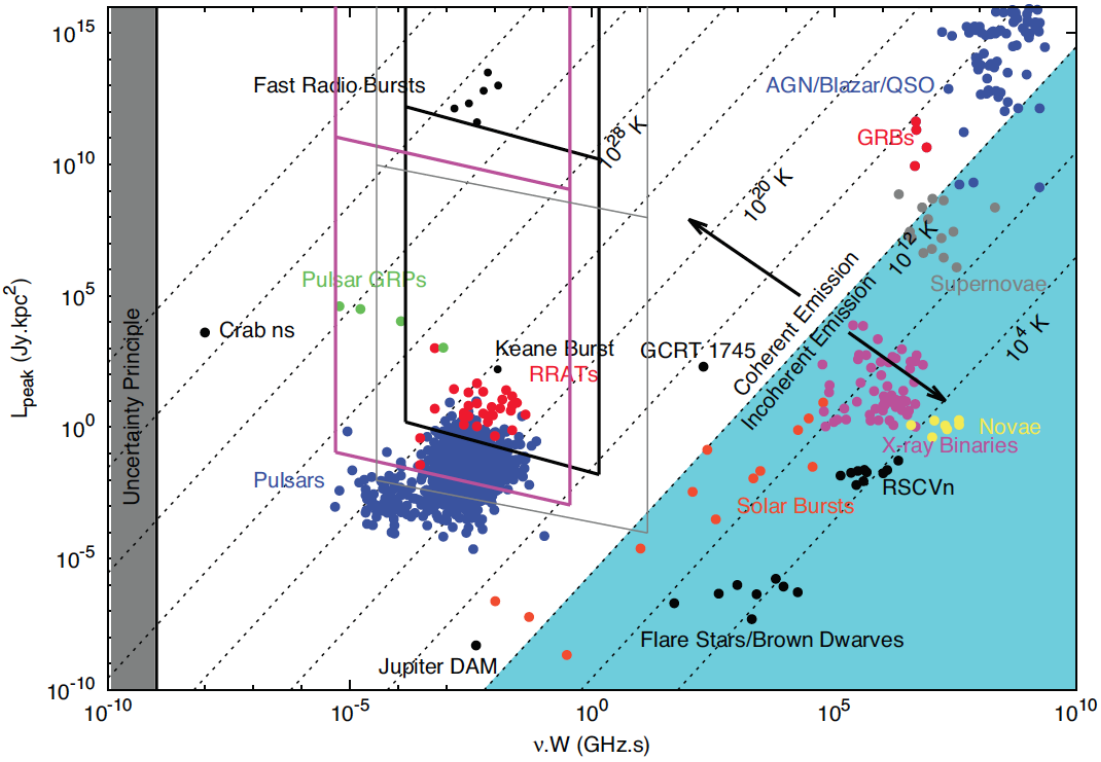

Figure 1.1 The phase space of radio transients from Macquart et al. (2015). The diagonal lines represent lines of constant brightness temperatures with 10^{12} K separating the incoherent emission processes (blue triangle) from the coherent emission processes (white region).

Pacini in the year 1967, shortly before the discovery of pulsars, postulated that strongly magnetized NSs would emit in the radio and even noted that such energy could drive a supernova remnant around a neutron star, such as the Crab Nebula (Pacini, 1967).

There are presently $\sim$ 2500 known NSs mostly catalogued in the radio (Kaspi et al., 2006), most of which show evidence of being pulsars. Although most of them are 'radio loud' and primarily studied in the radio, they are also observed at higher energies such as optical, X-rays and γ-rays.

1.2.1 Pulsars

A pulsar is a rapidly rotating dense neutron star that beams radiation along a magnetic axis which is misaligned to the rotation axis. As the star spins the beams of radiation sweep across the sky much like a lighthouse and if one of these beams intersects the line-of-sight (LOS) of the observer, it results in a characteristic pulsed electromagnetic signal, with the pulsation phase coincident with the neutron star rotation phase. The detection of the radio pulsar CP1919+21 with a 1.3 s period, led to the first observational confirmation of a NS in 1968 by Jocelyn Bell and Antony Hewish (Hewish et al., 1968). Following the discovery of the first pulsar, Thomas Gold independently proposed a neutron star model (Gold, 1968), similar to that of Pacini's and which could account for the pulsed radiation observed by Hewish et al. (1968). Though the emission mechanism and the origin of the pulses were unknown at the time of discovery, the discovery of the Crab pulsar in 1968 provided confirmation of the rotating neutron star model of pulsars. If a star had to be rotating that rapidly, it would have to be extremely dense so as not to tear apart due to centrifugal forces. The 33-millisecond pulse period of the Crab pulsar, was too short to be consistent with any other proposed models for pulsar emission.

If we know the spin period of a star, in principle, limits on central density can be estimated. Assuming a star of radius R, period P and mass M, the angular velocity, Ω can be calculated as,

$$\Omega = \frac{2\pi}{P}. \tag{1.1}$$

The equatorial centrifugal acceleration cannot exceed the gravitational acceleration for a gravitationally bound star, requiring,

$$m\Omega^2 R < \frac{GMm}{R^2} \tag{1.2}$$

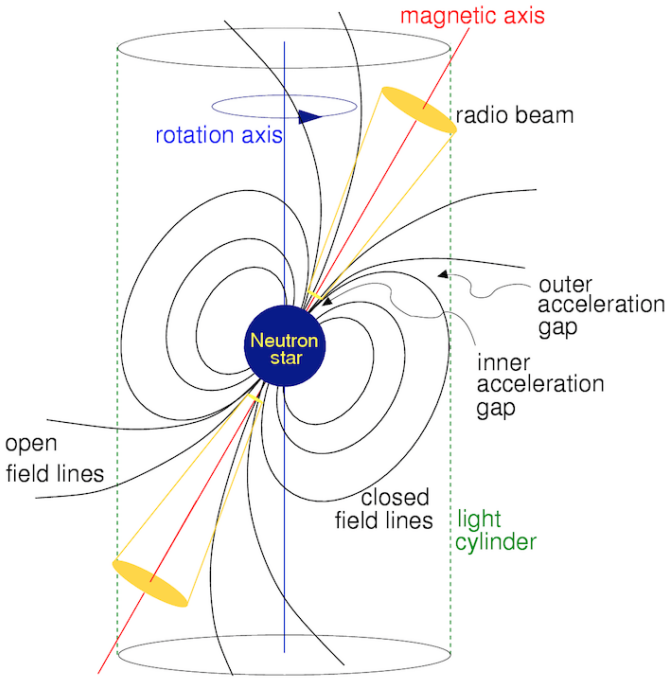

Figure 1.2 The standard lighthouse model of pulsar emission taken from Lorimer & Kramer (2012).

where, G is the gravitational constant. Hence,

$$GM > \frac{4\pi^2 R^3}{P^2} \tag{1.3}$$

$$P^2 > \frac{4\pi^2 R^3}{GM}. \tag{1.4}$$

Assuming spherical symmetry for the star, the density can be calculated as,

$$\rho = \frac{3M}{4\pi R^3}. \tag{1.5}$$

Substituting Equation 1.5 in Equation 1.4 yields,

$$P > \sqrt{\frac{3\pi}{G\rho}} \text{ or } \rho > \frac{3\pi}{GP^2} \tag{1.6}$$

For the source CP1919+21 assuming G = 6.673 $\times 10^{-11}$ m^3 kg^{-1} s^{-2} and P = 1.3 s, the density was found to be, $\rho \approx 10^{11}$ kg m^{-3}, which is the limit on the possible density of a white dwarf, as the electron degeneracy pressure in the star's core is insufficient to balance its own gravitational self-attraction, above this limit.

The life of a pulsar

Massive red supergiants that are 8−10 $M_\odot$ undergoing Type II supernova explosions are thought to be NS progenitors (Blaauw, 1985; Teukolsky & Shapiro, 1983). As the star ages, the hydrogen that fuels the core by the fusion of hydrogen to helium is depleted. This forces the helium to undergo a helium capture reaction followed by oxygen fusion to in turn fuel the core which ultimately leads to the formation of heavy elements like nickel and iron in onion-like layers (Teukolsky & Shapiro, 1983). The high binding energy per nucleon of iron prevents further fusion of elements causing the iron core to contract until it reaches the Chandrasekhar limit. This limit is the maximum stable mass of a white dwarf ($1.4M_\odot$) and is derived from the equation-of-state (EOS) dictated by the temperature, pressure and density of matter. In keeping with Pauli's exclusion principle, the electrons are the first particles to become degenerate in a NS due to their lower mass, and this is attained when the density of matter is so high that these particles cannot be packed any closer together in terms of their energy states. The electron degeneracy pressure fails to support the gravitational pressure of the star beyond the Chandrasekhar limit (Teukolsky & Shapiro, 1983). At this point the dense core, unable to support itself, collapses on itself and the matter inside undergoes a process called inverse beta decay, which causes protons and electrons to merge and form neutrons and neutrinos into a compact dense structure.

The neutrinos apply immense outward pressure at such densities, though they do not normally interact with matter. The neutron degeneracy caused by the neutrons being tightly packed in the core causes the halt of the core collapse and the outer layers that collapse inwards, bounce back, thus exciting shock waves of dust and gas into the ISM in the process. The result is a supernova explosion, whose brightness can briefly outshine our own Galaxy. At the heart of this explosion lives an extremely dense and rapidly rotating, hot stellar corpse retaining only a small faction of its progenitor's size and mass. During collapse, the neutron star conserves angular momentum thereby typically yielding rotational periods in the millisecond range at birth and conserves magnetic flux thereby yielding surface fields of $\sim 10^{12}$ G at birth. These estimates of periods and magnetic fields are simple and ignore the likely complexity of torques acting on the proto NS during collapse and the possibility of a magnetic dynamo mechanism. It is born with a radius ~ 10 km, surface temperature $\sim 10^9$ K and mass $\sim 1.5\,M_\odot$. The maximum theoretical mass for NSs due to causality is the Tolman-Oppenheimer-Volkoff limit ($1.5 - 3.0\ M_\odot$), analogous to the Chandrasekhar limit for white dwarfs (Teukolsky & Shapiro, 1983). There is no stable EOS for a stellar remnant whose mass exceeds that of the Tolman-Oppenheimer-Volkoff limit, resulting in the collapse to a black hole (Oppenheimer & Volkoff, 1939). A

more detailed review of NS EOS models can be found in Lattimer & Prakash (2004).

Broadly speaking, based on observations pulsars are divided into two classes[1] – the normal pulsars and the millisecond pulsars. The majority of the pulsar population are normal pulsars with $P \sim 500$ ms and $\dot{P} \sim 10^{-15}$ s s^{-1}. Millisecond pulsars have periods two orders of magnitude smaller $P \sim 5$ ms and $\dot{P} \sim 10^{-20}$ s s^{-1}. The emission mechanism of pulsars is quite poorly understood and is still an open question (Melrose, 1992). It is accepted that the charged particles move at relativistic velocities, spiraling along the magnetic field lines leading to synchrotron and curvature radiation in the X-ray and radio (S. Longair, 1992). Pulsar emission requires coherency in the emission process and the origin of the coherency remain unknown. Pulsars are observed over frequencies ranging from 10s of MHz to $>$ 100 GHz in the radio, with spectral indices (a measure of the dependence of flux density on frequency) typically between 0 and -3 indicating that they are typically brighter at lower frequencies. Also, pulsars being offsprings of main sequence stars, on average populate the Galactic plane. However, there is evidence of pulsars traveling out of the plane at velocities higher than their progenitor star, possibly due to large natal kicks, eg: PSR B2224+65 with a transverse speed of $\gtrsim 800$ km s^{-1} in the Guitar Nebula (Cordes et al., 1993). Pulsars have proven to be excellent probes of (1) the ISM (Lyne & Smith, 1989; Han et al., 2006) (2) gravity (Taylor et al., 1979) and (3) extreme physics (Lattimer & Prakash, 2007). Over the last decade several successful maps have been made of the Galactic magnetic field exploiting the RMs and DMs of pulsars through Faraday Rotation measurements (see Chapter 3 for details). Precision pulsar timing of the dynamics of binary systems has enabled precise measurements of their orbital parameters and companion masses. With regard to gravity, the loss of energy in the decaying orbit of the NS-NS system observed through PSR B1913+16 agrees with the expected emission of gravitational waves predicted by general relativity to within 0.3% which is the first indirect detection of gravitational radiation (Weisberg et al., 2010). Also the determination of the masses of the NSs in the double pulsar system J0737−3039A&B through pulsar timing, has permitted the most rigorous test of general relativity in the strong-field regime (to 99.5% precision ; Kramer et al., 2006b) through a comparison of observed properties of the relativistic orbit with the predicted parameters of general relativity.

Pulsar fundamental parameters

The time of arrival of a pulse from a pulsar is predictable because the NS spin is remarkably stable due to its high angular momentum and beamed radiation. However, a pulsar's

[1]It should be noted that this is an oversimplification.

rotation period is seen to increase over time as predicted by the neutron star model by Pacini (1967) due to the loss of rotational kinetic energy carried away by the emitted radiation. Pulsars are typically rotation powered and are characterised by their spin period P and period derivative $\dot{P}$. The loss in energy given by Lorimer & Kramer (2012) is,

$$\dot{E}_{\rm rot} = \frac{d}{dt}\frac{1}{2}I\Omega^2 = \frac{4\pi^2 I\dot{P}}{P^3} \tag{1.7}$$

where, P is the measured period and I is the moment of inertia for a uniform sphere ($I = 0.4MR^2$). Hence this is a very idealised model. Only a small portion of this energy (typically one millionth or so of the total loss in rotational energy) is produced as observable radio emission. For the most part, the energy is converted into high energy emission, magnetic dipole radiation and pulsar wind. A rotating magnetic dipole with misaligned spin and magnetic axes, according to Jackson (1962), loses energy as,

$$\dot{E}_{\rm dipole} = \frac{2}{3c^3}\left|m\right|^2\Omega^4 \sin^2\alpha \tag{1.8}$$

where, $m = BR^3$ is the magnetic dipole moment for a uniformly magnetised sphere with radius R and surface magnetic field strength B, and α is the angular offset between the magnetic axis and the spin axis. Since the neutron star is a spinning magnetic dipole, it acts as a unipolar inductor (Goldreich & Julian, 1969) which implies there is a torque even for an aligned rotator. This is shown in simulations by Li et al. (2012)

If we assume that the majority of the loss of rotational kinetic energy is due to the dipole radiation, we can equate the two to arrive at a minimum magnetic field at the pulsar surface

$$\left(\frac{B}{\rm Gauss}\right) > 3.2\times10^{19}\left(\frac{P\dot{P}}{\rm s}\right)^{1/2}, \tag{1.9}$$

and a simple power law explaining the 'efficiency of spin-down braking'. For a spin frequency $\nu = 1/P$, Lorimer & Kramer (2012) show that,

$$\dot{\nu} = -K\nu^n \tag{1.10}$$

where n is the braking index. The value of n typically ranges between 0.9 - 2.9 (Kaspi & Helfand, 2002) but is often contaminated by timing noise. We can derive the age of the pulsar by integrating the above equation with respect to the spin period and assuming (1) $P_0 \ll P_{\rm present}$ (i.e. the pulsar was born with a spin period that is much lower than what

it is now) and (2) n = 3.0 (i.e. assuming a purely magnetic dipole), to give

$$\tau = \frac{P}{2\dot{P}} \tag{1.11}$$

where τ is the "characteristic" age or "spin-down" age. The characteristic age is an approximation because the birth period of a pulsar is usually unknown. The above equation only holds well for the assumptions made as in particular, n=3 is not always the case in reality. The "spindown" or characteristic age depends only on P and $\dot{P}$ and is independent of the unknown radius, moment of inertia or the perpendicular magnetic field. A plot of the parameters P versus $\dot{P}$ shown in Figure 1.3 is used as a standard to track the birth-death cycle of pulsars and is analogous to the Hertzsprung-Russell diagram for ordinary stars. The age and magnetic field strength of pulsars are shown as lines on this plot. Newborn pulsars that are associated with their parent supernova remnants manifest themselves towards the centre of the diagram. With age, they gently transition to the bottom right until they cross the death line over into the graveyard where they cease emitting radio pulses. Observationally only young pulsars ($\lesssim 10^5$ years) are associated with their parent supernova remnants whilst older pulsars ($\gtrsim 10^6$ years) are not (Teukolsky & Shapiro, 1983). This is either due to natal kicks which discharge the pulsar with a speed sufficiently high to move away from the parent supernova remnant or because the remnants have merged into the ISM. Pulsars below the spin up line near $\log[\frac{\dot{P}}{P}\ \mathrm{s}^{-1}] \sim -16$ are in binary systems as verified by the monitoring of their orbital variations over time. These are the millisecond or 'recycled' pulsars that have been spun up by accretion of mass and angular momentum from their companion stars. Approximately 80% of millisecond pulsars still reside within binary systems as shown by Grégoire & Knödlseder (2013).

1.3 Rotating Radio Transients

Rotating radio transient (RRATs) were first discovered in 2006, in archival data from the Parkes Multibeam Pulsar Survey (McLaughlin et al., 2006). They were discovered at 20-cm as single pulses rather than in Fourier domain searches, with widths between $2-30$ ms and peak flux densities between $0.1-3.6$ Jy. Since no consecutive pulses were identified in the periodicity searches, it suggested that the RRATs were either weakly emitting during those periods or were in fact "off". If the infrequently-detectable emission is due to them being "off" or nulling, then their population is possibly greater than or equal to that of the normal radio pulsars (Keane & Kramer, 2008). The difficulty in detecting them

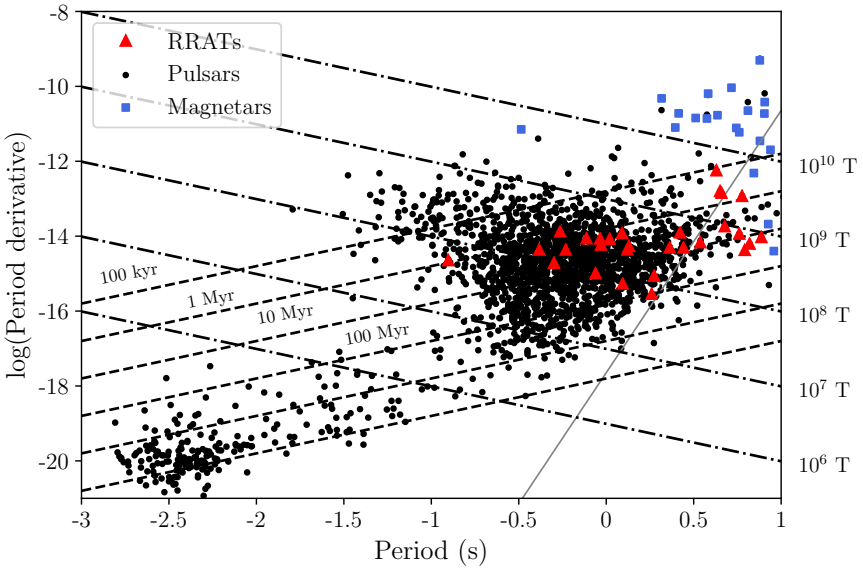

Figure 1.3 The $P\dot{P}$ diagram tracing the lives of pulsars. Lines of constant surface magnetic field strength and characteristic age are shown as dashdot and dotted lines. The graveyard zone lies below the solid 'death line'. Circles denote pulsars, squares represent magnetars and the triangles mark the positions of RRATs.

due to their variability, implies a largely undetected source population (Keane & Kramer, 2008) which does not comply with the estimated core-collapse supernovae rate in the Milky Way, causing a discrepancy. This over-estimation of the RRAT population could be due to extrapolations from a small number of known sources and can be reconciled if RRATs somehow form a particular stage in pulsar evolution (Keane & McLaughlin, 2011). Properties such as the Galactic distribution (Burke-Spolaor & Bailes, 2010) and pulse energy distributions of RRATs (log-normal) (Keane et al., 2010; Miller et al., 2011) have been studied and they appear to be similar to those of normal radio pulsars.

RRATs is the name given to a group of sporadically pulsing radio sources with the majority of them having been seen to repeatedly emit detectable pulses (Keane, 2016). More recently, RRATs were defined as repeating radio sources with an underlying periodicity, that do not emit persistently in the radio (Keane & McLaughlin, 2011). They exhibit extreme pulse amplitude distributions, like the Crab pulsar's "giant pulse" phenomenon for instance. The interval between the single pulses can last anywhere between minutes (4 pulses per minute) to hours (3 pulses per hour) (Keane & McLaughlin, 2011). Their underlying periodicities P are somewhat typical of slow pulsars, lying between $0.17 - 7$ seconds.

Radio pulses of short timescales with a pulse width W and peak flux density S originating at a distance D and observed with a frequency ν have a brightness temperature,

$$T_{\rm b} \simeq 10^{30}\,{\rm K}\left(\frac{S_{\rm peak}}{\rm Jy}\right)\left(\frac{\nu}{\rm GHz}\right)^{-2}\left(\frac{W}{\mu{\rm s}}\right)^{-2}\left(\frac{D}{\rm kpc}\right)^{2}. \tag{1.12}$$

The high brightness temperatures of RRATs $10^{22} - 10^{23}$ K indicate coherent non-thermal emission with a causally connected emission region. The light travel time across the emitting region and the observed pulse width present an upper limit on its size. Assuming a millisecond timescale width of a typical pulse the emission region of RRATs are $\lesssim 300$ km. The observed RRATs only represent a small fraction of the observed pulsar population and are poorly understood due to the relatively small number of observed sources[2] (~ 110).

1.3.1 What are RRATs?

Although the nature of RRATs is still poorly understood, several hypotheses and models have been proposed to explain the observed behaviour. One proposition was that RRATs are distant faint pulsars with high variability in their amplitude from pulse-to-pulse, such that only the few brightest pulses from them are detectable. Burke-Spolaor & Bailes (2010) however show that this can only apply for a small subset of RRATs as in their study of archival Parkes survey data, they identified two sources that emitted pulses that were too frequent and bright to be originating from a log-normal pulse energy distribution. Another suggestion is that they are extreme nullers with a rotation period much longer than the "on" window region of the pulse and high nulling fractions ($> 99\%$). The nulling fraction is the average fraction of rotations spent in an "off" mode causing the degree of intermittency to vary. Several observations suggest that nulling results from persistent and large-scale variations in the magnetospheric current distribution (van Leeuwen et al., 2002; Redman et al., 2005; Esamdin et al., 2005). Observations of PSR B1931+24 (Kramer et al., 2006a) indicate that the nulls may likely be due to a halting or redistribution of the current which leads to a beam pattern with no or little power in the direction of the observer.

The discovery of the RRAT J0941−39 reported in Burke-Spolaor et al. (2011) may represent a link between RRATs and pulsars, as it was discovered as an RRAT but later appeared to be a pulsar with a low nulling fraction. More importantly, the RRAT emission was seen to be coincident with the pulsar emission implying a link between the two,

[2]http://astro.phys.wvu.edu/rratalog/

speculatively implying that the nulling pulsars might undergo increases in their nulling fraction with age. Wang et al. (2007) show that there is no correlation between the characteristic age of a pulsar and its nulling fraction. However according to their Figure 8 the nulling pulsars appear to increase with proximity to the radio death line.

As evident from their position in the $P - \dot{P}$ diagram (see Figure 1.3), some RRATs exhibit long spin periods and high magnetic fields. Their positions in the $P - \dot{P}$ are among those of the normal pulsar population though slightly closer to that of the magnetars. Magnetars are a class of pulsars whose total energy budget is dominated by the magnetic energy reservoir as opposed to released rotational energy. They typically have magnetic fields of order $10^{14} - 10^{15}$ G compared to the 10^{12} G of pulsars. Presently 29 magnetars[3] are known, most of which are detected in the X-ray and γ-ray regimes with fewer in the radio. The magnetar-RRAT connection was strengthened with the detection of radio emission from the X-ray magnetar XTE J1810−197 (Camilo et al., 2006) and X-ray emission from a high-B radio RRAT, J1819−1458 (Reynolds et al., 2006). The latter has displayed unusual glitch activity (Lyne et al., 2009) and also shows a bright pulsar wind nebula (Rea et al., 2009). However no conclusion has been reached regarding the evolutionary link between pulsars and RRATs and more multi-wavelength data are required to further analyse this theory.

1.3.2 Polarisation of RRATs

The RRAT J1819−1458 was the first of its kind to have its Rotation Measure (RM) estimated, from polarisation observations (Karastergiou et al., 2009). The RM quantifies the amount of rotation undergone by the angle of linearly polarised radiation, as the radio wave traverses the magnetised ISM. This was done using an integrated pulse (Karastergiou et al., 2009). A venture to determine the RMs of individual single pulses via Faraday rotation is discussed in Chapter 3. A pilot study was conducted on giant single pulses from Vela to estimate the magnetic field along the LOS towards a single pulse (as opposed to an integrated pulse profile). Most pulsars are only up to 75% linearly polarised. Vela, being an exception to the rule, is 100% linearly polarised. We determined an RM of 32.0 ± 0.1 rad m^{-2} from the weighted mean of the single pulse RM distribution, which agrees well with the published value of 31.4 ± 0.1 rad m^{-2} in the ATNF Pulsar Catalogue[4]. This variation in RM is not uncommon as it depends on the DM along the LOS (see equation 1.33) and has been reported in Hamilton et al. (1977), where they observed

[3] `http://www.physics.mcgill.ca/~pulsar/magnetar/main.html`
[4] `http://www.atnf.csiro.au/people/pulsar/psrcat/`

Vela's RM to change by 14% between 1970 and 1976. All the RMs in Hamilton et al. (1977) have been corrected for the effects of Faraday Rotation in the Earth's ionosphere. The corrections were in the range $0.7-1.3$ rad m^{-2} for these observations and are estimated to be uncertain by less that 10%. The pilot study in this thesis has led to the first RM measurements of 18 known RRATs (see Chapter 3) and the method has been successfully applied of a class of transients called Fast Radio Bursts, discussed in the following section.

1.4 Fast Radio Bursts

The discovery of the RRATs in 2006 motivated astronomers to comb through archival pulsar surveys in hopes of finding more such RRAT single pulses. This motivation led to the discovery of the (prototypical) 'Lorimer Burst' in archival data from 2001 (Lorimer et al., 2007). The burst followed the classic dispersion sweep (refer to Figure 1.4 and Section 1.5.1) and showed scatter-broadening with a power-law dependence that is characteristic of a celestial origin. This pulse was extremely bright with a peak flux density of ~ 30 Jy and lasted only ~ 5 ms. The DM of the burst is 375 pc cm^{-3} at the observed Galactic latitude of $b = -41.8°$ which is 20 times greater than the expected contribution from the Galaxy along this LOS according to the NE2001 model by Cordes & Lazio (2002). Given its large DM, Lorimer et al. (2007) proposed that this burst originated at extragalactic/cosmological distances, with its DM dominated by propagation through the Intergalactic Medium (IGM), and contributions from the ISM in the Milky Way and the ISM in a putative host galaxy.

The discovery of "odd" dispersed pulses dubbed 'Perytons' at the Parkes radio telescope in 2011 caused some worry about the authenticity of the Lorimer burst (Burke-Spolaor et al., 2011). These Perytons looked remarkably similar to the Lorimer burst, but also have striking differences, more in common with radio frequency interference (RFI). The confusion was finally put to rest when they were identified to be caused by improperly shielded microwave ovens onsite at the Parkes radio telescope (Petroff et al., 2015c). For years however, the Lorimer burst was in a class of its own. It was not until much later, when four more bursts were discovered at the Parkes radio telescope providing strong evidence for the astrophysical nature, did the class 'Fast Radio Bursts' or FRBs emerge (Thornton et al., 2013). Like the γ-ray bursts the FRBs are also named based on the date of detection (e.g. FRB160410 was detected on 2016 April 10). Thornton et al. (2013) arrived at a rate estimate after having processed $\sim 24\%$ of the high latitude sub-survey of the High Time Resolution Universe survey. The rate was calculated to be,

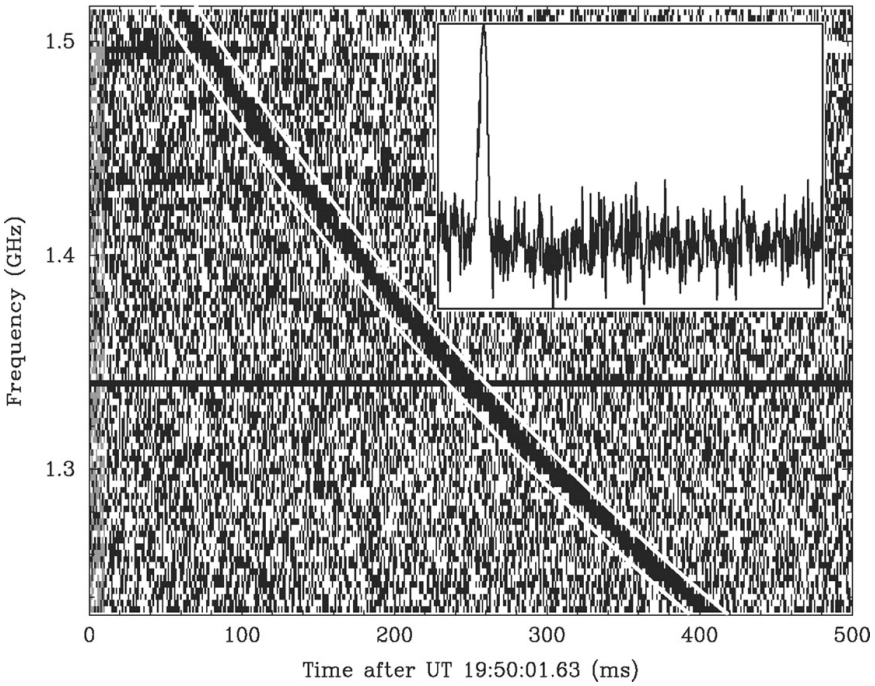

Figure 1.4 Waterfall plot showing frequency versus time of a sidelobe detection of FRB 010724 or the "Lorimer Burst". The pulse was detected with a flux density of ~ 30 Jy and a DM of 375 pc cm^{-3} during an observation of the Small Magellanic Cloud. The two white lines separated by 15 ms on either side of the the pulse show the expected behaviour for the cold-plasma dispersion law assuming the observed DM. Only $\sim 7\%$ of this DM was accounted for in this direction by the Milky Way, suggesting an extragalactic origin. The horizontal line across the plot is an artefact in the data caused by a malfunctioning frequency channel. The inset shows the total-power pulse profile after correcting for the dispersive delay, assuming a DM of 375 pc cm^{-3} at a reference frequency of 1.5165 GHz. Figure taken from Lorimer et al. (2007).

$$\mathcal{R}_{\rm FRB}(\mathcal{F} \sim 3\,{\rm Jy\,ms}) \geq 1.0^{+0.6}_{-0.5} \times 10^4\,{\rm events\,sky^{-1}\,day^{-1}}. \tag{1.13}$$

Champion et al. (2016) present an updated all-sky FRB rate of,

$$\mathcal{R}_{\rm FRB}(\mathcal{F} \geq 0.13\,{\rm Jy\,ms}) \geq 7^{+5}_{-3} \times 10^4\,{\rm events\,sky^{-1}\,day^{-1}} \tag{1.14}$$

after having processed 100% of the high latitude sub-survey at the 95% confidence interval.

An FRB is defined as a burst of coherent radio emission of millisecond duration, exhibiting a dispersion sweep characteristic of propagation through a cold ionised plasma with DMs well in excess of the Galactic contribution along the observed LOS. However, there are typically uncertainties of order $\sim 50\%$ on the DM estimated by the NE2001

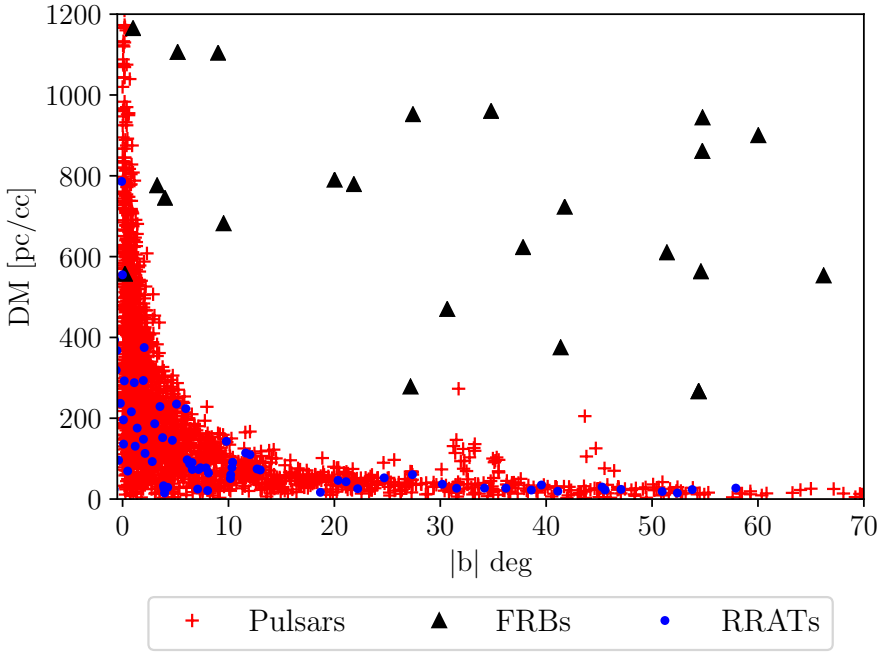

Figure 1.5 The Galactic latitude versus DMs of the known pulsars (red crosses), RRATs (filled blue circles) and the published FRBs (black triangles). The FRBs show significantly higher DMs than pulsars and RRATs for similar separations from the Galactic plane.

model given that it only accounts for the thin disk, thick disk and Galactic centre and is poorly constrained in the Galactic halo. Given that the vast majority of the 24 known FRB detections have been far from the plane, accounting for the error still cannot deem the observed DM to be purely Galactic (see Figure 1.5). The observed FRBs also have brightness temperatures well in excess of thermal emission ($T_b > 10^{35}$ K), strongly requiring coherent emission (Katz, 2014; Luan & Goldreich, 2014). If they are indeed found to be cosmological in origin, it would open up an entirely new way to probe the extragalactic and even distant Universe. They could potentially be used to,

1. solve one of the Universe's most puzzling mysteries — the case of the "Missing Baryons", the unaccounted for atoms and ions that make up the cosmos (McQuinn, 2014).

2. obtain the rotation measure of the IGM along the LOS (Zheng et al., 2014).

3. acquire an independent measure of the dark energy equation of state (Zhou et al., 2014).

A major caveat to items 1) and 3) is that while they are exciting potential applications,

the uncertainty in the DM from the host galaxy itself limits how precisely they can be used as probes of the IGM.

What are these FRBs? This question is the main driver for this thesis. It is a decade since their discovery and despite several progenitor theories we still have not conclusively identified a source of origin. Presently, there are more progenitor theories than actual FRBs detections with none of the theories having been conclusively verified. Almost all the discovered FRBs have been detected with single dish antennas with relatively poor angular resolution ($\approx 15'$). Precise localisation would require an interferometric detection as discussed in Chapters 5 and 6. Chapter 6 presents the first interferometric detections of FRBs. Some of the leading progenitor theories are summarized below. The absence of repeat pulses in re-obervations of the sky positions for most FRBs (with the exception of FRB 121102 discussed in Spitler et al., 2016) indicate that they are either cataclysmic events or originate in repetitive sources with very low rates. A third possibility is that they have high rates (i.e. small spin periods) but emit radio waves sporadically. Chatterjee et al. (2017) report on sub-arcsecond localisation of the only FRB known to repeat (FRB 121102) using radio interferometric observations. The source has been localised to a twenty-fifth magnitude low-metallicity, star-forming dwarf galaxy at $z = 0.19273(8)$ (Tendulkar et al., 2017). The precise localisation shows that the source is either co-located with a 180 μJy active galactic nucleus or an unknown type of extragalactic source. However, the exact nature of the FRB progenitor is still unknown.

A key distinguishing factor between RRATs and FRBs is the DM. The observed DMs of RRATs can fully be accounted for by the Galactic electron density contribution while the observed DMs of FRBs are well in excess of the Galactic contribution (see Figure 1.5). The total DM of an FRB is thought to be comprised of,

$$\mathrm{DM_{FRB}} = \mathrm{DM_{MW}} + \mathrm{DM_{IGM}} + \mathrm{DM_{host}} + \mathrm{DM_{source}} \tag{1.15}$$

where $\mathrm{DM_{MW}}$ is the contribution from the ISM of the Milky Way, $\mathrm{DM_{IGM}}$ is the contribution from a diffuse IGM or inhomogeneities along the line-of-sight (LOS), $\mathrm{DM_{host}}$ is any contribution from a host Galaxy and $\mathrm{DM_{source}}$ is any contribution from the source itself. The Galactic contribution can be easily estimated using the NE2001 model by Cordes & Lazio (2002) (with at most 50% or more error but typically much smaller errors) for any given LOS through the Milky Way. The excess DM after accounting for the Galactic contribution can be considered extragalactic or cosmological or intrinsic to the host. The host galaxy contribution depends upon the angle of inclination through the galaxy and is discussed in detail in Chapter 4 for spirals,

ellipticals and dwarf galaxies. The contribution from a possible host galaxy is indiscernible from the IGM contribution and we presently assume a value of 100 pc cm^{-3} for a host galaxy for a median inclination angle of $< 70°$. A simple relation between DM and z from Ioka (2003) and Inoue (2004) is used throughout this thesis,

$$z \leq \frac{\mathrm{DM_{FRB}} - \mathrm{DM_{MW}}}{1200\,\mathrm{pc\,cm^{-3}}}. \tag{1.16}$$

This value of z is an upper limit as the contribution from the host galaxy could be a significant fraction of the total DM of the FRB given the environment of the source and its location within a galaxy. For instance the magnetar at the centre of our Galaxy has a total DM of $1778 \pm 3\,\mathrm{pc\,cm^{-3}}$ which is the highest measured value for any pulsar to date (Eatough et al., 2013). As discussed above, cosmological applications are possible only through precise localisations of these bursts. For all the published FRBs, the inferred redshift estimates are in the range $0.2 < z < 1.5$, firmly placing the sources at cosmological distances. As the IGM is thought to contain 90% of the Universe's baryons, (e.g Fukugita & Peebles, 2004; Savage et al., 2014), measuring the DMs of FRBs at high redshifts is potentially a novel way to probe this important cosmological component. Furthermore, if placed at such distances, the unbeamed (isotropic) energies of the observed FRBs lie in the range 10^{31} to 10^{33} J (Keane & Petroff, 2015) which help place constraints on possible progenitor models. It should be noted that the values of these energies are calculated assuming the upper limit on redshift from equation 1.16 and could be smaller depending on change in redshift due to changes in various DM contributions. Some FRBs exhibit polarisation which implies a rotation of the plane of polarisation across the pulse, consistent with relativistic beaming from particles moving along curved magnetic field lines. More information regarding observed and inferred parameters can be found in Chapter 4 where we perform Monte Carlo simulations of a cosmological population of FRBs to study their redshift, energy, fluence, width, DM and signal-to-noise (S/N) distributions in a ΛCDM Universe (Wright, 2006).

1.4.1 Progenitor theories

Since the discovery of FRBs there have been several progenitor theories for Galactic, extragalactic and cosmological models. A satisfactory theory would have to satisfy the conditions of all-sky rate, large DMs and high brightness temperatures. A few key theories that elegantly account for two or more of these criteria are summarised below.

1. *Hyperflares from soft gamma-ray repeaters*

Soft gamma-ray repeaters (SGRs) belong to a class of NSs called magnetars with extremely high magnetic fields ($\sim 10^{15}$ G) and are distinguished by the fact that they are powered by their magnetic energy rather than the conventional rotational energy. Popov & Postnov (2010) and Lyubarsky (2014) in their models, propose intense radio bursts from magnetars in dense star-forming regions, as a possible cause of FRBs. A starquake is theorised to cause a sudden rearrangement of the crust thereby leading to the disconnection and reconnection of magnetic field lines releasing an energetic pulse (Poynting vector) in the magnetosphere. As this pulse propagates through the magnetar's relativistic wind, it creates a relativistic forward shock upon interaction with the plasma. The millisecond duration radiation producing an FRB-like event would be due to coherent synchrotron maser emission from either the forward or reverse shock front (Lyubarsky, 2014). This model neatly accounts for the high rates and brightness temperatures of FRBs (Kulkarni et al., 2014).

2. *Giant pulses from pulsars and magnetars*

Cordes & Wasserman (2016) have proposed that FRBs are rare highly energetic giant pulses from extragalactic pulsars, similar to the ones emitted by the Crab. This is backed up by the fact that the energy of the brightest individual shot pulse ever detected from the Crab (Hankins & Eilek, 2007) is comparable to that required of FRBs. However, even the brightest pulse from the Crab over its lifetime would only be observable by present systems above the detection thresholds out to a distance of ~ 300 Mpc. Similar unusually bright pulses from pulsars within this distance could also be the source of FRBs. However, FRBs have DMs indicative of a much more distant origin ($1 - 3$ Gpc; assuming that most of the DM contribution is from the IGM). This can be circumvented by assuming a cosmological model in which pulses from pulsars out to $z \leq 1$ are magnified through gravitational microlensing or scintillation, given that the giant pulses emitted from the Crab are not typical of the pulsar population as a whole. In this case, since the NS population extending to $z \sim 1$ is large enough, of order one burst per NS would satisfy the apparent FRB rate. Cordes & Wasserman (2016) however favour a nearby and hence extragalactic population without the restrictions of microlensing and radiation processes but require many more bursts per NS. The multiplicity can be small enough that no individual source would repeat over human time-scales.

An extragalactic but non-cosmological model for FRBs has been put forth by Pen &

Connor (2015) in which FRBs are thought to arise from "nuclear magnetars" located at the centres of galaxies. A consequence of this model however is the reduction in the inferred distances to FRBs, as a sizeable contribution to the total DM would be from the immediate vicinity of the source. A weakness of the model is that there is no clear case for nuclear magnetars as opposed to magnetars in other locations of the galaxies.

Connor et al. (2016b) have proposed an FRB model in which young extragalactic pulsars which are still associated with their parent supernova remnants produce bright radio pulses. Similar to the nuclear magnetar model, this also greatly reduces the inferred distances to FRBs with the typical distance being 200 Mpc. By extrapolating Crab-like giant pulses back to the first 100 years of the pulsar in a dense supernova remnant, the DM and the scatter tail due to multi-path propagation can be explained.

3. *Collapse of supramassive neutron stars (Blitzars)*
   Falcke & Rezzolla (2014) have put forward a model in which the collapse of a magnetised and isolated supramassive rotating NS into a blackhole in a rarefied environment, produces an FRB. In this model, the NS is initially created above the theoretical critical mass limit and is supported by rapid rotation. Several thousand to million years after its birth, due to magnetic braking constantly reducing its spin, the NS is unable to restrain gravitational collapse and forms a black hole. This collapse into a black hole produces a strong electromagnetic pulse due to the strong snapping of the magnetic field in the magnetosphere of the NS creating a bright radio flash. The timescale of this flash is of the order of the free-fall timescale of the collapsing material which is $\lesssim 1$ ms. They point out that only $\sim 3\%$ of the core-collapse supernova population out to $z \leq 1$ would need to produce blitzars in order to match the observed apparent FRB rate.

1.5 Propagation effects in the interstellar and intergalactic media

As the signal from a pulsar, RRAT or FRB traverses the interstellar or/and intergalactic media, they encounter four possible propagation effects namely, 1) dispersion, 2) scattering, 3) scintillation and 4) Faraday rotation. Details of these effects are discussed below.

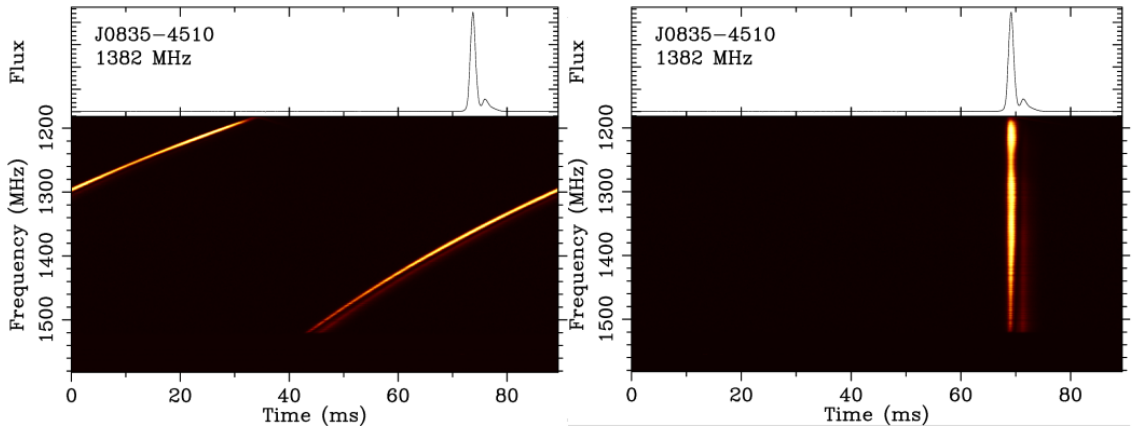

Figure 1.6 Left: Uncorrected dispersive delays for the Vela pulsar J0835−4510 over a bandwidth of 400 MHz (1024 channels of $\sim$ 390 kHz each), centred at 1382 MHz. The delays wrap since the data are folded (i.e. averaged) modulo the pulse period. Right: Pulse profile after correcting for the dispersion by applying the appropriate time delays.

1.5.1 Pulse dispersion

The pulse dispersion measure is an observational quantity which manifests itself as a broadening of an otherwise sharp pulse, when a pulsar is observed over a finite bandwidth. The electrons in the cold plasma in the ISM have a refractive index given by,

$$\mu = \left[1 - \left(\frac{\nu_{\rm p}}{\nu}\right)^2\right]^{1/2} \tag{1.17}$$

where ν is the frequency of the waves and ν_p is the plasma frequency,

$$\nu_{\rm p} = \left(\frac{e^2 n_{\rm e}}{\pi m_{\rm e}}\right)^{1/2} \simeq 8.5\,{\rm kHz}\left(\frac{n_{\rm e}}{\rm cm^{-3}}\right)^{1/2} \tag{1.18}$$

where $n_{\rm e}$ is the electron density and for the ISM, is typically $n_{\rm e} = 0.03$ cm^{-3}. From Equation 1.17 we see that $\mu < 1$ and for a radio wave to propagate, the condition $\nu_{\rm p} < \nu$ should be satisfied which follows that the group velocity ($\nu_{\rm g} = \mu c$ for a cold, unmagnetised plasma) of the waves is less than that of the speed of light given by,

$$\nu_{\rm g} \approx \left(1 - \frac{\nu_{\rm p}^2}{2\nu^2}\right). \tag{1.19}$$

As the radio wave propagates from source to observer, it interacts with the free electrons in the ISM. As the pulse traverses this diffuse plasma, the lower frequencies

travel more slowly and arrive at the telescope slightly later than the higher frequencies such that the time delay is given by,

$$\begin{aligned}\Delta t &= \left(\int_0^d \nu_{\rm g}^{-1} dl\right) - \frac{d}{c} = \frac{1}{c}\int_0^d \left(1 + \frac{\nu_{\rm p}^2}{2\nu^2}\right) dl - \frac{d}{c} \\ &= \frac{e^2}{2\pi m_{\rm e} c} \frac{\int_0^d n_{\rm e} dl}{\nu^2}\end{aligned} \tag{1.20}$$

$$\left(\frac{\Delta t}{\rm sec}\right) \approx \mathcal{D} \times \left(\frac{\rm DM}{\rm pc\,cm^{-3}}\right) \left[\left(\frac{\nu_{\rm low}}{\rm GHz}\right)^{-2} - \left(\frac{\nu_{\rm high}}{\rm GHz}\right)^{-2}\right] \tag{1.21}$$

where the dispersion constant $\mathcal{D} = \frac{e^2}{2\pi m_{\rm e} c} = 4.158808 \pm 0.000003 \times 10^3$ MHz^2 pc^{-1} cm^3 s, and DM is simply the integrated electron density along the line-of-sight given by,

$$\rm DM = \int_0^d n_e dl. \tag{1.22}$$

This frequency-dependent quadratic sweep is shown in Figure 1.6. Observations are typically made over a finite bandwidth with a larger bandwidth allowing more signal to be received which in turn makes the observations more sensitive. However if the dispersion delay is not accounted for, the integrated pulse becomes smeared which can be corrected for as explained in Section 2.2.1. The DM of pulsars together with the electron density models of the Galaxy are used to infer the distances to pulsars. The widely used "standard model" is the NE2001 model by Cordes & Lazio (2002) which accounts for the densities in the thick disk, thin disk, the central bulge, the Gum nebula and the spiral arms. This model does have a 50% uncertainty especially in the Galactic halo where the pulsar population is low and accurate distances are difficult to obtain. The distances inferred from the DMs can be calibrated against independently measured distances via HI absorption lines or parallax measurements. The DM is typically low at high latitudes averaging $\sim 70\,\rm pc\,cm^{-3}$ and can be as high as $\sim 1800\,\rm pc\,cm^{-3}$ towards the Galactic centre. Pulsars and RRATs are a Galactic population with all the observed DM accounted for by the Milky Way. FRBs on the other hand have been discovered primarily at high latitudes where the Galactic contribution to the observed DM is low, thereby indicating an extragalactic or cosmological origin.

1.5.2 Pulse scattering

The ISM is partially ionised, inhomogeneous and turbulent, exhibiting variations in concentration over a range of length scales. A short time duration pulse propagating

through such a medium will undergo multi-path propagation resulting in an exponential-like scattering tail on the trailing edge of the pulse. A thin screen model of irregularities of various scales can account for this observed pulse width broadening. A coherent pulse from a pulsar upon interaction with fluctuations along the path of propagation is scattered into multiple waves, each bent by an angle θ_0 forming an image broadened by angular diameter $2\theta_{\rm d}$. The angle θ_0 and the radius $\theta_{\rm d}$ are given by,

$$\theta_{\rm d} = \frac{\theta_0}{2} \approx \frac{e^2}{2\pi m_{\rm e}} \frac{\Delta n_{\rm e}}{\nu^2} \frac{\sqrt{d}}{\sqrt{a}} \tag{1.23}$$

where $\Delta n_{\rm e}$ is the variation in electron density, a is the length of the inhomogeneity and d is the distance to the source. However, it should be noted that there is strong evidence for the presence of a broad spectrum of length scales (Armstrong et al., 1995). The rays of light after interaction with the thin screen acquire an angular dependence resulting in a corresponding geometric time delay,

$$\Delta t(\theta) = \frac{\theta^2 d}{c} \tag{1.24}$$

which can be used to derive the observed intensity $I(t)$, and the scattering timescale $\tau_{\rm s}$ as,

$$I(t) \propto \exp(-c\Delta t/\theta_{\rm d}^2 d) \equiv e^{-\Delta t/\tau_{\rm s}}. \tag{1.25}$$

Hence, it is given by,

$$\tau_{\rm s} = \frac{\theta_{\rm d}^2 d}{c} = \frac{\rm e^4}{4\pi^2 m_e^2 c} \frac{\Delta n_{\rm e}^2}{a} \frac{d^2}{\nu^4} \propto d^2 \nu^{-4}. \tag{1.26}$$

We see that the scatter timescale is greatly dependent on the observing frequency, with larger scattering at lower frequencies. Equation 1.26 is an approximation for a single thin screen of turbulence. Clearly the ISM is made up of many such screens but most observational pulsar data agree well with a thin screen model as it can replicate the exponential scatter tails seen in pulsars. The scatter timescale increases with distance and DM and has been quantified by Bhat et al. (2004) using a large sample of pulsars. This is given by

$$\log\tau_s = a + b\,(\log{\rm DM}) + c\,(\log{\rm DM})^2 - \alpha \log\nu, \tag{1.27}$$

where the values of the coefficients are $a = -6.46$, $b = 0.154$, $c = 1.07$ and $\alpha = 3.86 \pm 0.16$ (see Figure 4.5 in Chapter 4). These values are obtained from a fit to the pulsar data. It should be noted that there is at least an order of magnitude scatter around this equation

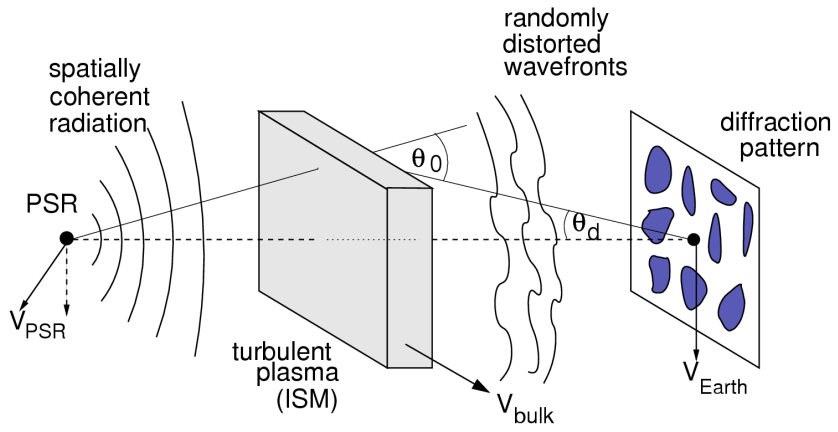

Figure 1.7 The figure displays the standard thin screen scattering model of pulsars as depicted in Lorimer & Kramer (2012). A radio signal that encounters an inhomogeneous plasma screen along its path of propagation midway between the source and observer, will get distorted and deflected upon interaction. This produces a scatter-broadened exponential tail and a scatter-broadened image of the source. Figure taken from Lorimer & Kramer (2012).

(Bhat et al., 2004).

1.5.3 Interstellar scintillation

Interstellar scintillation in pulsars is analogous to the twinkling of stars in the optical. This short-term variation in brightness is attributed to the constructive and destructive interference caused by the multi-path propagation of the signal through turbulent, ionised concentrations in the ISM. Scintillation is seen as the densities in the ISM move by the Earth, and the timescale of the intensity of the fluctuations depend on the relative velocities of the densities in the ISM, the pulsar, and the Earth. The resulting interference pattern has a variety of phases Φ due to the different path lengths of the deflected rays exhibiting a characteristic phase difference (Rickett, 1977) of

$$\delta\Phi \sim 2\pi\nu\tau_{\rm d}. \tag{1.28}$$

Interference can occur only if the following condition is satisfied:

$$2\pi\Delta\nu\tau_{\rm s} \sim 1, \tag{1.29}$$

where $\Delta\nu$ is the 'decorrelation bandwidth' or 'scintillation bandwidth' and is the typical

bandwidth of correlated intensity fluctuations for a source. The above condition implies that the scintillation bandwidth scales as $\Delta\nu \sim 1/\tau_{\rm s} \propto \nu^4$ (from equations 1.26 and 1.29). The interstellar turbulence can be described by a power law model relating the strength of the fluctuations along a given LOS ($C^2_{\rm n_e}$) to the spectral index β by,

$$P_{\rm n_e}(q) = C^2_{\rm n_e} q^{-\beta}, \tag{1.30}$$

resulting in a Kolmogorov spectrum where $\beta = -11/3$ (Armstrong et al., 1995) and q is the three-dimensional wavenumber (Lorimer & Kramer, 2012). The sizes of the turbulent regions vary between 10^9 and 10^{13} cm giving rise to two different branches of scintillation – (a) diffractive and (b) refractive. Diffractive scintillation is typically caused by turbulence of length scales of $10^9 - 10^{10}$ cm with short duration intensity fluctuations of order seconds to minutes. This is commonly seen in pulsars. Refractive scintillation conversely, is due to turbulence of larger length scales of $10^{12} - 10^{13}$ cm with longer duration intensity fluctuations of the order hours to days or months. This is observed in distant quasars (Burke & Graham-Smith, 2014).

1.5.4 Faraday Rotation

Magnetic fields play pivotal roles in many aspects of astrophysics ranging from star formation to galactic dynamics. They also have a significant contribution to the hydrostatic balance in the ISM. Unfortunately much remains unknown about how these fields are generated or how they are evolving. Polarisation studies are precisely what is required to answer these questions of magnetogenesis. The magnetic field B, of the Galaxy has been studied through synchrotron emission, optical starlight polarisation, Zeeman splitting of spectral lines and Faraday rotation (Noutsos et al., 2008). The main challenge that most of these methods face arises from the fact that they only provide the orientation of B. Zeeman splitting, unlike these methods, measures both orientation and direction of B. A drawback of the Zeeman splitting approach is the long integration times required. Faraday rotation of polarised sources has proven to be a powerful probe of B by providing a measure of the strength and direction of the LOS component of the field. An important advantage of Faraday rotation is the fact that its effects are strong in the radio part of the electromagnetic spectrum. This indicates that we can ignore interstellar extinction and thus probe magnetic fields out to cosmological distances.

Linearly polarised light can be split into two circular components of opposite handedness. Faraday rotation is caused as the phase velocity of the two circularly polarised electric field components differs in a magnetised plasma, effectively rotating the

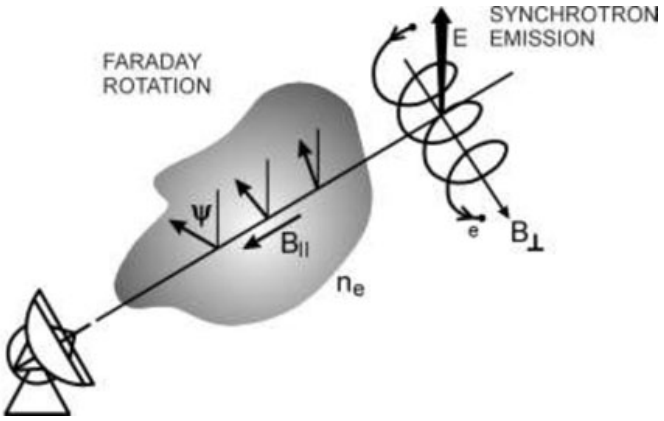

Figure 1.8 Block diagram showing the Faraday rotation occurring in the ISM. The polarised radiation from a source upon interaction with a cloud of magnetised plasma undergoes Faraday rotation causing the plane of polarisation to be rotated by an angle. This angle is measured at the telescope and is used to estimate the LOS component of the magnetic field. Image taken from Beck & Wielebinski (2013).

plane of polarisation. The measurement of the electric fields using orthogonally polarised feeds (linear or circular) basically translates to Stokes parameters, in a radio telescope. The Stokes parameters describe the polarisation properties of the radio source: I (total intensity), Q and U (linear polarisation) and V (circular polarisation). The polarisation position angle (PA) is calculated per frequency sub band as,

$$\chi = \frac{1}{2}\tan^{-1}\frac{U}{Q} \tag{1.31}$$

from which the RM is derived as a fit to the PA per frequency sub band (i.e.)

$$\Delta\Psi_{\rm PA} = {\rm RM}\,\lambda^2, \tag{1.32}$$

where RM is the rotation measure

$${\rm RM} = \frac{e^3}{2\pi m_{\rm e}^2 c^4}\int_0^D n_e\, B_{||}\cdot dl, \tag{1.33}$$

and has units $\mathrm{rad\,m^{-2}}$, where n_e is the electron density in particles per cubic metre, B is the vector magnetic field parallel to the LOS in microgauss (μG) and dl is the elemental vector towards the observer along the line-of-sight. Pulsars are well distributed throughout the volume of the Galactic disk and typically have substantial linear polarisation making Faraday rotation relatively easy to measure. Over the last two decades, several successful attempts have been made to map the Galactic magnetic field

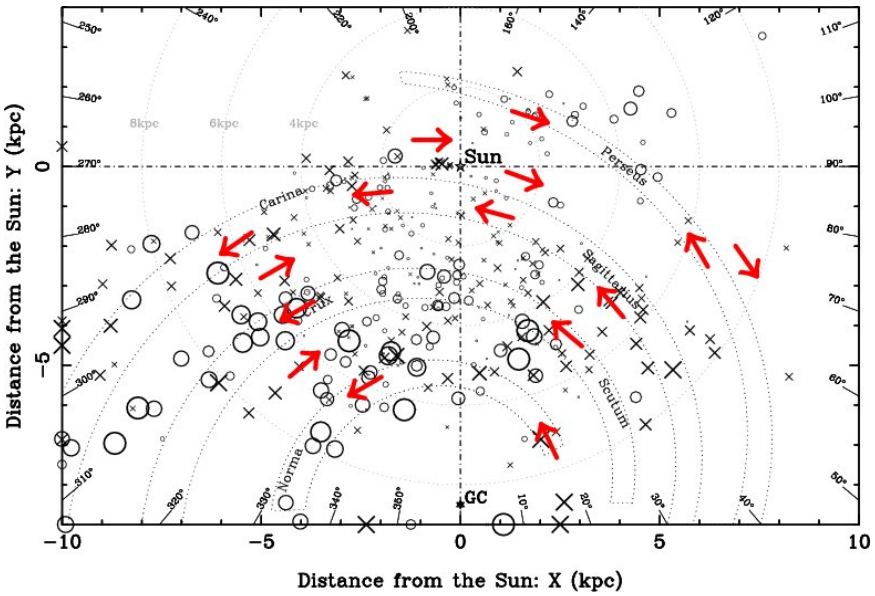

Figure 1.9 The RM distribution of 374 pulsars projected onto the Galactic plane. The crosses represent positive RMs, and the open circles represent negative RMs. The approximate locations of four spiral arms are indicated and our position at the Sun by the star. The large-scale structure of magnetic fields derived from pulsar RMs are indicated by red arrows. Figure taken from Han et al. (2006).

through pulsar RM measurements. These remarkable maps have provided evidence for a clockwise-directed field in the inter-arm regions and a counterclockwise-directed field along the arm regions shown in Figure 3.4, typically in the μG regime (Han et al., 2006). This is however still a hotly debated topic.

Gould & Lyne (1998) studied a sample of 300 pulsars at 600 and 1400 MHz and found the average degree of linear $\langle L/I \rangle$ and circular polarisation $\langle |V|/I \rangle$ to be 20 percent and 10 percent respectively. Considerable variation is observed around these mean values with individual pulses being up to 100 percent linearly polarised. A combination of the DM and RM from equation 1.33 – quantities that are both easily measured for polarised, pulsing radio sources – was first used by Lyne & Smith (1989), to determine the average magnetic field along the LOS weighted by the local free electron density,

$$\langle B_{\parallel} \rangle \simeq 1.232 \left(\frac{\mathrm{RM}}{\mathrm{rad\,m^{-2}}} \right) \left(\frac{\mathrm{DM}}{\mathrm{pc\,cm^{-3}}} \right)^{-1} \mu\mathrm{G}. \tag{1.34}$$

Since FRBs are highly energetic pulses of highly likely coherent emission of very short duration, they may well be polarised. Of the 27 known FRBs, only 8 have polarisation information (Petroff et al., 2015a; Masui et al., 2015; Keane et al., 2016; Ravi et al.,

2016; Petroff et al., 2017, Bhandari et al., submitted): and the fact that only Stokes I is recorded in typical searches. A method to determine single pulse RMs and its applicability to FRBs is discussed in Chapter 3. If FRBs are indeed cosmological, the total RM would be a combination of different contributions

$$\mathrm{RM_{tot}} = \mathrm{RM_{Gal}} + \mathrm{RM_{IGM}} + \mathrm{RM_{int}} \tag{1.35}$$

where, $\mathrm{RM_{gal}}$ is the "smooth" Galactic component assumed to typically vary with l and b over angular scales larger than the intersource separation, $\mathrm{RM_{IGM}}$ is the contribution from the IGM in the form of galaxies or filaments of cosmological large-scale structures along the LOS and $\mathrm{RM_{int}}$ is the "intrinsic" component from magnetised plasma associated with the source and its immediate environment and/or elsewhere in a host galaxy. In such a cosmological case, the RM along the LOS will be reduced by a factor of $(1+z)^2$ as,

$$\mathrm{RM}(z) = 8.1 \times 10^5 \int_0^z \frac{n_e(z)\, B_{||}(z)}{(1+z)^2} \cdot \frac{dl}{dz}\, dz \tag{1.36}$$

due to the redshifting of the observed frequencies. It should be noted that the average magnetic field along the LOS can be affected by: 1) The presence of electron density inhomogeneities along the sight line such as a hot nebula or HII region will dominate and causes the magnetic field to be overestimated. 2) Field reversals of 180° could occur along the sight line similar to the ones we see between the spiral arms of the Milky Way (Han et al., 2006). In both cases the large scale magnetic field along a given LOS cannot be accurately estimated.

1.6 Thesis Outline

This thesis primarily focuses on fast transients (FRBs and RRATs) that occur on timescales of milliseconds and the methodology adopted to detect them in surveys in real-time. The thesis is organised as follows.

Chapter 2 describes the technical details of the two telescopes, the Molonglo Observatory Synthesis telescope and the Parkes radio telescope, used for the observations and surveys in this thesis. We describe the transient pipelines deployed at these two telescopes, to detect single pulses and the projects they are currently being used in. I have developed the transient pipeline for FRB searches at the Molonglo Observatory Synthesis telescope.

In **Chapter 3** I present the first rotation measures of 18 known RRATs using polarisation analyses of their single pulses. The weighted average of the single pulse RM

distribution was found to be consistent with the RM of the total integrated pulse. This method was developed as part of a pilot study to investigate its applicability to FRBs. It was proven robust and I have applied the method to several FRBs.

Chapter 4 details Monte Carlo simulations of a cosmological population of FRBs to estimate their detection rates at UTMOST based on the discovery rate at Parkes. We model the source count distribution of the FRBs detected in the high latitude sub-survey of the high time resolution Universe survey at Parkes and find the slope of the distribution to be consistent with a cosmological origin. We also model the integral source count distributions of FRBs for different fractional sensitivities of UTMOST and at Parkes for the multi-beam receiver and the phased array feed (PAF) receiver. UTMOST is seen to dominate the FRB detection rate due to its sensitivity and massive field-of-view.

Chapter 5 presents the first two FRB surveys performed at UTMOST as part of its commissioning science. These surveys were carried out at $\sim 7\%$ and $\sim 14\%$ of target sensitivity. Several pulsars were detected via their single pulses but the survey however yielded no FRBs. This enabled us to place an upper limit on the all-sky rate of FRBs at 843 MHz. We also set a lower limit on the mean spectral index of FRBs.

Chapter 6 reports on a third FRB survey undertaken at UTMOST at $\sim 14\%$ of target sensitivity resulting in the first interferometric detections of 3 FRBs. The detection with an interferometer ruled out local sources of interference as a possible origin placing them at $\gtrsim 10^4$ km. We also constrain their positions to 1σ narrow ellipses that are $5' \times 2^\circ$. The rate of FRBs at 843 MHz is several times higher than expected, scaling from detections with the Parkes radio telescope assuming a flat spectral index and a Euclidean distribution. We examine how this can be explained by FRBs having a steeper spectral index and/or a flatter integral source count distribution than is often assumed.

Finally in **Chapter 7**, I review the major scientific results of this thesis and discuss the future of FRB science and the prospects that future sensitive wide-field experiments hold for it, such as the Canadian Hydrogen Intensity Mapping Experiment (Bandura et al., 2014) and the Square Kilometer Array (Macquart et al., 2015).

2

Instrumentation and data acquisition

In this chapter we present the technical details of the UTMOST and Parkes radio telescopes and the software used for detections of events. This includes the hardware upgrades at UTMOST and the implementation of the single pulse detection systems at both telescopes.

2.1 Fundamentals of radio interferometry

The angular resolution of a single dish antenna of diameter D operating at a wavelength λ is $\sim \lambda/D$. Consequently, even the largest single dish antennas with diameters of 300 - 500 metres have resolutions of only a few arcminutes setting the fundamental limit for localisation and resolution of fine structure. Much higher spatial resolution can be obtained by combining coherently, two or more single dish antennas into an array as an interferometer. Interferometers have fields-of-view (FOV) equivalent to that of their constituent dishes if they are all of the same diameter. Interferometers can be thought of as the equivalent of a virtual single dish antenna whose diameter is equal to the maximum distance of separation between the individual smaller antennas. This virtual aperture is typically but not always sparsely sampled and hence has a much lower gain compared to an aperture filled single dish antenna of the same diameter.

The simplest interferometer is a pair of radio telescopes separated by a projected "baseline" R (see Figure 2.1). Geometric and instrumental delays due to different path lengths and cable lengths respectively, are corrected for in the input signals of each antenna which are then coherently summed to yield an improved spatial resolution on the sky in a "tied-array beam". In the context of this thesis, each antenna produces an output voltage, all of which are then amplified, channelised, delay corrected, coherently added, square law detected and time-averaged in tied-array beams. Multiple tied-array beams (a.k.a fan-beams) are formed by replicating the input signals from the various antennas and

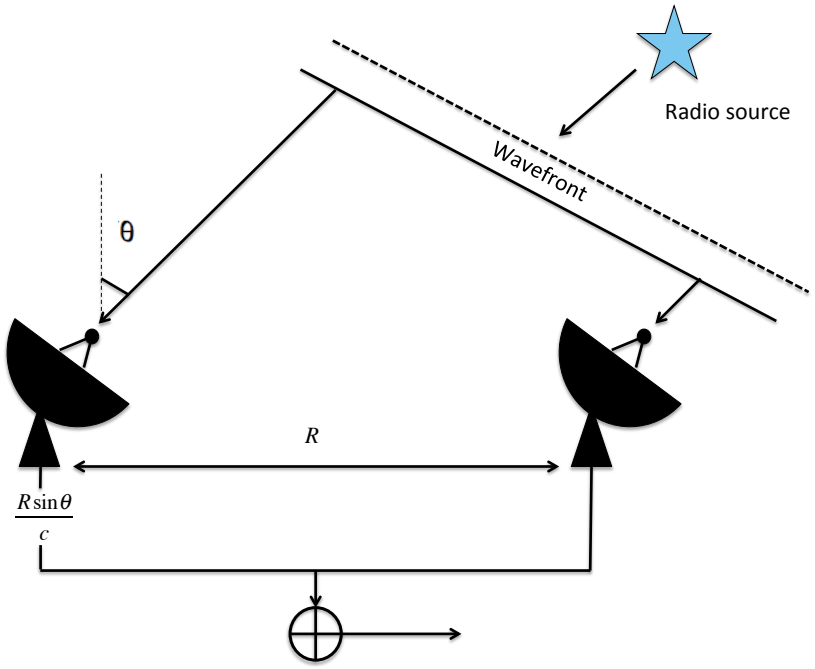

Figure 2.1 Schematic of a two element interferometric beamformer. Geometric and instrumental delays are applied to the input signals of each antenna which are then coherently summed in the required direction to yield the maximum response.

summing them with the application of different phase offsets, each with high directivity in a particular direction inside the large primary FOV. This increases the filling factor of the FOV. Each beam can now be regarded as an incoming signal from a single antenna and can be imparted to the backend for transient searches.

2.2 The Molonglo Observatory Synthesis Telescope

The Molonglo Observatory Synthesis Telescope (MOST) is a mile long interferometer of the "Mills Cross" design situated 40 km South-East of Canberra, Australia and has been operated on site since 1964. The telescope is well known for its discovery of the Vela pulsar (Large et al., 1968) and the Second Molonglo Pulsar survey which discovered 155 new pulsars effectively doubling the known population at that time (Manchester et al., 1978). Molonglo was also responsible for many catalogues of the Southern sky like the MOST Supernova Remnant Catalogue (MSC ; Whiteoak & Green, 1996) and the Sydney University Molonglo Sky Survey (SUMSS ; Bock et al., 1999). A transient detector installed on Molonglo in the late 1980's detected millisecond duration radio pulses

originating at least $>$ 1000 kms away with a rate of order 1.8×10^4 events sky^{-1} day^{-1} (Amy et al., 1989). These pulses however remained unidentified due to the lack of frequency resolution (1 frequency channel) at the telescope which prevented the measurement of a DM and hence the inability to distinguish between RFI and astrophysical signals. This rate is intriguing, as it is comparable to the rate of FRBs (see Section 1.4) estimated by Thornton et al. (2013).

The MOST consists of two parabolic cylinders 11.7 m wide and 778 m long separated by a 15-m gap. It was substantially modified in the early 1980s to make the East-West (E-W) arms fully steerable and increase the operating frequency to 843 MHz and a 3 MHz bandwidth (Robertson, 1991). A focal line feed system of 7744 right circularly polarised ring antennas operate at a central frequency of 843 MHz. These antennas are coherently summed in resonant cavities, 22 at a time along the focal line of the paraboloid, and fed to 352 Low Noise Amplifiers (LNAs). The working of the telescope is similar to that of a diffraction grating, with the circular dipoles analogous to the slits. Plane waves from a source at infinity reflect off the parabolic surface before reaching the antennas on the feed line. The telescope is thus effectively an array of 352 receivers or "modules" each with a beam of $4.64^\circ \times 2.14^\circ$ (EW-NS) operating at a system temperature of $\sim$ 100 K (Campbell-Wilson et al., 1997). In FRB search mode, the central 4.0 degrees of the 4.6 degree (half-power width) primary beam is tiled in the E-W direction by 352, elliptical, coherent, tied array beams (called 'fan-beams', each $46''$ wide), spaced $41''$ apart and overlapping at very close to their half power points at 843 MHz. In the N-S direction the resolution of the fan-beams is the same as that of the primary beam (2.1 degrees). The fan-beams are numbered from 1 to 352 running from East to West across the primary beam, with fan-beam 177 directly centred on boresight. Four adjacent modules are linked together digitally to form a "bay" and 44 such bays constitute one arm. The E-W arms can be tilted North-South (N-S), while E-W pointing is attained by differential rotation of the ring antennas (spaced at 0.54 λ) on the line feed. The telescope can access the whole sky south of $\delta = +18^\circ$, although hour angle coverage is best limited to an E-W tilt of $\pm 60^\circ$ due of gain losses. The telescope is currently being upgraded both in the backend receivers and with the installation of a new graphics processing unit (GPU) based correlator, in a collaboration between Sydney and Swinburne Universities. The installation of high-performance GPUs at MOST has transformed it into a powerful instrument, the Swinburne University of Technology upgrade for the MOST (UTMOST[1] ; Bailes et al., submitted). This has enlarged the FOV to twice that of the Sydney University Molonglo

[1]UTMOST is not an acronym

Sky Survey (SUMSS ; Bock et al., 1999) due to processing data from each 'module' rather than each 'bay'.

A block diagram of the system is shown in Figure 2.2. The right circularly polarised ring antennas in each module detect radiation and transmit the signals to a resonant wave guide chamber which is similar to a bandpass filter and is only resonant to a particular bandwidth. The signals from 4 independent LNAs are then sent to a bay's "RX box" or digital receiver which is fitted with commercially sourced analogue 3G and 4G forward link filters to block the local telecommunications phone bands at 890 MHz and 750 MHz and retain a 820 to 850 MHz band-limited signal. These signals are then down-converted and 8-bit complex sampled at 100 MHz before being sent down four optical fibres to the Polyphase Filterbanks (PFBs) to the control room where the data are processed by the UTMOST software correlator backend. A PFB is usually implemented using field programmable gate arrays (FPGAs) where the operations are highly parallelized and encoded in hardware. They are used to separate the signal into a predetermined number of frequency channels. Currently the system produces 128 channels, each 100/128 MHz (781.25 kHz). We select 40 of these 128 channels to pass to the data acquisition servers as shown in Figure 2.2. The data are written to disk at 655.36 μs time resolution for each of the individual frequency channels in a format called "filterbank".

The gain of each module is ~ 0.01 K Jy^{-1}. When added coherently on the meridian, the 352 modules of the antenna combine to have a gain of 3.5 K Jy^{-1}. Presently (November 2016) the system temperatures of the best performing modules is estimated, to be of order 100 K (Bailes et al., submitted). The system temperature does presently vary considerably from module to module, as sources of self-generated radio frequency interference are still being identified and removed in the ongoing upgrade. The LNAs contribute 20-30 K (as measured in the laboratory) to the total system temperature, with the remainder coming from a variety of sources including mesh leakage, cable feeds, etc. As of November 2016, we estimate the average system temperature to be 400 ± 100 K.

2.2.1 Dedispersion

As discussed in Section 1.5.1 a pulse is dispersed as it propagates through the tenuous ISM plasma. This effect needs to be removed to maximise the S/N of the original pulse. The effects of dispersion can be corrected for by splitting the observing bandwidth into independent frequency channels and applying appropriate time delays to each frequency channel so as to remove the quadratic sweep and make the pulse arrive at the same time in

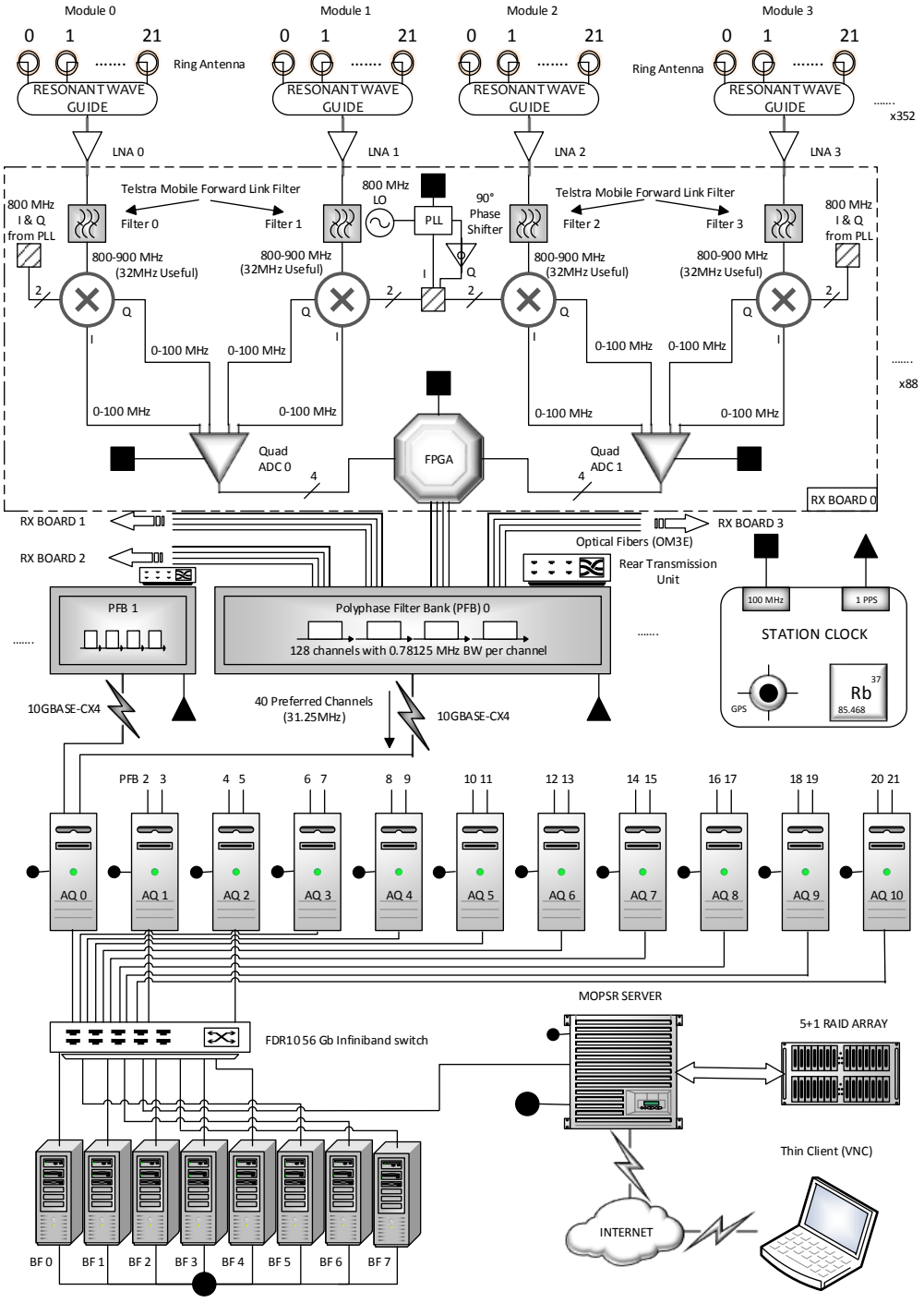

Figure 2.2 The data from the ring antennas are down-converted by the LNAs and sent to the PFBs through optical fibres for the data to be processed by the UTMOST correlator. The data are written to the filterbank format with 655.36 µs time resolution (Bailes et al., submitted).

each channel (see Figure 1.6). This is called dedispersion. Dedispersion can be classified into two types: 1) Incoherent dedispersion and 2) Coherent dedispersion.

1. *Incoherent dedispersion*:
   Pulsars being broadband emitters, cause the pulse to be smeared across the channel/band thereby lowering the S/N of the pulse and the probability of it being detected by the backend. The intra-channel smearing across a narrow frequency channel of the observing band is given by,

$$\tau_{\rm DM} = 8.3\,{\rm DM}\,\Delta\nu\,\nu^{-3}\,\mu s \tag{2.1}$$

   where $\Delta\nu$ is the channel bandwidth in MHz and ν is the observing frequency in GHz, dictates the effective width of an event, depending on the observed DM. Dispersion smearing degrades the effective time resolution of the pulse and the effect grows stronger with decreasing observing frequency. The integer sample shift to de-disperse the pulse can be calculated by re-writing Equation 1.21 as,

$$k(l) = \left(\frac{t_{\rm samp}}{\mathcal{D}}\right)^{-1}\left(\frac{\rm DM}{\rm pc\,cm^{-3}}\right)\left[\left(\frac{\nu_l}{\rm MHz}\right) - \left(\frac{\nu_1}{\rm MHz}\right)\right]^{-2} \tag{2.2}$$

   where $t_{\rm samp}$ is the sampling rate and ν_l is the frequency channel for which the time samples are shifted with respect to the highest frequency channel ν_1. The data format used at the UTMOST is the "filterbank" format[2] which is a 2-D array of samples $\mathcal{R}(\nu_1, t_{\rm j})$, at frequency ν_l and time $t_{\rm j}$. To produce a de-dispersed time series $(\mathcal{T}_j)$, the data are summed in frequency channels as,

$$\mathcal{T}_j = \sum_{l=1}^{n_{\rm chan}} \mathcal{R}(\nu_l, t_{j+k(l)}). \tag{2.3}$$

   Incoherent dedispersion is a post-detection technique (i.e. the phase information of the signal is no longer available). Since the DM of the source in blind surveys is not known *a priori*, a large range of trial DMs needs to be searched. The step size between the trial DMs searched is chosen such that the maximum smearing given by Equation 2.1 caused by dedispersing at the wrong DM (e.g. if the true DM value lies between 2 trial values) is no more than the smearing within a single channel. Following Lorimer & Kramer (2012), the ith value of the DM is,

[2] `http://sigproc.sourceforge.net/`

$$\mathrm{DM}_i = 1.205 \times 10^{-7}\,\mathrm{cm}^{-3}\,\mathrm{pc}\,(i-1)t_{\mathrm{samp}}(\nu^3/\Delta\nu) \tag{2.4}$$

where ν is the centre frequency in MHz, $\Delta\nu$ is the total observing bandwidth in MHz and t_{samp} is the sampling time in ms. When the value of $i = 1$, it corresponds to the "zero DM" time series, which is the combination of all the frequency channels without the appropriate time delays applied. This is frequently used to identify and excise sources of interference. Search pipelines generally increase the DM stepsize with increasing DM since the smearing within a channel increases with DM thereby allowing the effective time resolution to be maintained. Furthermore, to save computational power, down-sampling is employed by adding adjacent samples together when the channel smearing becomes larger than the sampling time, thereby reducing the needed time resolution and processing time.

2. *Coherent dedispersion*:
   In this method, the effects of dispersion are usually corrected for in the raw voltages i.e. before it is "detected". Dedispersion is performed under the assumption that the delays are represented by the convolution of the raw voltage and a transfer function with a frequency dependent phase (Hankins & Rickett, 1975; Hotan et al., 2004; Lorimer & Kramer, 2012). Given the filter response, the original signal can be deconvolved using an inverse filtering function, from the detected voltage. Though computationally intensive, coherent dedispersion yields the maximum time resolution possible for a given bandwidth. It is most useful in high precision timing experiments and the studies of microstructures in slow pulsars.

2.2.2 Radio frequency interference excision

Radio Frequency Interference (RFI) has been a major hindrance since the dawn of radio astronomy due to its often overwhelming brightness compared to the faint emission from celestial objects. UTMOST operates in the frequency range that is also shared by Australia mobile phone networks like Telstra and Vodafone, causing certain discrete bands of the data to be affected. These mobile signals present themselves as $\sim$ 5 MHz narrowband events with varying strength across the frequency spectrum typically during the hours associated with peak periods of telecom activity. Short pulses of 20 milliseconds in duration are almost always present as these are used by phones to register with the local phone tower. Stringent efforts to curtail the effects of RFI on the

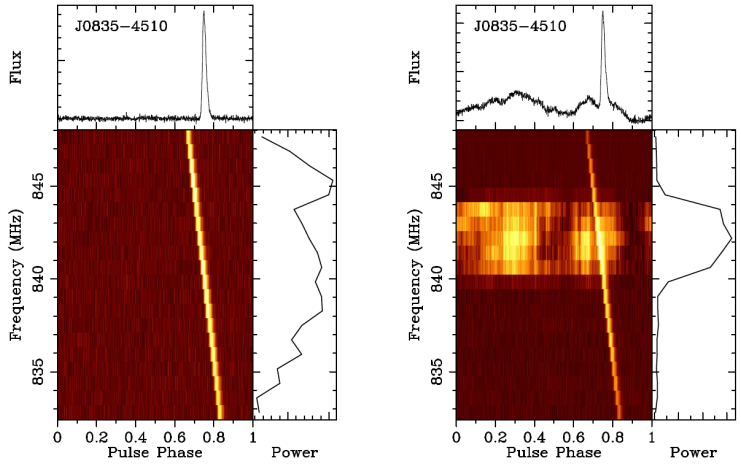

Figure 2.3 Figure from Bailes et al., submitted showing on data taken from a single module of the pulsar Vela with a phone call occurring during the observation. Left: The standard UTMOST RFI rejection procedures were implemented. Right: The data were processed without RFI excision (Bailes et al., submitted).

data have been implemented at UTMOST, as follows. In general, good radio data are statistically well represented by Gaussian random noise unlike mobile phone transmissions which lead to non-Gaussian distortions in the voltages. The spectral kurtosis approach (Nita & Gary, 2010a,b) measures the similarity between the input signal and Gaussian noise and identifies sudden deviations in total power. Single modules operate at $T_{\rm sys} \sim 100$ K and have a system equivalent flux density of 10^4 Jy which makes it unlikely to disregard celestial signals if there is a large percentage of increase in total power in a short time. The total power technique monitors and measures the median and median standard deviation for the preceding 8 seconds of data to determine when RFI causes the power levels to exceed pre-defined limits. UTMOST thus offers two levels of protection against RFI. Figure 2.3 shows an example of our RFI excision techniques. The data in the first panel are cleaned using the standard RFI excision techniques of spectral kurtosis and total power thresholding, and are added coherently. The data in the second panel did not undergo any RFI excision and is evidently badly corrupted. Both techniques search for interference on timescales from 1 to 20 milliseconds, operating on 40 coarse channels and 352 modules of the telescope. Despite the measures implemented, phone calls do affect the data at times. On the whole however this is manageable and useful astronomical observations can be taken $\gtrsim 95\%$ of the time.

2.2.3 The "BURST" programme at UTMOST

The "BURST" programme at UTMOST is the search for fast radio transients primarily focussing on FRBs. For this programme we use a mode in which we tile our ~ 8 deg^2 primary beam with 352 narrow elliptical tied-array beams or "fan-beams". The fan-beams are aligned uniformly E-W across the full-width half-power of the primary beam. The positional accuracy is $\approx 46''/(\mathrm{S/N})$ in the E-W direction and 2.1° in the N-S direction. This mode has been tested using pulsars and has been used to survey the sky for FRBs and RRATs. Since May 2015 we have commenced surveys for singe pulses over a wide range of DM trials (0 - 2000 pc cm^{-3}) primarily to detect FRBs. The results are the topics of Chapters 5 and 6. Our FRB search pipeline operates entirely simultaneously with other science modes, such as pulsar timing, map-making or transient searches. Predicted numbers of FRB events per year as a function of redshift z are shown in Figure 2.4, assuming that they are cosmologically distributed. At full sensitivity we might expect to detect an FRB every week of integration time (see Chapter 4). The estimated higher discovery rate at UTMOST over the current discovery rate of ~ 12 d event^{-1} at Parkes, is primarily due to UTMOST's large FOV (14× the Parkes multibeam receiver) and near 24/7 access to the facility (Bailes et al., submitted; Caleb et al., 2016b) unlike Parkes which spends only $\sim 10-20\%$ of the time-on-sky searching for FRBs. These offset the somewhat lower sensitivity to events at UTMOST (Parkes is approximately 3× more sensitive). UTMOST is currently part of the shadowing campaign for the SUrvey for Pulsars and Extragalactic Radio Bursts (SUPERB) collaboration at the Parkes radio telescope to search for FRBs. Simultaneous detections of FRBs with both telescopes would aid in localising bursts more precisely than either telescope could do on its own and also obtain crucial information regarding their spectra. Simultaneous detections of the RRAT J1819−1458 with known spectral index, at both telescopes (see Figure 2.5) validated the sensitivity of UTMOST during its upgrade (Keane et al., 2017).

2.2.4 The UTMOST transient pipeline

The sensitivity of UTMOST to FRB events (i.e. single pulse events) can be calculated using the radiometer equation,

$$S_{\mathrm{min}} = \beta \frac{\mathrm{S/N_{min}}\,(T_{\mathrm{sys}})}{G\sqrt{\Delta\nu\, t\, n_{\mathrm{p}}}} \tag{2.5}$$

where S_{min} is the minimum detectable flux density for a given minimum signal-to-noise (S/N), β is the digitisation factor, $\Delta\nu$ is the bandwidth in Hz, n_{p} is the number of

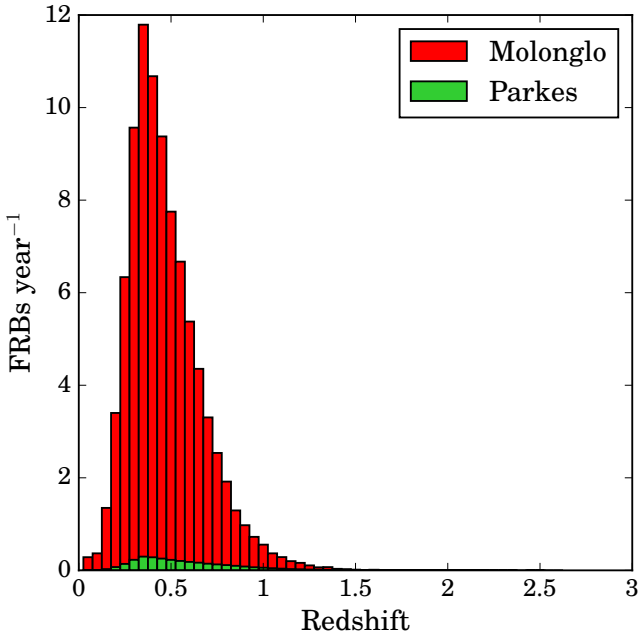

Figure 2.4 FRB rate as a function of redshift for events at Parkes (green histogram) versus a predicted rate at UTMOST operating at design sensitivity (red histogram), under the assumptions that they are flat spectrum sources, cosmologically distributed and that the DM is a proxy for redshift (from simulations by Caleb et al. (2016b) detailed in Chapter 4). The much higher number detected at UTMOST than at Parkes is driven primarily by the large FOV (~ 8 deg^2 versus 0.55 deg^2 at Parkes) and assumed high duty cycle at UTMOST to search for FRBs. It should be noted that the values of redshift are biased towards the host galaxy DM contributions being sub-dominant.

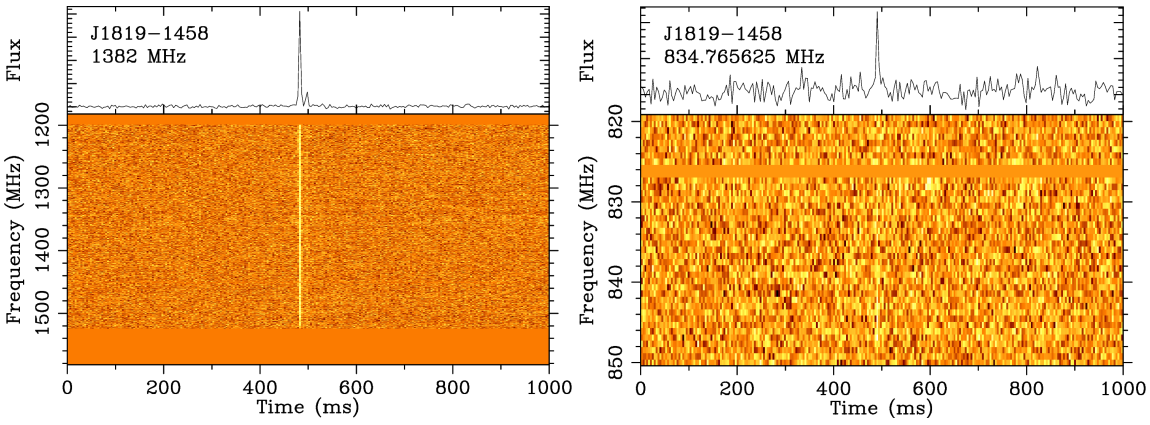

Figure 2.5 Simultaneous detections of the RRAT J1819−1458 with UTMOST and Parkes as part of the SUPERB shadowing campaign. Left: Parkes detection at UTC 2015-10-19-06:16:33 with S/N ~ 100 at L-band. Right: UTMOST detection at UTC 2015-10-19-06:16:34 with S/N ~ 11 at 843 MHz. This validated UTMOST's sensitivity during the ongoing upgrade (Keane et al., 2017).

polarisations, t is the width of the pulse in seconds, $T_{\rm sys}$ is the effective system temperature in K, and G is the system gain in K Jy^{-1}. For a pulse with S/N of 10 and width of 1 ms at UTMOST, $S_{\rm min} = 1.6$ Jy which is the minimum detectable flux density assuming the telescope specifications at design sensitivity (i.e.) $T_{\rm rec} = 100$ K, $\Delta\nu = 31.25$ MHz and $G = 3.52\,{\rm K\,Jy^{-1}}$.

Identifying pulses in a survey requires searching over different widths and a wide range of DMs in S/N as a function of time. Several codes exist to perform these searches like DEDISPERSE_ALL[3], DESTROY[4] and HEIMDALL[5]. The UTMOST transient pipeline is based on a custom design of the HEIMDALL single pulse search pipeline (Bailes et al., submitted). The original HEIMDALL software was developed by Ben Barsdell and is computationally fast as it uses graphics processing units (GPUs) (Barsdell, 2012). The use of GPUs for the operation of de-dispersion has resulted in speeding up the process by a factor of 9 compared to what was previously achieved by a CPU (Barsdell, 2012).

HEIMDALL reads the data in "gulps" or "blocks" of 8.05 seconds each and searches each of them over a DM-pulse width space. The data are searched for pulses by dedispersing for all values of DM in a set of trial DMs between DM$_{\rm min}$ to DM$_{\rm max}$. The data are also searched for a range of pulse widths by convolving with a series of sliding boxcar filters (square pulse) of width $W = 2^n$ time samples where $n = 0, 1, 2, ..., 12$ to recover the maximum S/N. At UTMOST we use 66 DM trials between $0 - 2000\,{\rm pc\,cm^{-3}}$ and 13 pulse width trials between $(2^0 - 2^{12}) \times 0.65536$ ms. Consecutive gulps are read in with overlaps of, the sum of the maximum dispersive delay across the whole band (~ 2.8 s for DM $= 2000\,{\rm pc\,cm^{-3}}$) and the maximum width trial ($W = 0.89$ s), to prevent loss of pulses at the edges. A clustering algorithm adds together single pulses which are detected over a range of DMs close to the real value, to maximise the S/N. This reduces the number of candidates considerably, though it still results in a few thousand candidates over the 352 fan-beams.

The results are written to an ASCII file which contains the information for all fan-beams such as S/N, time, width, DM and primary beam of detection of the pulses. This list typically consists of a few thousand candidates. This is further filtered by running a "coincidencer" to minimise RFI and get rid of those that appear in multiple fan beams at the same instance of time. The result of the coincidencer is a final list of hopefully unique candidates which are processed and analysed to look for true celestial pulses. A detailed description of the pipeline can be found in Chapter 5.

[3] `http://sigproc.sourceforge.net/`
[4] `https://github.com/evanocathain/destroy_gutted`
[5] `http://sourceforge.net/projects/heimdall-astro/`

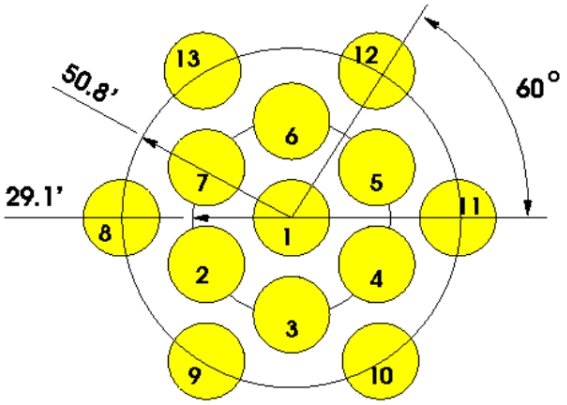

Figure 2.6 The 13-beams of the Parkes 21-cm multibeam receiver configuration is shown. The beams have a FWHM of $\sim 14.4'$. The inner hexagon beams 2-7 are separated radially from the central beam 1 by $29.1'$ while the outer hexagon beams 8-13 are separated radially from the central beam 1 by $50.8'$. The multibeam has a field-of-view of 0.55 deg^2. Image credit: ATNF (`http://www.atnf.csiro.au/research/multibeam/instrument/description.html`).

2.3 The Parkes radio telescope

The Parkes radio telescope is a 64-m dish situated 20 kms north of the town of Parkes in New South Wales, Australia, managed and operated by the Commonwealth Scientific and Industrial Research Organisation (CSIRO) as part of the Australia Telescope National Facility (ATNF) network of radio telescopes. It has been operational since 1961 and played an integral part in transmitting images of the Apollo 11 Moon landing in 1969. Of the many discoveries made at Parkes, an important one was the establishment of the source 3C 273 and hence all quasars, as being extragalactic objects. Parkes was also used to discover the first pulsar outside our Galaxy in the Large Magellanic Cloud. In 1991 Parkes presented the discovery of 10 millisecond pulsars in the globular cluster 47 Tucanae. Parkes primarily operates at 1.4 GHz with the 21-cm multibeam receiver (Staveley-Smith et al., 1996) which consists of a central feed horn surrounded by 2 hexagonal rings of 6 feed horns each. The beam of the central feed horn has a full-width half-maximum (FWHM) of $14'$ while the inner hexagon and the outer hexagon have beams of FWHM that are $14.1'$ and $14.5'$ respectively. Their gains also vary with radial distance with the central beam having a gain of 0.735 K Jy^{-1} and the inner and outer hexagons having gains of 0.690 K Jy^{-1} and 0.581 K Jy^{-1} respectively.

2.3.1 The Parkes transient pipeline

For the data and analyses in Chapter 3, the processing pipeline is shown in Figure 2.7. Data were recorded for a pilot study to analyse the single pulse polarisation of known RRATs and to test the Berkeley Parkes Swinburne Recorder (BPSR) full real-time polarisation dump system implemented in 2013 by Andrew Jameson. The sky positions of known RRATs were observed using the central beam 1 of the multibeam receiver. The 8-bit full polarisation data from two orthogonal linear feeds per beam is recorded for each of the 13 beams of the multi-beam receiver over 400 MHz bandwidth from 1182 to 1582 MHz with 1024 channels at 64 μs time resolution using the BPSR instrument. This is an FPGA based PFB instrument that was implemented in 2010 and is identical to the one used for High Time Resolution Universe surveys and the FRB discoveries reported in Thornton et al. (2013); Petroff et al. (2015a); Keane et al. (2016). The overall data processing using HEIMDALL is similar to that described in Section 6.2. Real-time searches for RRAT single pulses are performed as the data are recorded. An example visualisation of the real-time observations is shown in Figure 2.9. The linear polarizations are summed into a single 8-bit number and the gulps are read in overlapping sections of 16.77 seconds and are searched over a DM-width space with a clustering algorithm to group pulses together to maximise S/N. The processing of a gulp is ceased if the number of ungrouped candidates exceeds 10^6 and the processing of the next gulp begins. Additionally, the data from each of the 13 beams are merged and detections coincident in time are rejected. Further cuts are applied to further reduce the number of candidates namely

$$\begin{aligned} \mathrm{S/N} &\geq 10, \\ N_{\mathrm{beams}} &\leq 4, \\ W &\leq 32.768\,\mathrm{ms}, \\ N_{\mathrm{events}}(t_{\mathrm{obs}} - 2\mathrm{s} \rightarrow t_{\mathrm{obs}} + 2\mathrm{s}) &\leq 5, \end{aligned} \tag{2.6}$$

where the width criterion ensures only narrow pulses make it through and the last line of the equation 2.6 requires that there exists no more than five other candidates within a 4 second window around the candidate of interest. All this processing is done on average in under 10 seconds. A ring buffer in the backend (the HI-Pulsar Signal Processor) retains 120 seconds of 8-bit data from all 13 beams while the real-time processing is in progress. If the real-time HEIMDALL software identifies a candidate matching all the criteria listed in equation 2.6 it saves the 8-bit data in the buffer with the time window,

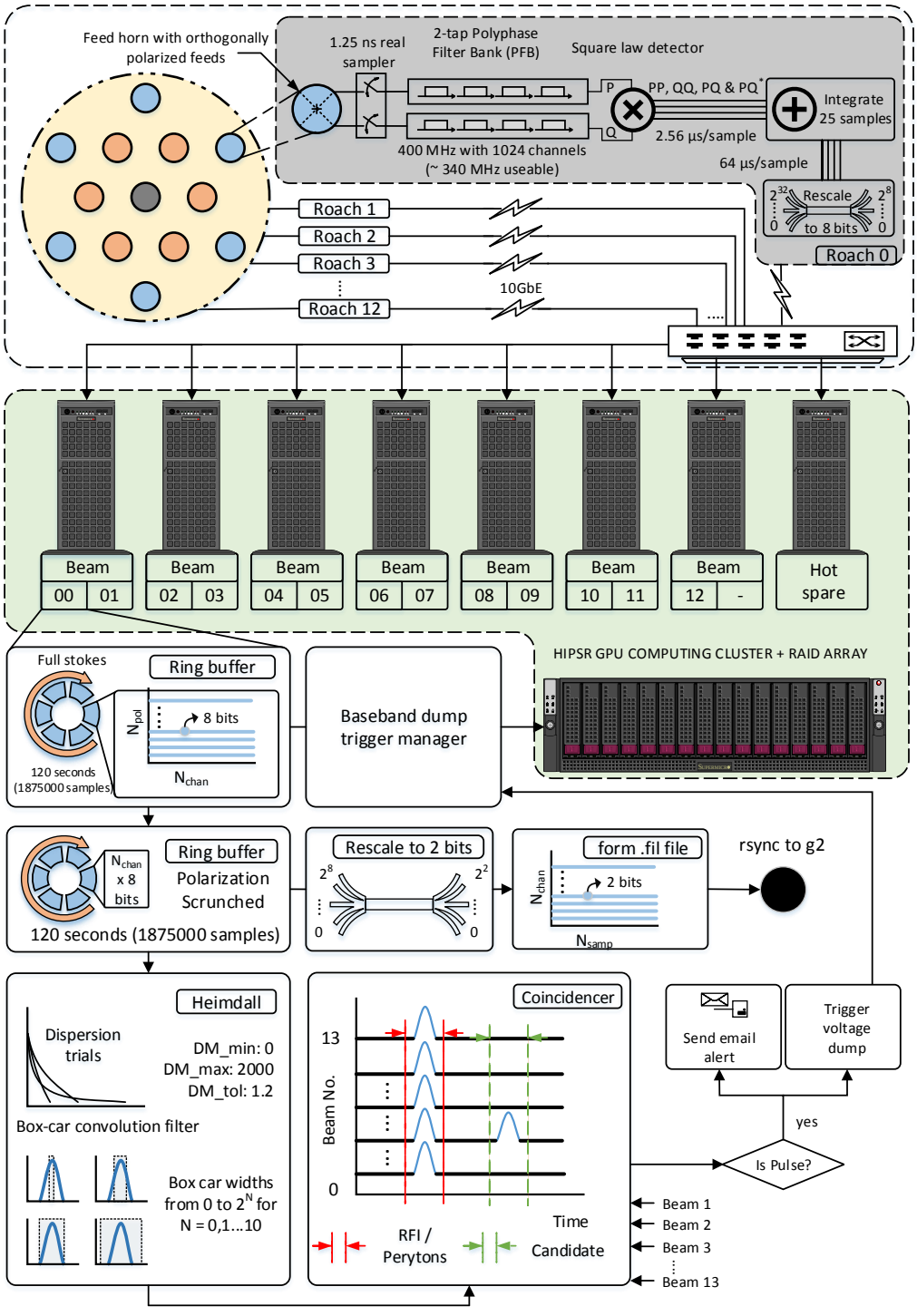

Figure 2.7 Block diagram of the pipeline used to detect RRAT pulses in real-time using the BPSR backend (Caleb et al., in prep). Data from the 13 beams of the Parkes 21-cm multi-beam receiver are recorded and searched live to identify pulses, using the HEIMDALL single pulse search software. A 120-s ring buffer is used to store the full-polarisation voltage data, which is dumped upon identification of a candidate that passes the tests in Equation 2.6. Image credit: Vivek Venkatraman Krishnan. To appear in Caleb et al., in prep

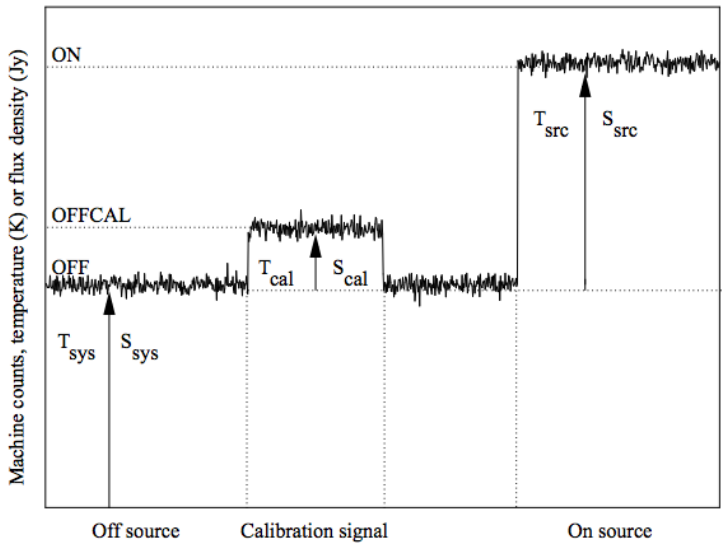

Figure 2.8 The system temperature and flux density relationship from Lorimer & Kramer (2012).

$$t_0 - \Delta t \leq t \leq t_0 + 2\Delta t \tag{2.7}$$

where t_0 is the time at which the event occurred at the highest frequency of the observing band, t is the time elapsed since the start of the observation and Δt is the dispersive delay across the whole band (see equation 1.21). The backend and pipeline were successfully tested using RRAT single pulses in 2013 and has since been used to discover 8 FRBs in real-time (Petroff et al., 2015a; Ravi et al., 2015; Keane et al., 2016; Ravi et al., 2016; Petroff et al., 2017, Bhandari et al., submitted).

2.4 Calibrating pulsar data

In radio astronomy, the raw data recorded during observations are typically quantised and designed to be compact and are initially uncalibrated. The processing of the data is not "truly" complete without the conversion of the arbitrary "machine units" to flux density in Janskys through calibration (Lorimer & Kramer, 2012). The following sections discuss the methodology for polarisation and flux calibration.

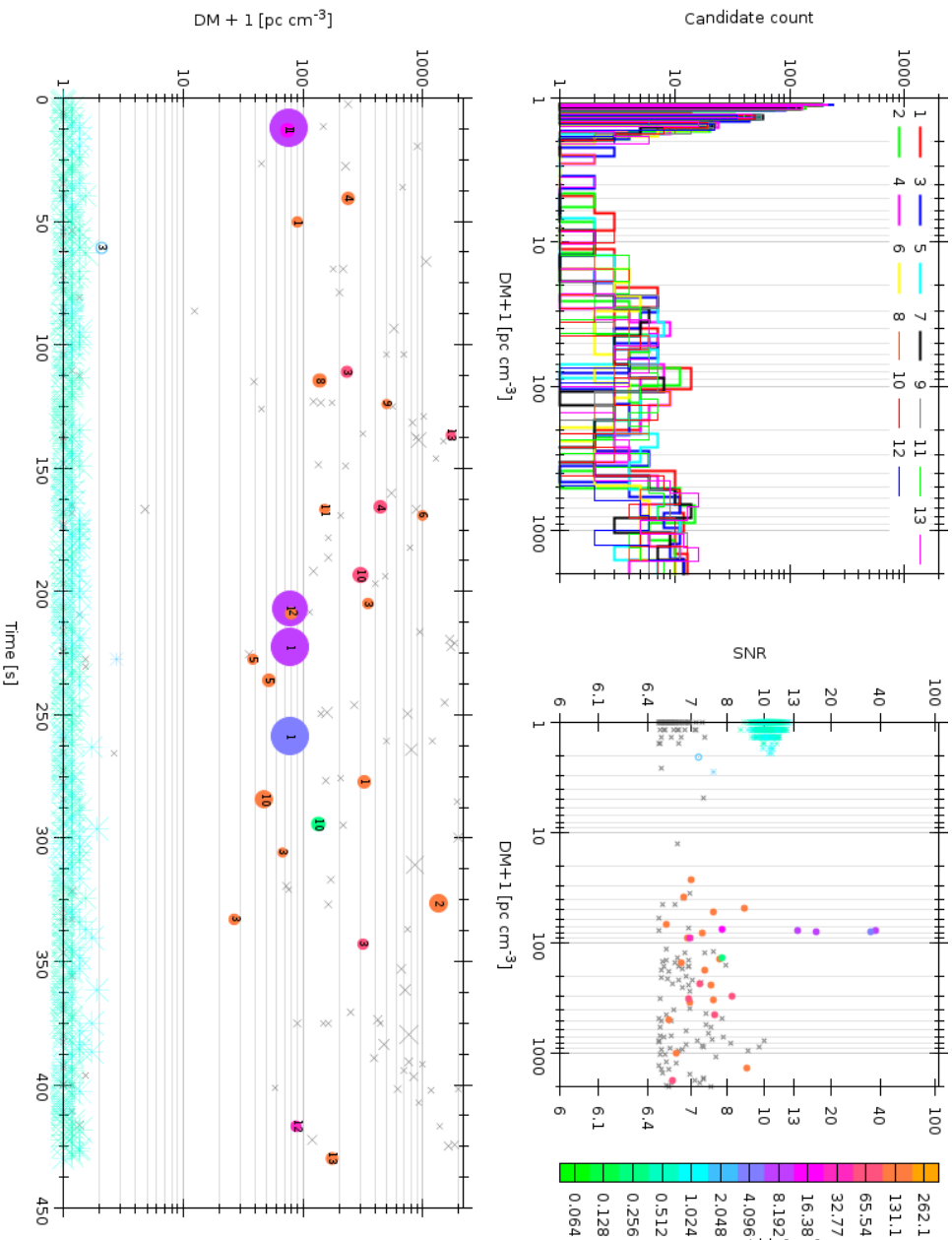

Figure 2.9 An overview plot of the candidates produced in a HEIMDALL search of an observation of RRAT J1129−53. Top left: Candidate histograms for all 13 beams over the DM range searched. Top right: Scatter plot of DMs vs S/N of all candidates. Bottom: Plot of time vs DMs of candidates. The size and color of the filled circles represent the S/N and width of the events with the number representing the beam number. The filled circles marked with the number 1 at a DM of 77.0 pc cm^{-3} represent pulses from PSR J1129−53. All other markers represent spurious RFI candidates that appear in multiple beams.

2.4.1 Polarimetric calibration

Polarisation measurements and anaylses are vital to improving our comprehension of not only the propagation and emission of radio waves but also the medium through which they propagate. For instance, Faraday rotation studies in the ISM have enabled the measurements of the Galactic magnetic fields along the LOS (Han et al., 2006; Noutsos et al., 2008). At Parkes, each of the 13 beams of the multi-beam receiver is equipped with two orthogonal linearly polarised receptors to measure the electric field vectors $E_{\rm x}$ and $E_{\rm y}$ of the X and Y components of the incoming radiation. The polarisation state of a radio signal can be described by the Stokes parameters as,

$$\mathcal{S} = \begin{bmatrix} I \\ Q \\ U \\ V \end{bmatrix} \tag{2.8}$$

where I is the total intensity, Q and U are the linearly polarised components of I and V is the circularly polarised component of I. All Stokes parameters are the sums and differences of the self and cross products of the measured electric field vectors given by,

$$\begin{aligned} I &= E_{\rm x}^2 + E_{\rm y}^2 \\ Q &= E_{\rm x}^2 - E_{\rm y}^2 \\ U &= 2E_{\rm x}E_{\rm y}{\rm cos}\phi \\ V &= 2E_{\rm x}E_{\rm y}{\rm sin}\phi \end{aligned} \tag{2.9}$$

where ϕ is the relative phase difference between the two components. The total intensity of the signal can be written as,

$$I = \sqrt{Q^2 + U^2 + V^2}. \tag{2.10}$$

For a purely linearly polarised wave, $V = 0$ while $V/Q = 1$ for a right circularly polarised wave and $V/Q = -1$ for a left circularly polarised wave. The intrinsic state of polarisation of a source undergoes changes in its phase and amplitude due to effects such as Faraday rotation in the medium along the path of propagation, parallactic angle rotation and other effects relating to the backend system and telescope. Examples include feed rotation with respect to the sky and irregularities in the amplifier chain. The intrinsic Stokes vectors $\mathcal{S}_{\rm i}$ can be described as a product of observed Stokes vectors $\mathcal{S}_{\rm o}$ with a 4×4

Mueller matrix $\mathcal{M}$ encapsulating all the effects detailed above:

$$\mathcal{S}_{\rm i} = \mathcal{M} \times \mathcal{S}_{\rm o}. \tag{2.11}$$

Following Heiles et al. (2001), the combined Mueller matrix $\mathcal{M}$ can be expanded as,

$$\mathcal{M} = \mathcal{M}_{\rm Amp} \times \mathcal{M}_{\rm CC} \times \mathcal{M}_{\rm Feed} \times \mathcal{M}_{\rm PA} \tag{2.12}$$

where the subscripts denote parallactic angle, cross-coupling, feed and amplifier. The non-commutative nature of Equation 2.12 necessitates the matrix algebra be solved from right to left. In the first case, an 'alt-az' telescope like Parkes tracking a source across the sky causes the receiver feed to rotate with respect to the plane of polarisation of the incoming signal given by the parallactic angle. During observations, a change in parallactic angle leads to a phase rotation of twice the parallactic angle of the Stokes vector. Parkes can however rotate the receiver to compensate for the changing parallactic angle. In the second case, the feeds may introduce a mixing of the incoming linear polarisation causing them to be elliptically polarised. This can be described by the ratio of the voltages of the polarisation ellipse α and the relative phase of the two voltages or the phase angle of coupling given by χ. In case of linear receptors, $\alpha = 0^\circ$ and $\chi = 0^\circ$. The imperfections in the system due to the receptors not being perfectly orthogonal can lead to cross-coupling between the polarisations given by the amplitude ϵ and phase ϕ. If the signal is transmitted through different amplifier chains, this additionally introduces a change in the voltage gain and a phase delay due to the different path lengths traversed given by $g_{\rm x}$, $g_{\rm y}$ and $\psi_{\rm x}$, $\psi_{\rm y}$ respectively. From these, the differential gain and phase can be estimated as $\Delta G = G_X - G_Y$ given $G = g^2$ and $\psi = \psi_x - \psi_y$ respectively. The Mueller matrix thus solves for $\alpha, \chi, \epsilon, \phi, \Delta G$ and ψ. There is additionally an angle $\theta_{\rm rot}$ by which the derived position angle must be rotated in order to conform with IAU astronomical definition. The combined Mueller matrix M expressed as,

$$\mathcal{M} = \begin{bmatrix} 1 & [-2\epsilon \sin\phi \sin 2\alpha + \frac{\Delta G}{2} \cos 2\alpha] & 2\epsilon \cos\phi & [2\epsilon \sin\phi \cos 2\alpha + \frac{\Delta G}{2} \sin 2\alpha] \\ \frac{\Delta G}{2} & \cos 2\alpha & 0 & \sin 2\alpha \\ 2\epsilon \cos(\phi + \psi) & \sin 2\alpha \sin\psi & \cos\psi & -\cos 2\alpha \sin\psi \\ 2\epsilon \sin(\phi + \psi) & -\sin 2\alpha \sin\psi & \sin\psi & \cos 2\alpha \cos\psi \end{bmatrix} \tag{2.13}$$

must be solved for these 7 independent parameters in order to estimate $\mathcal{S}_{\rm o}$ (Heiles et al., 2001). The calibration technique used in Chapter 3 however is an approximation based on

the ideal feed assumption (IFA) that the receptors are perfectly orthogonally polarized, and the reference source is 100% linearly polarized and illuminates both receptors equally and in phase. Flux calibration to convert all four Stokes vectors to a flux density scale in Jy can be done by using a reference radio source of known flux density and a noise diode as described in the following section.

2.4.2 Flux calibration

A signal is detectable only when it exceeds the noise fluctuations in the receiver system which according to Dicke & Beringer (1946) is defined as,

$$\Delta T_{\rm sys} = \frac{T_{\rm sys}}{\sqrt{\Delta\nu\, t\, n_{\rm p}}}. \tag{2.14}$$

The mean flux density of a source is the area under the pulse divided by its period and is routinely used to interpret the signal strength. The mean flux of a source can be estimated using,

$$S_{\rm mean} = \beta \frac{\rm S/N\, T_{\rm sys}}{G\sqrt{\Delta\nu\, t\, n_{\rm p}}} \tag{2.15}$$

where $\Delta\nu$ is the observing bandwidth in Hz, t is the observed width of the pulse in seconds, G is the gain in K Jy^{-1}, $T_{\rm sys}$ is the system temperature in K and $n_{\rm p}$ is the number of polarisations. The relationship between system temperature and flux density is shown in Figure 2.8. During observations, the flux of the source is recorded in arbitrary units. The most straightforward way to estimate the flux of a source without observing a calibrator is to firstly estimate the system noise. This can be obtained from Equation 2.15 as,

$$\Delta S_{\rm sys} = \beta \frac{T_{\rm sys}}{G\sqrt{\Delta\nu\, t\, n_{\rm p}}} \tag{2.16}$$

using $S_{\rm sys} = T_{\rm sys}/G$. The conversion to flux units is performed by multiplying the observed intensity by $S_{\rm sys}/\sigma$ where σ is the off-pulse rms.

The second method involves the observation of a source of known flux density ($S_{\rm src} = T_{\rm src}/G$) and constant spectral index over a wide range of frequencies to use as a reference, typically Hydra-A. Two measurements are made, with the telescope pointing at the source (ON) where the counts are proportional to the source plus the system noise, and when it is pointing at an empty patch of sky $\sim 1^\circ$ away from the source (OFF) which only represents the system noise as shown in Figure 2.8. The $T_{\rm sys}$ can then be calculated as,

$$\frac{T_{\rm src}}{T_{\rm sys}} = \frac{\rm ON - OFF}{\rm OFF}. \tag{2.17}$$

A more reliable method that is routinely used in pulsar observations is similar to the one described above but with the injection of a noise diode signal with the telescope pointed at an empty patch of sky (OFFCAL),

$$\frac{T_{\rm cal}}{T_{\rm sys}} = \frac{\rm OFFCAL - OFF}{\rm OFF} \tag{2.18}$$

where OFFCAL is the injection of the noise diode signal to the off-source observation. Combining the above equation with Equation 2.17 gives,

$$\frac{S_{\rm cal}}{S_{\rm src}} = \frac{T_{\rm cal}}{T_{\rm src}} = \frac{\rm OFFCAL - OFF}{\rm ON - OFF}. \tag{2.19}$$

This is used to determine a flux density scale by calculating $S_{\rm cal}$ using the $S_{\rm src}$ as a reference.

3

Single pulse polarisation studies of RRATs

In this Chapter, I present a method to determine the RMs of RRAT single pulses through Faraday rotation measure studies. In addition to yielding the first RM measurements of 18 known RRATs this method is also applicable to FRBs.

3.1 Introduction

The last decade in radio astronomy has seen the discovery of two similar yet distinctly different classes of radio emission: Rotating Radio Transients (RRATs) and Fast Radio Bursts (FRBs). RRATs are a category of moderately bright pulsars, exhibiting sporadic radio bursts of millisecond duration (McLaughlin et al., 2006). The most common definition of an RRAT applies to a neutron star that is more easily detectable in single pulse searches of data compared to periodicity searches. They exhibit extreme pulse amplitude distributions, such as in the giant pulses seen from the Crab pulsar. However, the emission processes (the process by which plasma is generated and flows in the magnetosphere) that lead to the bursts are not very well understood. This is not surprising given the open problem of radio emission in pulsars (Melrose, 1992; Mitra et al., 2015).

The FRBs (Lorimer et al. 2007; Thornton et al. 2013; Spitler et al. 2014; Burke-Spolaor & Bannister 2014; Petroff et al. 2015a; Ravi et al. 2015; Champion et al. 2016; Masui et al. 2015; Keane et al. 2016; Spitler et al. 2016; Caleb et al. 2017; Bannister et al. 2017; Bhandari et al., submitted) are the very first detections of possibly cosmological, coherent radio emission and have mostly been observed as one-off events. The pulses have been found to be similar in nature to the single pulses emitted by the RRATs and pulsars like Vela and the Crab in terms of their cold plasma dispersion sweeps and narrow pulse widths. However unlike the RRATs, Vela or the Crab, we are yet to detect more pulses

from all but one of the FRBs (with the exception of FRB 121102 reported in Spitler et al., 2016) despite extensive follow-up (e.g. Petroff et al., 2015b) and their nature remains an enigma. The distinguishing factor between these two classes of sources lies in their total observed DMs, with the Galaxy being able to fully account for the total observed DMs along the LOS in the case of RRATs. FRBs on the contrary have total observed DMs well in excess of the Galactic contribution along the LOS. Thus all the known RRATs have been asserted to lie within the Galaxy whereas the large excess DMs of the FRBs, imply they are extragalactic with inferred redshifts at cosmological distances (Keane, 2015). Also FRBs have implied peak luminosities of $\sim 10^{13}$ Jy kpc^2 (assuming upper limits on redshifts from Equation 1.16) compared to RRATs which have peak luminosities of ~ 10 Jy kpc^2 (see Figure 1.1). If, as is expected from a coherent emission mechanism, such high-energy short-duration pulses are polarised, they can prove to be unique probes of the extragalactic magnetic field through Faraday rotation studies.

The source J1819−1458 was the first RRAT to have its Rotation Measure (RM) derived, through polarisation observations (Karastergiou et al., 2009). The RM quantifies the amount of rotation undergone by the plane of polarised radiation, as the radio wave traverses the magnetised interstellar medium (ISM). This measurement was done using hundreds of single pulses over multiple epochs integrated into a single stable profile (Karastergiou et al., 2009) and has a large uncertainty (330 ± 30 rad m^{-2}). In this Chapter we discuss the possibility of using individual single pulses to determine the RMs of known RRATs and the prospect of applying this method to FRB pulses to determine the extragalactic magnetic field along the LOS. A thorough description of Faraday rotation in both the Galactic and cosmological cases can be found in Section 1.5.4.

Unlike previous works (e.g. Lyne & Smith, 1989; Han et al., 2006; Noutsos et al., 2008; Karastergiou et al., 2009) which used pulses integrated over many periods of the pulsar, the study conducted in this Chapter uses single pulse polarimetry to address two science goals simultaneously. It has helped determine the first ever RM measurements of 18 known RRATs using their sporadic single pulses whilst testing the possibility of applying the process to individual FRB pulses in the process. Since the FRBs are highly energetic pulses of very short duration, they might be assumed to be polarised. FRB RMs could then open up a whole new possibility to probe the extragalactic magnetic fields associated with the local environment of the FRB through polarimetry. Microgauss strength magnetic fields have been found to exist out to redshifts of $z \sim$ 1-2 (Widrow, 2002). These measurements are made by acquiring RMs for polarised sources at high-z (eg: AGNs and quasars). However intervening dense clumps and isolated HII regions along

the LOS contribute significantly to the overall RM value. FRBs are the first detections of coherent emission at possibly cosmological distances.

Only 18 of the 27 known FRBs (Burke-Spolaor & Bannister, 2014; Lorimer et al., 2007; Thornton et al., 2013; Champion et al., 2016; Masui et al., 2015; Petroff et al., 2015a; Ravi et al., 2015, Bhandari et al., submitted) exhibit scatter tails well in excess of what can be accounted for by the Milky Way along their LOS indicating an origin in either the turbulent IGM or ISM of a possible host galaxy or possibly something intrinsic to the source. Presently the DMs of coherent extragalactic sources are limited to the known pulsars in the Magellanic clouds (Manchester et al., 2001) and presumably a few FRBs. However only two published FRBs have a measured RM value (Masui et al., 2015; Ravi et al., 2016). Since the observed RM is the sum of multiple components along the LOS (see Equation 1.35), the crucial steps required to extract the extragalactic RM value are,

1. the subtraction of the foreground RM due to the various intervening components.

2. the subtraction of the contribution from the ISM of the host galaxy.

3. the subtraction of the contribution from the ionoshpere.

It should be noted that the RM contribution from the ionosphere is negligible at 1.4 GHz but however becomes crucial at lower frequencies. The SKA is the future of cosmic magnetism measurements. A large sample of FRB RMs if dominated by the IGM, and their corresponding redshifts via photometric and spectroscopic optical surveys could enable us to map the progression of the magnetic field of the Universe out to $z \sim 3$ (Gaensler, 2007). The SKA1's cosmic magnetism project (e.g. Johnston-Hollitt et al., 2015) aims to obtain a substantial number ($7 - 14$ million) of extragalactic RMs.

3.2 Observations and Analyses

Observations of single pulses from 18 known RRATs were undertaken as part of the P864 (PI: Caleb) project at the 64-m Parkes radio telescope. Only the bright RRATs with flux S>100 mJy and recorded burst rate were chosen from the RRATalog[1]. All pulses were detected in real-time using the HEIMDALL[2] software package and the data were recorded in full polarisation-mode using the Berkeley Parkes Swinburne Recorder (BPSR) and the fourth generation Parkes digital filterbank system (PDFB4) backends to enable pulse

[1] http://astro.phys.wvu.edu/rratalog/
[2] http://sourceforge.net/projects/heimdall-astro/

Table 3.1 Data for the 18 RRATs observed at Parkes in the period 2013 - 2016 as part of this thesis. Columns: (1) RRAT name based on J2000 coordinates; (2,3) Galactic longitude (l) and latitude (b); (4) dispersion measure value from the RRATAlog; (5,6,7) weighted average of the single pulse RM distribution, the 1σ scatter around it and the number of pulses in the distribution; (8,9) RM of the integrated pulse obtained by adding all the single pules in the distribution (column 7) and its corresponding error; (10) indicates the presence of orthogonally polarised modes (OPM) in the single pulses.

J2000 name	l	b	DM	Single pulse distribution			Integrated pulse		Remarks
	(deg)	(deg)	(pc cm^{-3})	RM (rad m^{-2})	1σ	Pulses	RM (rad m^{-2})	$\sigma_{\rm RM}$	
J0410−31	230.59	−46.67	9.2	15.3	5.8	6	15.0	1.6	
J0628+09	202.19	−0.86	88.0	119.5	15.5	7	113.4	7.8	Exhibits OPM
J0735−62	274.74	−19.21	19.4	–	–	1	−25.6	16.6	
J0837−24	247.45	9.80	142.8	355.4	3.9	2	367.3	7.2	
J0941−39	267.70	9.98	78.2	−70.4	18.4	16	−87.6	3.2	Exhibits OPM
J1129−53	290.80	7.41	77.0	−26.2	12.9	25	−27.3	4.0	Exhibits OPM
J1226−3223	296.90	30.19	36.7	−39.6	19.2	8	−48.4	1.2	Exhibits OPM
J1317−5759	306.43	4.70	145.3	177.7	8.1	9	183.8	14.3	Exhibits OPM
J1423−56	315.29	3.87	32.9	−8.0	3.0	4	−7.8	4.4	Exhibits OPM
J1513−5946	319.97	−1.70	171.7	104.0	12.0	9	95.4	5.9	
J1554−5209	329.01	1.19	130.8	−141.2	10.3	35	−132.7	10.1	
J1707−4417	343.04	−2.28	380.0	−661.3	14.4	4	−669.6	5.1	Exhibits OPM
J1753−38	352.25	−6.38	168.4	133.2	26.2	8	148.0	9.2	
J1819−1458	16.02	0.08	196	319.6	10.2	40	327.3	3.4	Exhibits OPM
J1840−1419	18.94	−4.12	19.4	58.44	17.1	23	79.7	5.0	Exhibits OPM
J1854+0306	35.88	0.83	216	−83.2	9.4	3	−96.9	16.2	
J1854−1557	19.02	−7.95	160	−61.0	15.7	2	−83.3	12.0	
J1913+1330	47.42	1.38	175.6	931.2	18.6	3	935.5	11.2	

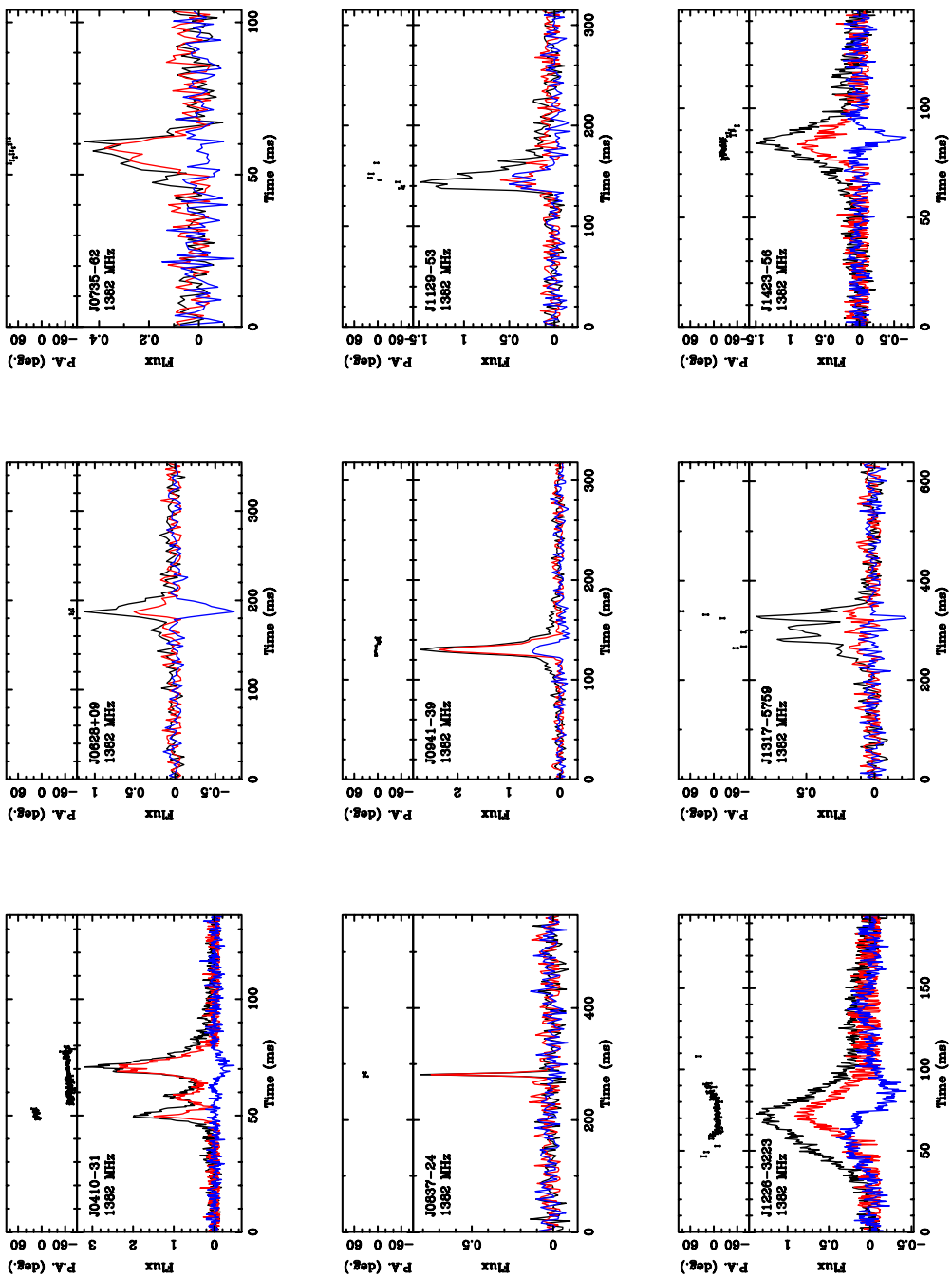

Figure 3.1 Polarisation profiles of the brightest pulses from individual RRATs. The black, red and blue lines represent the total intensity, linear polarisation and circular polarisation respectively. The top panel in each plot shows the PA variation as a function of pulse phase in ms. To appear in Caleb et al., in prep.

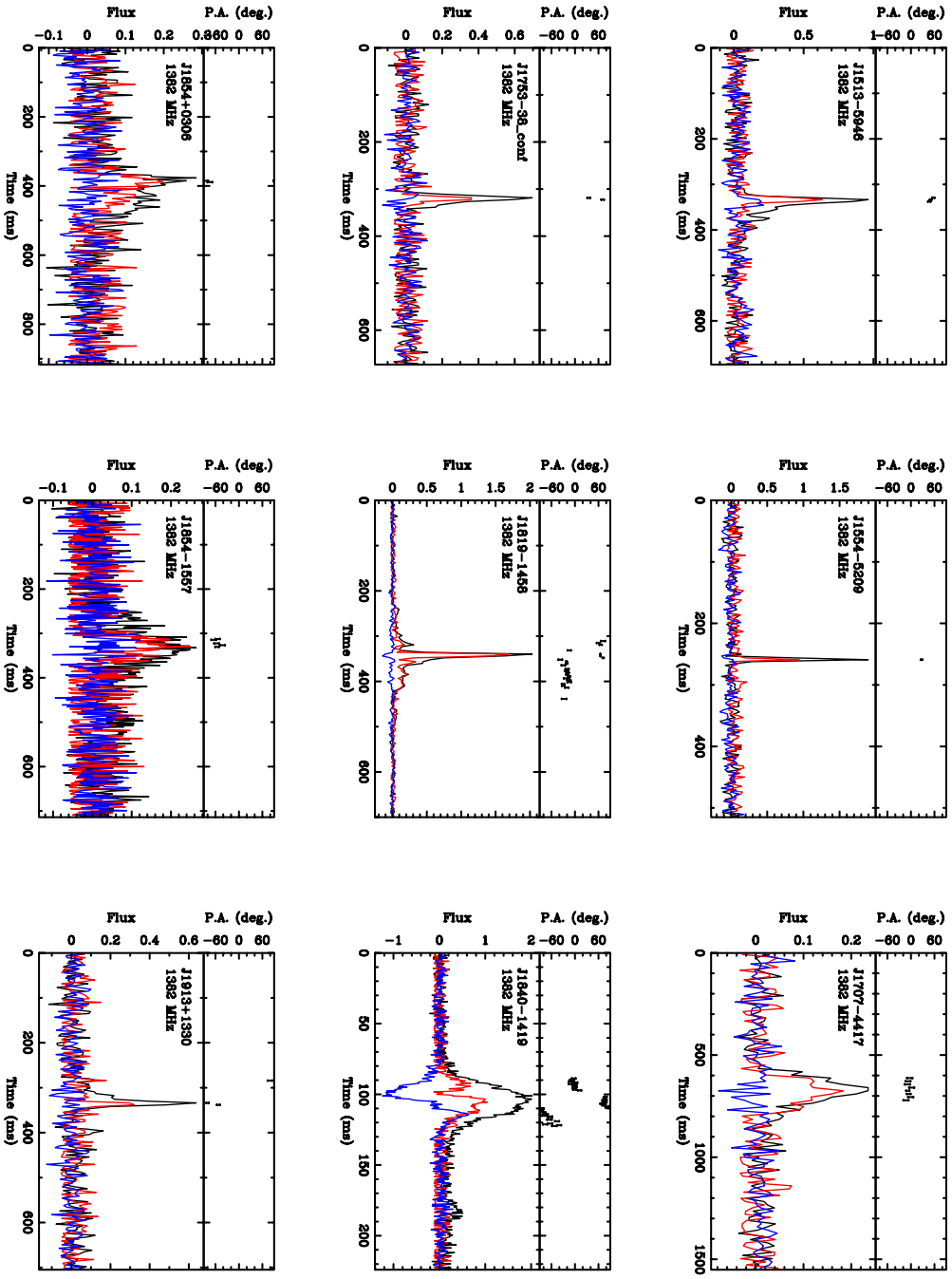

Figure 3.2 Polarisation profiles of the brightest pulses from individual RRATs. The black, red and blue lines represent the total intensity, linear polarisation and circular polarisation respectively. The top panel in each plot shows the PA variation as a function of pulse phase in ms. To appear in Caleb et al., in prep.

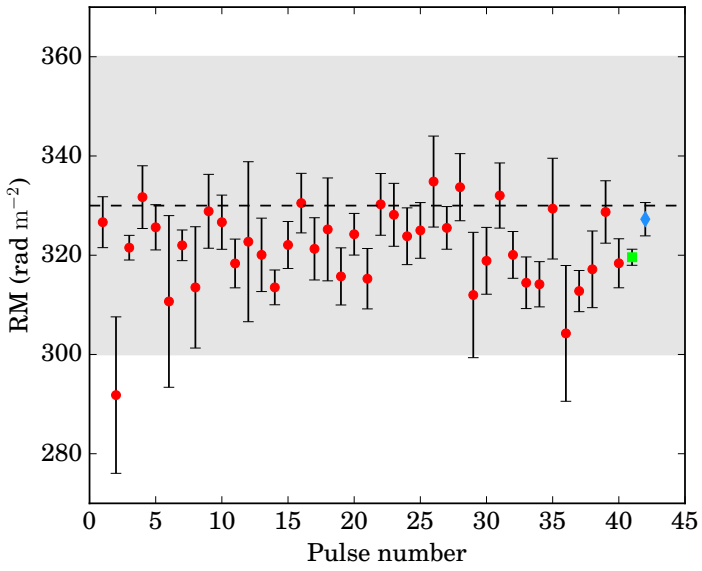

Figure 3.3 RM as a function of pulse number for J1819−1458 observed as part of the project P864 at Parkes between 2013 and 2016. The circles represent the RM of each single pulse observed as part of P864 whilst the star and diamond represent the RM of the weighted average of the single pulse distribution and the RM of the total integrated profile. The black dashed line represents the RM value published in Karastergiou et al. (2009) and the shaded region encloses the error region for all possible values of RM for J1819−1458. To appear in Caleb et al., in prep.

profile calibration and studies of the single pulse emission properties. The feeds in the 21-cm Parkes multibeam receiver have orthogonally polarised probes with a calibration probe placed at a 45° angle to the signal probes to enable the injection of a linearly polarised broad-band pulsed calibration signal. The linear polarisation for each pulse is summed into 8-bit data and is passed to HEIMDALL. If HEIMALL validates a pulse the corresponding 8-bit full Stokes data are saved to disk. The real-time transient pipeline searches for pulses across all DMs from $0 - 2000\,\mathrm{pc\,cm^{-3}}$ and pulse widths from $0.128 - 262$ ms. Only pulses with DM < 2000 pc cm^{-3}, S/N ≥ 10 and $W \leq 32.768$ ms are recorded to disk. All the observations reported in the paper have a total bandwidth of 400 MHz centred at 1382 MHz with 1024 channels across the band. A calibration of the gain and phase of the receiver system was done by recording the pulsed calibration signal for 2 minutes prior to each RRAT observation.

The offline data processing was performed using the PSRCHIVE pulsar data analysis package. To begin with, the data near the edges (∼15 percent of the total bandwidth)

on either side of the band were assigned zero weight and excised as they are known to be corrupted by digitisation artefacts. The data were then median smoothed and further cleaned using interactive excision. In keeping with the IAU/IEEE convention, for the Parkes 21-cm multibeam receiver we set the symmetry angle to $-\pi/2$ (van Straten et al., 2010). The data are calibrated using both the ideal feed assumption[3] and the measurement equation modelling mode of the polarisation calibration modelling[4]. A brute force search method was used for the RM determination. The data were summed from orthogonal observation pairs to produce the Stokes profiles for each sub-band. We determined the RM by integrating in frequency for a range of trial RMs of $\pm 1.18 \times 10^5\,\mathrm{rad\,m^2}$ in steps of roughly about 1 $\mathrm{rad\,m^2}$ and searching for a peak in the total linearly polarised intensity $L = \sqrt{Q^2 + U^2}$. The Stokes parameter profiles are produced for the upper and lower band profiles correcting for the RM value determined at the peak in the previous step. The best estimates of the RRAT RM were then obtained by taking the weighted mean PA difference between the two bands with the weight inversely proportional to the square of the error in PA difference for each pulse phase bin.

3.3 Results

Table 3.1 gives an overview of the results of the analyses. For each source, a distribution of the RMs of the single pulses was produced and an average weighted by the error in RM was determined. The single pulses that yielded an RM value were added together and the RM of the total integrated pulse also was determined using the offline data processing described in the previous section and compared with the weighted average of the distribution. Both values were found to be consistent within a 1σ uncertainty. It should be noted that not every observed pulse was sufficiently linearly polarised ($> 3\sigma$) to enable an RM measurement. To ensure the accuracy of our method, we compare in Figure 3.3 the RM value of each single pulse of the RRAT J1819−1458 and the RM of our integrated pulse, with the integrated total value published in Karastergiou et al. (2009). All the single pulse RMs are found to be in good agreement with the published value as shown in Figure 3.3. We obtain a weighted average RM of $320 \pm 2\,\mathrm{rad\,m^2}$ and a integrated pulse RM of $327 \pm 3\,\mathrm{rad\,m^2}$ for J1819−1458, which is consistent with the published value of $330 \pm 30\,\mathrm{rad\,m^2}$ (Karastergiou et al., 2009) with much smaller uncertainties. We thus conclude that single pulse RMs can be accurately measured. We note that we have ignored the effects of the ionosphere in our analysis and thus we

[3] `http://psrchive.sourceforge.net/manuals/pac/`
[4] `http://psrchive.sourceforge.net/manuals/pcm/`

slightly underestimate the RM uncertainty. This can be compensated for by adding in quadrature an error of 2 rad m^{-2} which is fairly typical at these frequencies. The duty cycles and Galactic distribution of RRATs have been analysed and compared with the canonical pulsar population and they have been seen to have similar distributions (see Figure 1.5) (Burke-Spolaor & Bailes, 2010). Figure 3.4 shows the RMs of the pulsars and RRATs in our Galaxy as a function of their DMs. The values of the pulsar RMs were obtained from the ATNF pulsar catalogue PSRCAT[5] and the RMs of the RRATs are from this work. We see that the RRAT population is distributed similarly to the overall pulsar population in our Galaxy.

The minimum S/N required to reliably determine an RM value was determined using the PSRSIM single pulse simulator from the PSRCHIVE software package. PSRSIM was fed a template of a single pulse of J1819−1458 to begin with (e.g.: number of channels, frequency, bandwidth, number of bins, etc.). For given values of S/N (S/N$_i$ = 25, 50, 75, 100) constant RM values (RM$_i$ = 10, 0, −10) were injected and the pulse profile was replaced with a fake pulse at given S/N$_i$ and the injected RM$_i$. By default, the pulse has a peak of 1 (unity) and the degree of linear polarisation is held constant at 40 percent as a function of pulse phase with no circular polarisation. We simulated 1500 such pulses, for every combination of S/N$_i$ and RM$_i$. Figure 3.5 displays the results of this simulation. As expected, we see the uncertainty in RM steadily decreasing with increasing S/N. An overall S/N of at least 50 is required to get a reliable error estimate on RM assuming 40 percent linear polarisation. The robustness of the RMFIT algorithm was tested by determining the mean and variance of the chi-square distribution of the pulses simulated with S/N$_i$ = 100 and RM$_i$ = 10. The resulting mean and variance of the chi-square distribution were 0 and 1 respectively with a weighted average RM and error values of 10.0 ± 0.07 rad m^{-2}.

3.3.1 Orthogonally Polarised Modes

Polarisation is key diagnostic of radio emission through emission geometry. In general the position angle (PA) of the linearly polarised flux varies in a regular and smooth manner throughout the pulse – a characteristic S-shaped curve explained by the Rotating Vector Model (RVM) (Radhakrishnan & Cooke, 1969) – and is independent of the observing frequency given by,

$$\tan(\psi - \psi_0) = \frac{\sin\alpha \sin(\phi - \phi_0)}{\sin\zeta \cos\alpha \; - \; \cos\zeta \sin\alpha \cos(\phi - \phi_0)} \tag{3.1}$$

[5] `http://www.atnf.csiro.au/people/pulsar/psrcat/`

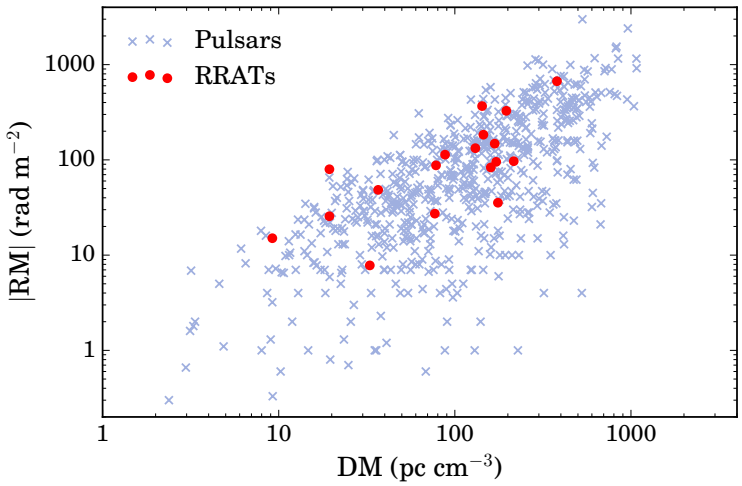

Figure 3.4 RMs of the pulsars and RRATs in our Galaxy as a function of DM. The RMs of the RRATs are distributed similarly to those of the pulsar population. To appear in Caleb et al., in prep.

where ψ and ψ_0 are the PA and offset in PA, ϕ and ϕ_0 are the pulse phase and offset in pulse phase, α is the colatitude of magnetic axis, ζ is the colatitude of the the LOS. Fits to this model allow us to constrain the magnetic axis inclination angle α with respect to the rotation axis, and the closest approach of the LOS to the magnetic axis β ($\beta = \zeta - \alpha$). Some RRATs were observed to exhibit orthogonally polarised modes (OPM) in their single pulses as shown in Table 3.1. The pulsar modelling programme, PSRMODEL[6] as part of the PSRCHIVE package was used to fit the RVM model to the linear polarisation data. PSRMODEL executes a two-dimensional fit to Stokes Q and U which are treated as the two components of a complex number with the phase of each number complex number indicating the PA predicted by the RVM model. Further analysis is required to determine RVM fits for the RRATs, and will be included in Caleb et al., in prep.

3.4 Discussion and Summary

In this chapter we present RM measurements of 18 known RRATs with peak flux densities S>100 mJy. The method used for the offline data processing is similar to the one used to measure RMs of FRB single pulses (Petroff et al., 2015a; Keane et al., 2016). As a sanity check, we compared the published RM of J1819−1458 (Karastergiou et al., 2009) with the weighted mean of our single pulse RM distribution and the RM of the integrated pulse profile and both values were found to be consistent within the uncertainties. To determine

[6] http://psrchive.sourceforge.net/manuals/pac/

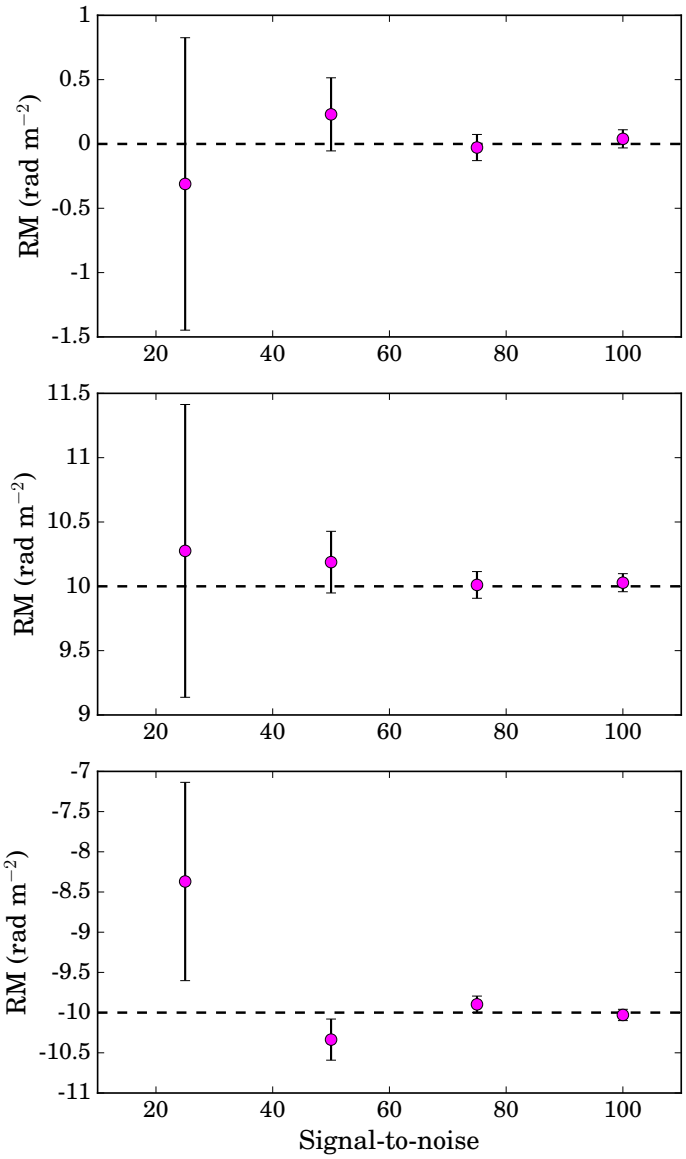

Figure 3.5 The Figure displays the RMs as a function of various simulated pulse S/Ns. In each subplot, the circles represent the weighted average RMs of all the simulated pulses at that S/N and the dashed line indicates the injected RM value. The weighted averages in all the plots are found to be consistent with the injected RM within the 1σ uncertainty. As expected, we see a steady decline in the RM uncertainty with increasing S/N. To appear in Caleb et al., in prep.

the minimum S/N required to accurately estimate the RM, we run simulations of mock RRAT pulses injected with a range of RMs of different magnitudes and a range of S/Ns. We conclude that we require a total S/N of at least 50σ with 40% linear polarisation to reliably estimate a RM value. Future work before publication of this analysis would require performing RVM fits to the sources that exhibit OPMs to try and understand their emission geometry and making fits to the pulse amplitude distributions to differentiate between a log-normal distribution and a high-energy power-law tail.

The method used in this paper has been applied to FRBs in Petroff et al. (2015a) and Keane et al. (2016). However, given the fact that these FRBs have been observed as one-off events with sub-threshold or no linear polarisation, no reliable estimate of an RM value has been made. The SUrvey for Pulsars and Extragalactic Radio Bursts (SUPERB) collaboration have been exploiting the sensitivity of Parkes to search for FRBs. Presently, there is one unpublished FRB with full polarisation information discussed in Chapter 7. However unlike the FRB reported in Masui et al. (2015) which indicates magnetisation in the vicinity of the source itself or within a host galaxy, the unpublished FRB is open to interpretation. Polarisation studies to determine RMs and RVM fits for FRBs could prove transformational to our understanding of FRB progenitors and their associated magnetic fields.

4

Are the distributions of fast radio burst properties consistent with origin in a cosmological population?

In this chapter (published as Caleb et al., 2016a) we present simulations of a cosmological population of FRBs based on models for their density distribution in space − one in which their comoving density is constant and the other in which their density is proportional to the star formation history of the cosmos. The simulations are based on assumptions consistent with observations of their energy distribution, their spatial density as a function of redshift and the properties of the interstellar and intergalactic media. We note that these quantities are interrelated as the energy and redshift distribution rely critically on converting the DM to a distance, which requires a trustworthy model for the properties of the ISM and IGM. We examine whether the dispersion measures, fluences, derived redshifts, signal-to-noise ratios and effective widths of known FRBs are consistent with a cosmological population.

4.1 Introduction

For all FRBs discovered to date, the arrival time delay associated with the dispersion closely follows a ν^{-2} frequency dependence, and the pulse width evolution follows a ν^{-4} frequency dependence for those FRBs where the S/N has permitted frequency-dependent width measurements (Thornton et al., 2013). Both properties are consistent with propagation through a sparse, non-relativistic plasma.

Four events were found by Thornton et al. (2013) in the high-latitude component of the High Time Resolution Universe (HTRU) survey at Parkes (Keith et al., 2010). From these events, a rate of $R_{\rm FRB}\left(\mathcal{F} \sim 3\,{\rm Jy\,ms}\right) = 1.0^{+0.6}_{-0.5} \times 10^4$ events sky^{-1} day^{-1} was estimated. If the redshifts ascribed to the bursts are valid, the volumetric rate to which

this corresponds is $\sim 2 \times 10^4$ events $\mathrm{Gpc}^{-3}\mathrm{yr}^{-1}$, which is similar to the volumetric rate for SGRs ($< 2.5 \times 10^4$ events $\mathrm{Gpc}^{-3}\mathrm{yr}^{-1}$), and within an order of magnitude of the volumetric rate of core collapse (Type II) supernovae ($\sim 2 \times 10^5$ events $\mathrm{Gpc}^{-3}\mathrm{yr}^{-1}$) (Kulkarni et al., 2014). No consensus has emerged regarding the progenitors of FRBs, with possibilities including annihilating black holes (Keane et al., 2012), giant flares from SGRs (Popov & Postnov, 2010; Thornton et al., 2013; Lyubarsky, 2014), binary white dwarf mergers (Kashiyama et al., 2013), neutron star mergers (Totani, 2013), collapsing supramassive neutron stars (Falcke & Rezzolla, 2014), radio emission from pulsar companions (Mottez & Zarka, 2014), dark matter induced collapse of neutron stars (Fuller & Ott, 2015) and the radio emission from pulsars (Cordes & Wasserman, 2016; Connor et al., 2016b). The leading theories are discussed in detail in Section 1.4.1. The difficulty in associating FRBs with sources at any wavelength other than radio, or with a host galaxy, is predominantly because of the large uncertainty in their positions — 14.4 arcmin is the full width at half maximum of the Parkes Multibeam receiver (Staveley-Smith et al., 1996). Petroff et al. (2015a) detected an FRB in real time at the Parkes radio telescope and triggered follow-up at multiple wavelengths with data from 12 telescopes. No counterpart was detected at any of the observed wavelengths. Part of the difficulty of finding a host or counterpart for this burst was the large position error due to Parkes' large primary beam size.

We present here simulations of a cosmological population of FRBs, under assumptions about their energy distribution, their spatial density as a function of redshift and the properties of the ISM and IGM (Section 4.2), finding they are broadly consistent with origin at cosmological distances. The analysis of the models and the results are discussed in Section 4.3, in comparison with data from the HTRU survey. We present $\log N$-$\log \mathcal{F}$ curves and discuss the FRB rates at Parkes and UTMOST in Section 4.4 and finally our summary and conclusions in Section 4.5.

4.2 Monte Carlo Simulations

The High Time Resolution Universe (HTRU) survey at Parkes samples the transient radio sky with 64 μs resolution at 1352 MHz and has a bandwidth of 340 MHz. The observing band is sub-divided into 390.625 kHz frequency channels. HTRU is composed of three sub-surveys at low, intermediate and high Galactic latitudes. The simulations in this Chapter are of the high latitude (Hilat) region of the survey — 34099, 270-sec pointings at declinations $\delta < 10^\circ$ — where 9 of the 27 known FRBs have been discovered (Thornton et al. 2013; Champion et al. 2016), and of the intermediate latitude (Medlat) region, which yielded no FRBs (Petroff et al., 2014). Petroff et al. (2014) and Hassall et al.

(2013) have carried out studies similar to ours, to model the detectability of FRBs using simulations and analytic methods respectively. Petroff et al. (2014) simulated the effects of dispersion smearing which is the pulse broadening caused by the adopted frequency resolution, interstellar scattering and sky temperature on FRB sensitivity at Parkes, in the Medlat region. Hassall et al. (2013) used analytical methods to derive the detection rates at various telescopes operating over a wide range of frequencies. Our simulations are of FRB events at cosmological distances under assumptions about their comoving density with redshift, and include the effects of ISM scattering, IGM scattering, dispersion smearing, sky temperature and telescope beam pattern. We produce estimates of the energy, fluence, S/N, pulse width, DM and redshift distributions for FRBs with our models, and compare them to the 9 FRBs detected in Hilat. We perform two classes of simulations:

1. in section 4.2 we generate sufficiently many surveys such that the Poisson noise of the averaged simulations in Figures 4.1 and 4.2 is negligible compared to the noise of the 9 hilat events,

2. in section 4.3.4 we generate thousands of short runs with an average of 9 events per simulation to estimate and compare the slopes of their log$N$-log$\mathcal{F}$ curves with the slope of the log$N$-log$\mathcal{F}$ curve of the 9 hilat FRBs.

For simplicity, FRB events in our simulations are assumed to be radiating isotropically[1] at the source with a flat spectrum to be consistent with what is seen at 20-cm with Parkes. Their intrinsic energy distribution is assumed to be log-normal, although this is not a critical assumption. A power-law gives similar results. We adopt a ΛCDM model with matter density $\Omega_m = 0.27$, vacuum density $\Omega_\Lambda = 0.73$ and Hubble constant $H_0 = 71$ km s^{-1}Mpc^{-1} (Wright, 2006). The comoving number density distribution of FRBs in the simulations is assumed to be either a constant, or proportional to the cosmic star formation history (SFH). We adopt the SFH from the review paper of Hopkins & Beacom (2006) as typical of cosmic SFH measurements, which show a rise in the star formation rate of about an order of magnitude between the present ($z = 0$) and redshifts of $z \sim 2$ (see their Figure 1). It has the parametric form $\dot{\rho_*} = (a+bz)h/[1+(z/c)^d]$ where $h = 0.7$, $a = 0.0170$, $b = 0.13$, $c = 3.3$ and $d = 5.3$ (see their Section 4). We do not explicitly set the comoving number density of FRBs in the simulation: we compute the maximum in the product of SFH and comoving volume of each shell of width dz as a function of z, and generate Monte Carlo events under this function. This allows the simulation to generate

[1] If we assume a beaming fraction of 4π, it would imply a shift to lower energies by about an order of magnitude will have no significant effect on the results and conclusions of the paper.

events at the maximum rate, which is important as our run times can be quite long (c.f. section 4.3).

The total DM for any given FRB is assumed to arise from a component due to the IGM, a component due to the ISM in a putative host galaxy and immediate vicinity of the source and a component due to the ISM of the Milky Way as given by Equation 1.15. These different DM components are modeled as follows:

1. the DM due to the IGM is assumed to be related to the redshift of the source via the simple scaling relation $\mathrm{DM_{IGM}} = 1200z\,\mathrm{pc\,cm^{-3}}$ (see Equation 1.16) with a 1σ scatter of order $\sim 20\%$ over the redshift range and DM range of interest (DM$> 100\,\mathrm{pc\,cm^{-3}}$, $0.5 \lesssim z \lesssim 2$) (Ioka, 2003; Inoue, 2004).

2. The contribution due to the ISM of the Milky Way along the line of sight to each event is taken from the NE2001 model of Cordes & Lazio (2002) which includes the electron density distributions in the thin disk, thick disk, spiral arms and Galactic Center components. For the high Galactic latitude regions simulated, this is generally, $\lesssim 50$ pc cm^{-3}.

3. The DM contribution of a putative host galaxy will depend on galaxy type, the FRB site within it and the viewing angle. Xu & Han (2015) have modeled the DM distributions due to the ISM for FRBs arising in elliptical, dwarf and spiral galaxies. They scale the NE2001 model of the Milky Way ISM to the integrated Hα intensity maps for such hosts, to represent their electron density distributions. The ensemble average DM distribution for dwarf galaxies is 45 $\mathrm{pc\,cm^{-3}}$ and for elliptical galaxies is 37 $\mathrm{pc\,cm^{-3}}$. For spirals, they derive the weighted average of the DM distribution over a range of inclination angles $(0°, 30°, 60°, 75°, 90°)$ to be 142 $\mathrm{pc\,cm^{-3}}$. Noting that there may be more than one type of FRB progenitor, Masui et al. (2015) conclude that their particular FRB could have occurred in a high density or star forming region of a host galaxy due to its high linear polarisation.

   Observationally, the galaxy stellar mass function distribution peaks near the Milky Way mass (Robles et al., 2008) (their Figure 9), and we assume the DM properties of the Milky Way are typical of a host FRB galaxy. Probing many random lines of sight through the NE2001 model, we derive a median DM of ~ 70 $\mathrm{pc\,cm^{-3}}$ for the Milky Way. Given the wide range of DM estimates above, and the uncertainty even as to what typical host galaxies are and the sites of FRBs within them, we have decided to follow Thornton et al. (2013) and Xu & Han (2015), and assume a DM value of $\mathrm{DM_{host}} \sim 100\,\mathrm{pc\,cm^{-3}}$ as typical over a range of hosts and inclination

angles. This assumption is somewhat *ad hoc*, but does have the advantage of facilitating comparison with previous work. Also, for the large DMs of the FRBs being analysed, this assumption has only a small effect. The assumed DM of the host is a small fraction of the total DM to FRBs both in our observed samples and in the simulations, and we could vary this host galaxy DM over the full range discussed above ($40 \lesssim \mathrm{DM} \lesssim 140$) and not affect the conclusions of the paper.

In the simulation, events are generated out to a redshift $z = 3.0$ in redshift shells of width $dz = 0.01$, each populated in proportion to the comoving volume of the shell and weighted by the star formation rate (SFR) at its redshift z (in "SFH" type models). Events are distributed randomly over the sky surveyed by Hilat in proportion to the total time spent on sky (i.e. the product of the number of pointings and the integration time per pointing). No events are generated north of declination $\delta = +10°$, the Northern limit of the survey performed at Parkes.

The fluence $\mathcal{F}$ (in Jy ms) at the telescope is derived from the energy at the source E, the luminosity distance in the ΛCDM cosmology and a factor of $(1 + z)$ representing the redshifting of the observed frequency range, given by:

$$\mathcal{F} = \frac{10^{29}\, E}{4\pi {D_L}^2(z)\, \Delta\nu\, (1+z)^{-1}} \ \mathrm{Jy\,ms} \tag{4.1}$$

where z is the redshift; $D_L(z)$ is the luminosity distance in pc; E is isotropic emitted energy in J; $\Delta\nu$ is the bandwidth of the receiver system in Hz. The S/N of each event is determined using the radiometer equation,

$$\mathrm{S/N} = \beta\, \frac{S\, G\, \sqrt{\Delta\nu\, t\, n_\mathrm{p}}}{T_\mathrm{rec} + T_\mathrm{sky}}, \tag{4.2}$$

where S is the flux of the signal in Jy, β is the digitisation factor $\simeq 1.0$, $\Delta\nu$ is the bandwidth in Hz, n_p is the number of polarisations, t is the pulse width in seconds, T_rec and T_sky are the receiver and sky temperatures in K respectively, and G is the system gain in K Jy^{-1}. Additional simulations of the FRB rates in other surveys are made later in the paper, and the parameters adopted in those simulations are shown in Table 6.1.

The brightest FRB in Thornton et al. (2013), namely FRB110220 was detected with S/N of ~ 50 and has an estimated energy $E = 10^{32.5}$ J at source, a pulse width of $t = 5.6$ ms, redshift of $z = 0.81$ and a luminosity distance of $D_L(z) = 5.1$ Gpc. Thornton et al. (2013) assumed the FRBs were radiating into 1 steradian (that is with a beaming fraction

[2] http://sourceforge.net/projects/heimdall-astro/

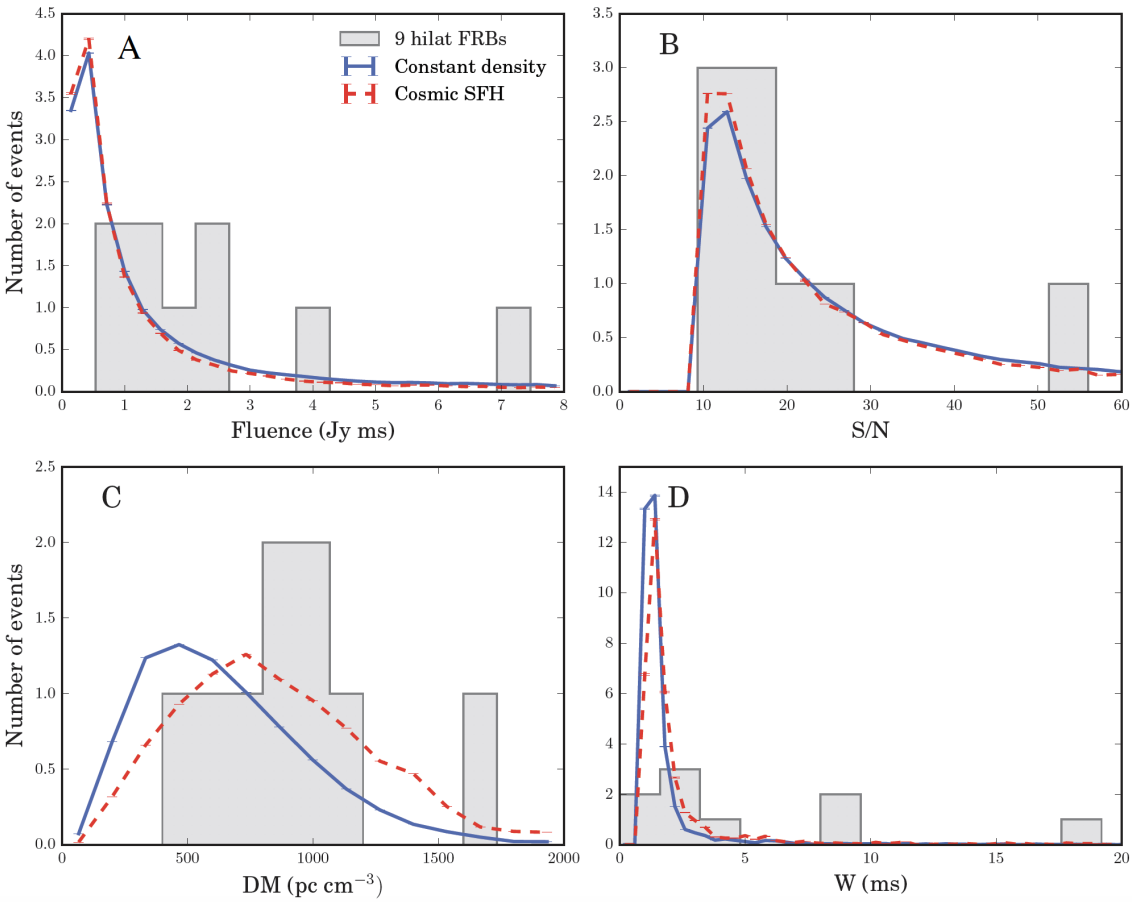

Figure 4.1 Simulated and observed distributions of fluence, S/N, DM and width for the 9 Parkes events. The dashed and solid curves represent the cosmic SFH and constant comoving density respectively. The 9 observed FRB events are represented by the histograms. The values of the data have been obtained using the HEIMDALL[2] single pulse detection software package. **Panel A**: Fluence distribution predicted by both models. **Panel B**: S/N distribution above the detection threshold of the FRBs. **Panel C**: FRB distribution as a function of total DM. **Panel D**: The observed widths distribution predicted by both models. We note that we are able to fit for all the observed properties, the pulse widths notwithstanding.

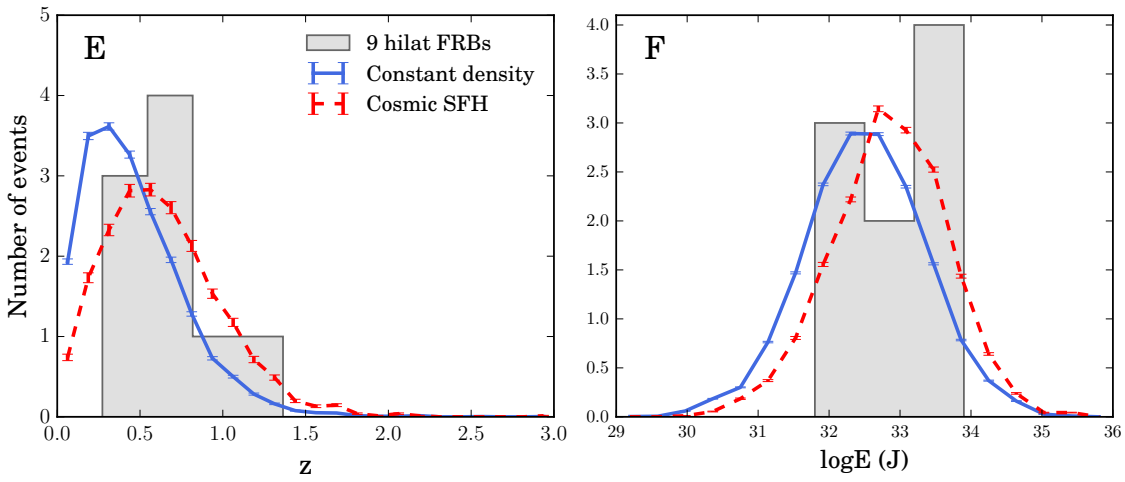

Figure 4.2 Derived FRB parameters from the Monte Carlo simulations of FRBs detected in the Hilat survey at Parkes. The dashed and solid curves represent the cosmic SFH and constant comoving density models for the FRB spatial densities respectively. The 9 observed Parkes FRB events are represented by the histograms. **Panel E**: FRB distribution as a function of redshift. **Panel F**: Unbeamed energy distribution of the FRBs.

of $1/4\pi$), whereas we assume isotropic radiation instead for simplicity. Accounting for this factor means that the isotropic energy of FRB110220 in the rest-frame is $E = 10^{33.6}$ J and its fluence is 7.3 Jy ms.

4.2.1 Scattering

Along the path from source to receiver, a radio pulse may be broadened in several ways. We assume the scatter-broadening time (τ) of a pulsed signal passing through the ISM is related to the DM by the empirical function derived by Bhat et al. (2004) in Equation 1.27.

Rescaling the scatter-broadening time through the ISM for the IGM, Lorimer et al. (2013) arrived at an upper limit to the average amount of scattering as a function of DM, with the scattering due to the IGM being 3 orders of magnitude smaller than that due to the ISM, i.e.

$$\log(\tau_{\rm IGM}) = \log(\tau_{\rm ISM}) - 3.0. \tag{4.3}$$

This rescaling on scattering in the IGM is still consistent with the observed widths of the majority of the FRBs discovered to date (Lorimer et al., 2013).

Additionally, the pulse is broadened or smeared across frequency channels because of the adopted frequency resolution $\tau_{\rm DM} = 8.3\,\Delta\nu\,{\rm DM}\,\nu^{-3}\,(\mu\,{\rm s})$ where DM is in $\rm pc\,cm^{-3}$, $\Delta\nu$ is the channel bandwidth in MHz and ν is in GHz. The observed width W of the FRB taking into account the different contributing components is:

$$W^2 = \tau_{\rm IGM}^2 + \tau_{\rm ISM}^2 + \tau_{\rm int}^2 + \tau_{\rm DM}^2 + \tau_{\delta\rm DM}^2 + \tau_{\rm samp}^2 + \tau_{\delta\nu}^2, \tag{4.4}$$

where the first two components are the scattering times due to the IGM and ISM, $\tau_{\rm int}$ is the (unknown) intrinsic width of the pulse, $\tau_{\rm DM}$ is due to the DM smearing, $\tau_{\delta\rm DM}$ is the second order correction to the DM smearing, $\tau_{\rm samp}$ is due to the adopted sampling time and $\tau_{\delta\nu}$ is the filter response of an individual frequency channel (Cordes & McLaughlin, 2003). The $\tau_{\delta\rm DM}$ and $\tau_{\delta\nu}$ terms are typically negligible in the context of our modelling. For the FRBs discovered at Parkes to date, $\tau_{\rm IGM}$ ranges from ~ 2 µs to ~ 40 ms and $\tau_{\rm ISM}$ ranges from ~ 40 ns to ~ 10 ms. Previous studies dealing with FRB detectability have assumed either a "no scattering" scenario or a strong ISM-like scattering scenario for the IGM, as its properties are highly uncertain. Macquart & Koay (2013) have suggested that if the latter scenario was true, the FRB pulses will be rendered undetectable at current telescopes, concluding that the IGM scattering was likely weak ($\leqslant 1$ ms). We may therefore be sampling a highly-selected population of FRBs, both in terms of luminosity and scattering.

The total width of a simulated event W affects its S/N ratio, scaling it down by a factor proportional to $\sqrt{W}$. This essentially limits the horizon of the HTRU survey to $z \sim 2$ as dispersive effects beyond this redshift rapidly degrade the S/N of even the brightest events to well below the adopted threshold of 10. Consequently, we use $z = 3.0$ as the high redshift cut-off in the simulations. This is sufficiently far to sample the dispersion measure space of the known FRBs.

4.2.2 Measured signal-to-noise ratios

The sky temperature additionally degrades the S/N particularly for sources close to the Galactic plane. We adopt a receiver temperature[3] of $T_{\rm rec} = 21$ K at Parkes and estimate the sky temperature ($T_{\rm sky}$) at the Galactic longitude and latitude (l, b) of the source from Haslam et al. (1982) who mapped the sky temperature at 408 MHz with a resolution of $0.85^\circ \times 0.85^\circ$. We scaled the survey frequency of 408 MHz to the HTRU frequency of 1.4 GHz by adopting a spectral index of -2.6 for the Galactic emission (Reich & Reich, 1988),

[3] www.parkes.atnf.csiro.au/observing/documentation/user_guide

i.e.,

$$T_{\rm sky} = T_{\rm sky_{(l,b)}} \left(\frac{\nu}{408.0\,{\rm MHz}} \right)^{-2.6}. \tag{4.5}$$

The S/N of each FRB event is then reduced by the additional factor $T_{\rm rec}/(T_{\rm rec}+T_{\rm sky})$. For most sources this is a negligible correction, becoming important only near the Galactic centre and low in the Galactic plane. $T_{\rm sky}$ at high latitudes is typically $\sim$ 1 K and lies between 3 and 30 K over the intermediate latitude regions. The S/N is finally degraded depending on a randomly chosen position in the beam pattern shown in Figures 4.3 and 4.4. For Parkes, each beam of the multibeam receiver is represented as an Airy disk with a 14.4 arc-minute full-width half-maximum. It should be noted that the effect of the beam pattern is quite significant on the distribution of both the event S/N and the apparent luminosity; this is discussed in detail in Section 4.3.3.

4.3 Analysis and Results

We have simulated FRBs in two models for their comoving number density (either following the SFH, or simply constant density) and either including or excluding the effects of scattering due to the IGM. In each model, we adopt a log-normal source luminosity distribution, centered on a mean energy E_0 and spread $\sigma_{\rm logE}$. The average energy of the 4 Thornton et al. (2013) events in Keane & Petroff (2015) correcting for the beaming fraction is $10^{32.8}$ J. We initially adopt $\log E_0 = 32.8$ and a spread of $\sigma_{\rm logE} = 1.0$, as this is the order of magnitude scatter seen on the Thornton et al. (2013) events. Within a given model choice for the source density with redshift, E_0 and $\sigma_{\rm logE}$ are the 2 free parameters.

The simulations were run on 12 CPU cores with runtimes of a few days on the gSTAR national facility at the Swinburne University of Technology. Millions of FRBs are typically generated in the runs, the vast majority of which are much too dim to see. We ran the simulations until we had $\sim$5000 FRBs that passed the selection criteria, to ensure good statistical sampling. The distributed properties of these FRBs are normalized and compared to the 9 observed Hilat events.

Slightly different selection criteria have been used by various authors to find FRBs. Thornton et al. (2013) used S/N $>$ 9 and DM $>$ 100 pc cm^{-3} and Champion et al. (2016) use the same selection criteria as Petroff et al. (2014), notably S/N $\geqslant$ 10, DM $\geqslant 0.9 \times$ DM$_{\rm MW}$ and $W \leqslant$ 16.3 ms. We use the criteria S/N $\geqslant$ 10 and $W \leqslant$ 32.786 ms for the selection of the candidates in the simulations. We adopt an upper limit of 32.786 ms for

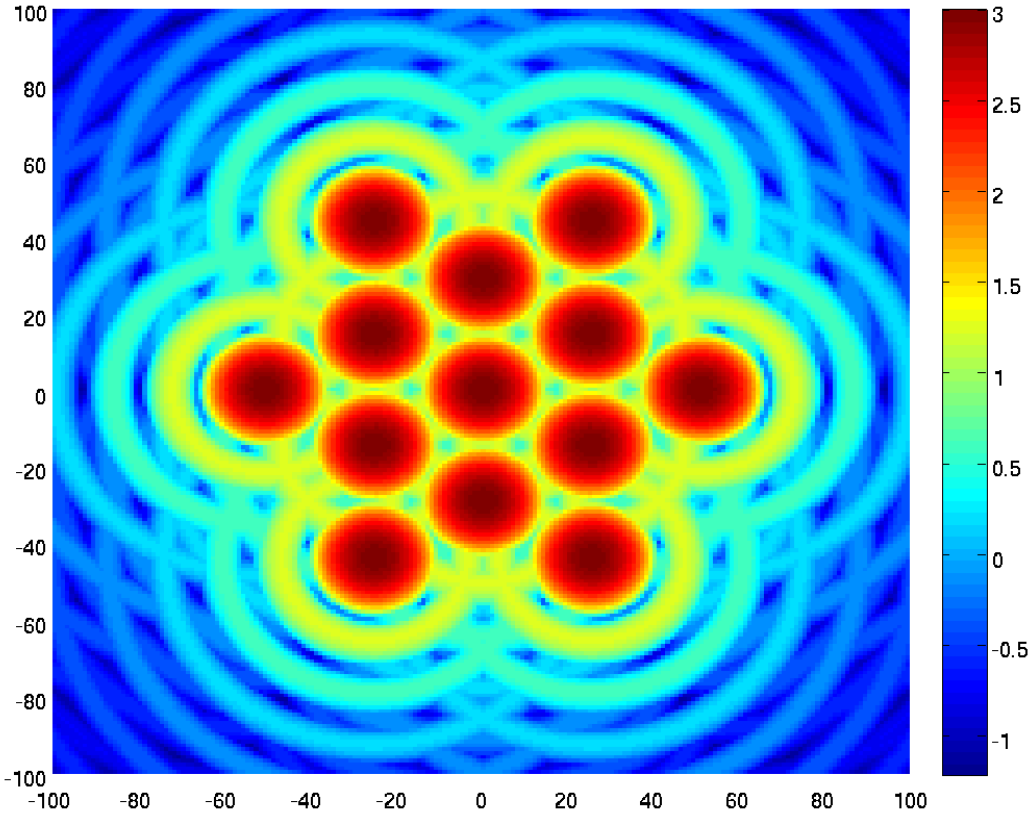

Figure 4.3 Simulation of the Parkes multibeam pattern shown in logscale where the colour represents the sensitivity at that point. Each of the 13 beams is modeled as a 14.4′ FWHM Airy disk pattern. All beams have been assumed to have the same gain and ellipticity as the central one.

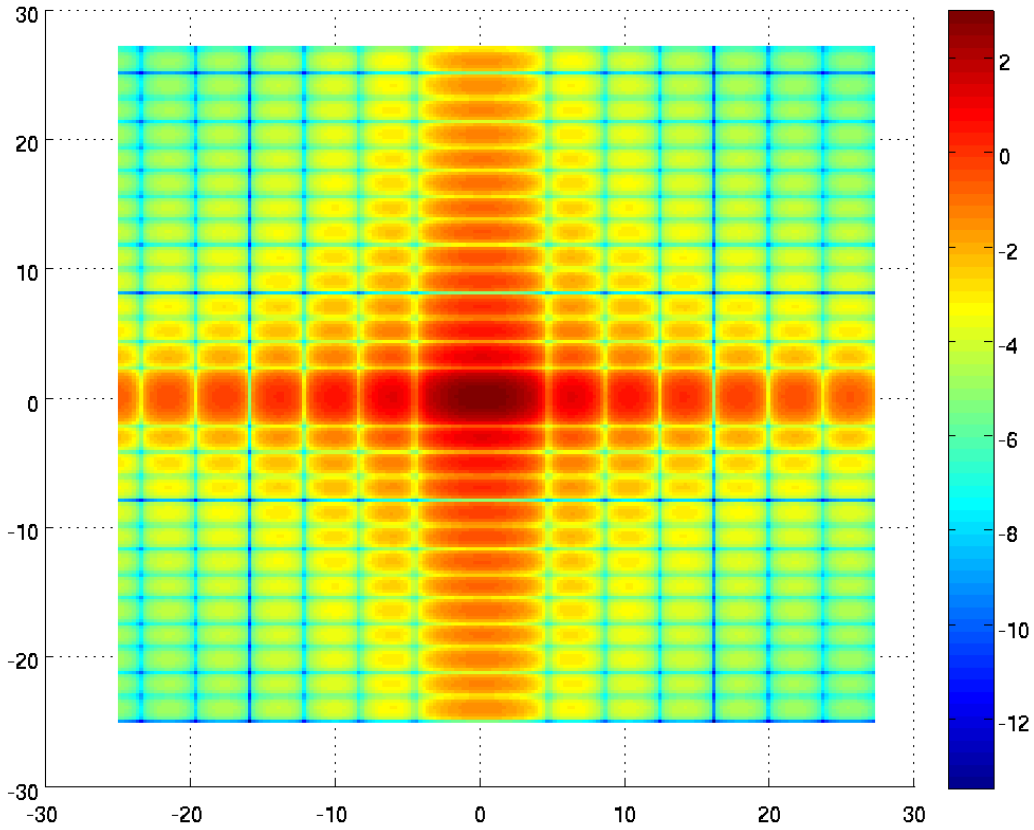

Figure 4.4 Simulation of the primary beam of the UTMOST telescope shown in logscale where the colour represents the sensitivity at that point. The primary beam is modeled as a $4.64^\circ \times 2.14^\circ$ 2-D Airy disk. It should be noted that the fan-beams described in Section 2.1 have not been simulated.

the width motivated by the fact that the broadest FRB discovered in Hilat has a width of ∼19 ms, and in any case broader events still would have to be intrinsically luminous (i.e. tail-end of the luminosity function and extremely rare) to have S/N > 10. We do not apply a DM threshold for the Hilat region as we are only sensitive to DM > 100 pc cm^{-3} in keeping with Thornton et al. (2013), due to assuming the value of $\mathrm{DM_{host}}$ to be 100 pc cm^{-3}. Tests showed that the differences in these selection criteria are minor and have negligible effect on our basic results.

4.3.1 Monte Carlo results for Parkes

Figures 4.1 and 4.2 display the results of the simulations of the cosmic SFH ($\rho_{\mathrm{FRB}}(z) = \rho_{\mathrm{SFH}}(z)$) and constant-density ($\rho_{\mathrm{FRB}}(z) =$ constant) models with scattering included, as seen by Parkes, overlaid on histograms of the 9 observed Hilat FRBs (Thornton et al. 2013; Champion et al. 2016). Figure 4.1 shows observational parameters for each burst and Figure 4.2 displays the parameters that are derived. We quantify the goodness of fit of the model to the observations in Section 4.3.2.

The fluence distribution of our simulated events is displayed in Panel A of Figure 4.1 and their S/N distribution in Panel B, each compared to the 9 Hilat events. All the observed Hilat FRBs have fluences between 0.7 and 7 Jy ms. Both models peak at ∼ 0.5 Jy ms and are reasonable matches to the observations. The S/N distributions of both models contain a large number of events just above the detection threshold of 10 and then gradually decline towards higher values; both appear to agree with the observations reasonably. Panel C shows the DM distribution of the models and the observations: this is similar to the panel showing the redshift distribution, since they are closely related. Both the cosmic SFH and constant density models are in agreement with the observed data.

The width of an FRB pulse affects its detection S/N. In the observer's rest frame, the width results from the sum of contributions from scattering due to the ISM and IGM (Equations 1.27 and 4.3, see Bhat et al., 2004; Lorimer et al., 2013) DM smearing time and the intrinsic width. Panel D of Figure 4.1 displays the distributions of the observed widths of the sources. We found neither model to agree with the data very well and this may be a result of our simplistic model of intergalactic scattering discussed below. The adopted model for the spatial density of the sources in Figure 4.2 Panel E does not have much effect on their redshift distribution, with only a small excess of sources produced at $0 < z < 0.5$ for the constant density model compared to the cosmic SFH model. As expected, we see a tendency for more events at higher redshift for the SFH model compared to the constant density model. Panel F shows the energy distribution (at source and in-band) of the FRBs

and the models. Both models are only sensitive to the bright tail of the adopted log-normal energy distribution function and have similar mean values to that of the 9 observed FRBs. Since the mean energy E_0 of the adopted luminosity function is a free parameter we adjust this to achieve good fits to the observed luminosities in panel F of Figure 4.1. Acceptable fits are obtained for both models by adopting $E_0 = 10^{31.2}$ J, with a log normal-scatter of $\sigma_{\rm logE} = 1.0$. This adopted luminosity function is a parameterised luminosity function only and possesses negligible physical significance.

4.3.2 Statistical analysis

Kolmogorov-Smirnov tests (K-S) were performed on all the distributions in Figures 4.1 and 4.2 and the resulting probability statistics p are given in Table 4.1. A p-value of < 0.05 is our criterion for deciding if the two distributions differ. Each model was compared against the data for the 9 FRBs.

The p-values show that both space density models of FRBs are consistent with the observed distributions of redshift, energy, fluence S/N and DM but, as already noted above, we have difficulty modelling the effect of scattering on the FRBs. The p-values of 0.013 (density of FRBs proportional to the cosmic SFH with redshift) and 0.001 (density of FRBs constant with redshift) reject the hypotheses that both models and the FRB data are from the same population. The present sample of 9 events is thus insufficient to distinguish between these models per se (the poor match to the distribution of pulse widths in both models notwithstanding). For FRBs discovered at Parkes, our simulations indicate that of order 50 FRBs are required to distinguish between the two FRB number density models at the 95% confidence level. This certainly highlights the need to discover FRBs more efficiently, as the present discovery rate is only of order 1 per 12 days on sky at Parkes.

To better understand the effective widths, the 14 FRBs at Parkes as a function of scattering time is shown in Figure 4.5. The estimated widths of the events due to IGM scattering and a possible intrinsic width ($\tau^2_{\rm IGM} + \tau^2_{\rm int} = W^2 - \tau^2_{\rm DM} - \tau^2_{\rm ISM}$ from Equation 4.4) are plotted against our estimate of the contribution to the total DM due to the IGM alone ($\rm DM_{IGM} = DM_{tot} - DM_{ISM} - DM_{host}$ from Equation 1.15). We see that the scattering times are inconsistent with Equation 4.3, and show considerable scatter around it.

This result highlights the basic difficulty with the IGM model, apparent in the data (Figure 4.5), that the pulse widths of the observed FRBs scatter around the adopted functional form for the IGM (Equation 4.3). This behaviour is also seen for pulsars being scattered by the ISM, for which there is at least an order of magnitude scatter in the

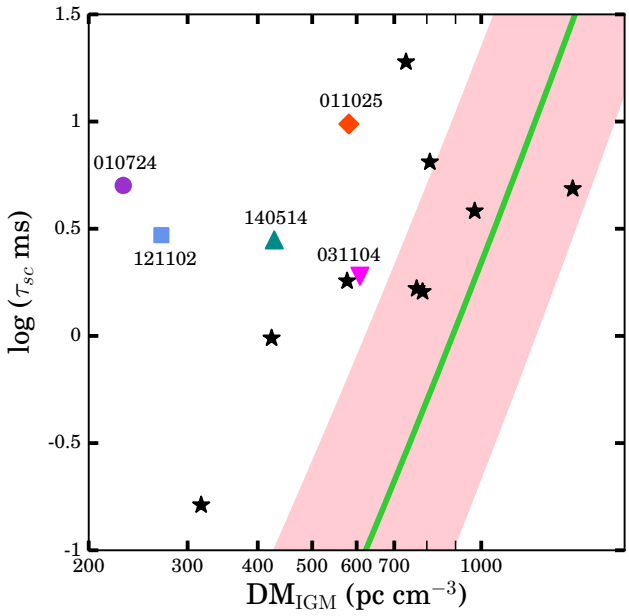

Figure 4.5 Adopted model of the scattering time due to the IGM (solid) at 1.4 GHz for Parkes versus estimated dispersion measures. Stars represent the 9 Hilat events and other markers represent FRBs discovered in various other surveys. It should be noted that some of the plotted values as upper limits as not all FRBs have scattering measurements. The shaded region around the fitted line to the equation represents the order of magnitude scatter adopted in the simulation. Note that one Hilat FRB lies below the IGM scattering relation (see Equation 4.3) but is still within the adopted 1-sigma spread.

Table 4.1 K-S test results for the adopted space density models against data (see Figures 4.1 and 4.2)

Parameter	p-value	
	Cosmic SFH	Constant density
Redshift	0.543	0.048
Energy	0.884	0.186
Fluence	0.047	0.106
S/N	0.258	0.078
DM	0.730	0.053
Effective width	0.013	0.001

data around the observed pulse width trend (Equation 1.27, see Bhat et al., 2004). If we assume that there is a similar scatter around $\tau_{\rm IGM}$ of an order of magnitude, we still do not acquire satisfactory fits to the data within 2σ confidence. This suggests that the scattering is not due to a LOS dependent inhomogeneous IGM. It may be due to interaction with the ISM of an intervening galaxy or an intracluster medium along the LOS, although the probability of intersection at the redshifts modelled is quite low and only a small fraction of lines of sight may be affected (Macquart & Koay, 2013). We have not attempted to model such effects: our aim is to test a much simpler model before adding in difficult to test assumptions about the properties of the IGM. If we assume that our simulated events have a mean intrinsic width of 3 ms based on the fact that the data distribution peaks at $\sim$ 3 ms (with a standard deviation of 3 ms, truncated at 0 ms), the resulting width distributions are found to be in good agreement with the observed 9 hilat FRBs. The intrinsic width assumption is motivated by FRB121002 and FRB130729 (Champion et al., 2016) which have hints of double, rather than single peaked pulse profiles. This is a rather *ad hoc* assumption and further work on this is required once the population is expanded (hence our work at UTMOST, Chapters 5 and 6). The disagreement of the distribution of event widths with the observations is the weakest point in our modelling. Clearly, there is a need for more FRBs to resolve this problem.

4.3.3 The log$N$-log$\mathcal{F}$ of the Hilat events

In a Euclidean Universe populated with events (or objects) of fixed luminosity (i.e. standard candles) and uniform number density, the number N detected above some flux limit S varies as $N \propto S^{\alpha}$, where $\alpha = -3/2$. In our model, the FRBs have a very broad luminosity distribution and are sufficiently distant (few Gpc) that non-Euclidean effects are important. Consequently we do not expect to see $\alpha = -3/2$.

The very wide range of luminosities of the observed events suggests they are not particularly good standard candles and/or that they are strongly beamed, and until we have a redshift of an FRB host galaxy, or some other independent distance indicator for an FRB, their luminosities are highly dependent on the assumption that DM is a proxy for redshift. The luminosities are dependent on each LOS being equal to the average LOS in a ΛCDM Universe. In fact it is the small deviations from this that we will use to do cosmology and FRB progenitor physics, when we have a lot of FRBs with real redshifts. In any case, our FRB simulations are for a ΛCDM cosmology, which affects α. In a ΛCDM cosmology, α varies smoothly from a slope of $-3/2$ for the nearby Universe, gradually becoming flatter as further distances are probed. To illustrate, at a redshift of

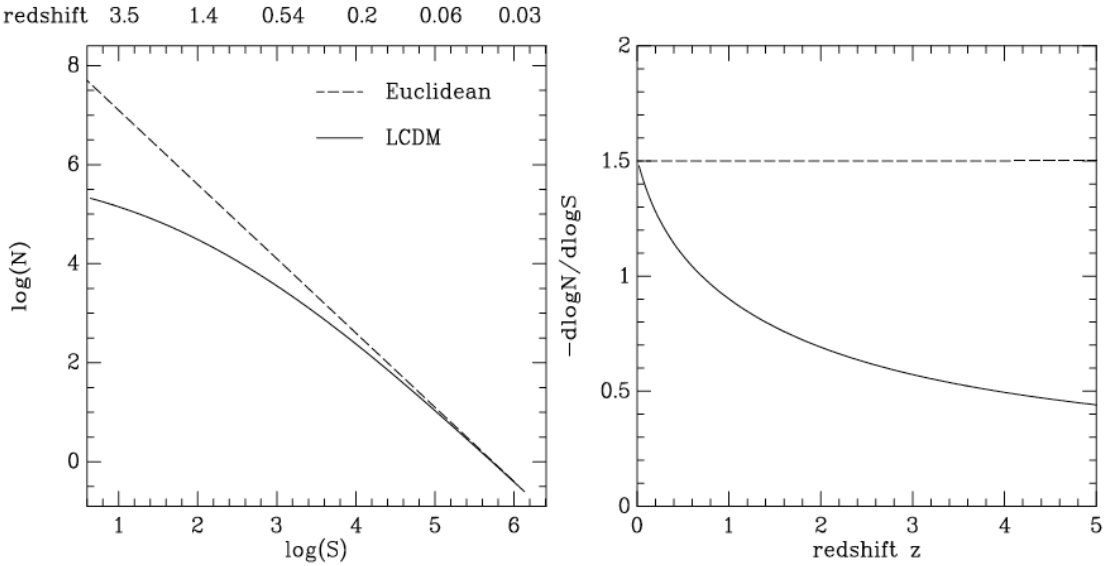

Figure 4.6 Left: The log$N$-log$S$ relations for a Euclidean and ΛCDM cosmological models (S and N are in arbitrary units). The redshifts in the ΛCDM model are indicated at the top. Right: Slope of the log$N$-log$S$ relation in ΛCDM shown as a function of redshift z. Image credit: Chris Flynn.

$z \sim 0.7$, typical of FRBs found to date, standard candles yield a relation with a slope of $\alpha \sim -1$ as we see observationally. There are additional factors which affect α. Firstly, the HTRU survey is "fluence incomplete" in the sense that events with the same fluence are easier to detect if they have narrower pulse widths. Secondly, propagation of FRB pulses through the IGM causes the pulses to broaden, reducing their S/N, so that a S/N selected sample effectively has a distance horizon beyond which pulses are too scattered to see. This will flatten the relation as we probe to dimmer events.

It is possible to select a "fluence complete" sample of the FRBs (Keane & Petroff, 2015), and compare these to simulation events selected in the same way, but this would reduce our sample of 9 events to just 4 events. For a S/N of 10, the fluence completeness limit for Hilat is ~ 2 Jy ms (Keane & Petroff, 2015). This is an observational selection, and marginally affects the slope α, of the relation. It is straightforward to include this effect in the simulations, however, due to our already small sample of events we prefer to compare to the full correctly modelled fluence incomplete set of 9 events, selected by S/N, rather than a fluence complete set of 4 events.

The log$N$-log$\mathcal{F}$ plot of the 9 Hilat events is shown in Figure 4.7 — note that we use the fluence $\mathcal{F}$ in Jy ms (since FRB detections are width dependent) for what would normally be flux density S in Jy. The cumulative log$N$-log$\mathcal{F}$ relation is reasonably linear for the

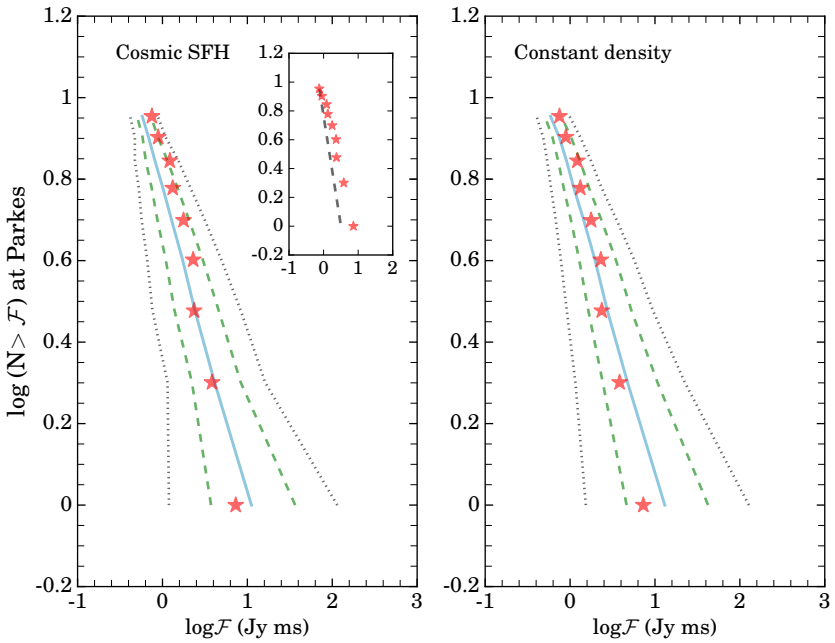

Figure 4.7 The log$N$-log$\mathcal{F}$ curves for the 9 Hilat FRBs and the simulation samples. The left panel displays the cosmic SFH (Hopkins & Beacom, 2006) scenario and the right panel displays the constant comoving space density scenario for the FRBs. Stars represent the 9 Hilat FRBs and the solid line connects the medians of the number densities as a function of fluence for the simulation sample. The dashed and dotted lines represents the 1σ and 2σ limits around the median for each N. The inset in the left panel exhibits the 9 observed FRBs and a fitted slope of $\alpha = -3/2$ for comparison.

9 events, and has a slope of $\alpha = -0.9 \pm 0.3$. For the cumulative curve of only 9 events, sample variance dominates the error. We use the simulations of Hilat (as described in section 4.2 with selection criteria described in Section 4.3), which were set up to yield of order 9 events per run to estimate the error on α. Those realisations which had exactly 9 events were used for comparison with the 9 observed Hilat events. We have fitted slopes (α) to these simulated 9 event samples and show the distribution of α in Figure 4.8. The typical error on determining α is ± 0.1 for a single run, which is the adopted bin size in Figure 4.8. The median slope obtained is $\alpha = -0.8$ for the SFH case and $\alpha = -0.7$ for the constant FRB space density model, but with significant scatters (the 1 σ limits are shown as dashed lines) of order ± 0.3 for the SFH and ± 0.2 for the constant density around the mean. Our observed slope of $\alpha = -0.9 \pm 0.3$ is consistent with both models, where the error is the scatter caused by our sample size.

We conclude that the slope of the log$N$-log$\mathcal{F}$ relation of the 9 observed events is consistent to within the uncertainties of both the simulated models, indicating that our

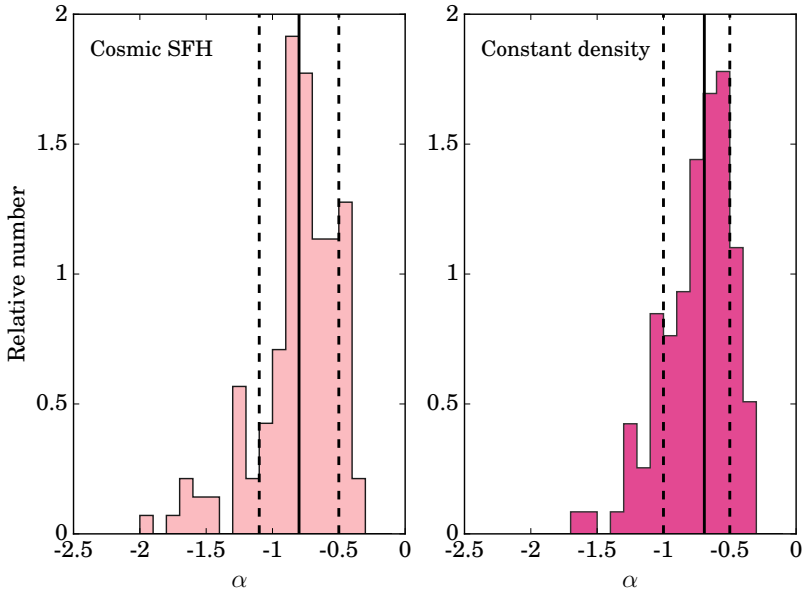

Figure 4.8 The histograms display the slopes α, of the simulation samples containing exactly 9 events each. The left panel represents the cosmic star formation history scenario and the right panel represents the constant comoving density scenario. The medians of the histograms are represented by the solid lines and the 1σ scatter from the median is marked by the dashed lines. The slope of the log$N$-log$\mathcal{F}$ relation for the 9 FRBs in Hilat $\alpha = -0.9 \pm 0.3$ is found to be consistent with the simulations within the uncertainties.

measured log$N$-log$\mathcal{F}$ slope is consistent with FRBs being of cosmological origin. This is in agreement with the conclusion of Katz (2016) that the log$N$-log$S$ and N vs. DM distributions are consistent (except for the anomalously bright Lorimer burst) with cosmological distances inferred from their DM in a simple approximation to standard cosmology.

4.3.4 Medlat vs Hilat

The intermediate-latitude component of the HTRU survey consists of 540-sec pointings in the range $-120° < l < 30°$ and $|b| < 15°$. Petroff et al. (2014) found no FRBs in this region of the survey. Under the assumption that FRBs are isotropically distributed, scaling from Hilat, and accounting for a slight reduction in their detectable source density in the Medlat region due to the smearing effects of the ISM, they estimate the probability of this occurring by chance as only of order 0.5%. We simulate both the Medlat and Hilat regions (adopting 100% of Hilat and 100% of Medlat as the surveyed completeness for the regions for FRBs) to determine the likelihood of finding zero FRBs in Medlat for 9 discovered FRBs in Hilat. The simulation for Medlat is otherwise identical to the one

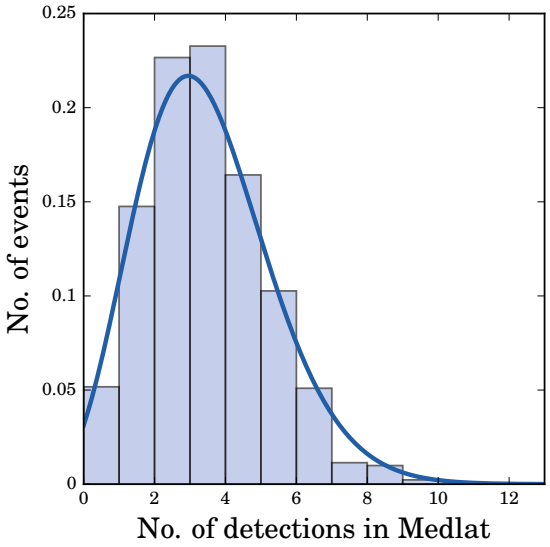

Figure 4.9 Number of FRBs expected in the Medlat sub-survey normalized to the 9 events in the Hilat sub-survey. Both surveys are assumed to be fully searched for FRBs. The histogram represents the number of FRBs expected in Medlat for a corresponding 9 FRBs detected in Hilat. A Poissonian curve is fitted to the data. The number of FRBs found in Medlat is zero 5.1% of the time which supports a Galactic latitude dependence.

described in Section 4.2 except for the survey parameters i.e. number of pointings, region of sky surveyed, $T_{\rm sky}$ corresponding to the region of sky surveyed and integration time per pointing. The same selection criteria as described in Section 4.3 are used for selection of candidates in both Medlat and Hilat. We obtain an average of $\sim 3 \pm 2$ events in our Medlat simulations for every 9 events in the Hilat simulations, finding no events just 5.1% of the time (Figure 4.9) thereby supporting a Galactic latitude dependence. The estimated probability of zero events being seen in Medlat 0.5% of the time made by Petroff et al. (2014) is based on the 4 events detected in the 24% of the Hilat survey which had been searched at the time. The higher probability we estimate of finding no events in Medlat in our simulations is due to our using the lower all sky rate, now that Hilat has been completely searched and it only yielded 9 FRBs.

4.4 The log$N$-log$\mathcal{F}$ of FRB events at other facilities

Our simulations have been used to generate FRB events at 2 facilities – Parkes and UTMOST (Bailes et al. submitted). UTMOST is the recently upgraded Molonglo Observatory Synthesis Telescope located about 300 km south-west of Sydney, near Canberra, and is a field station of the University of Sydney. We generate events for the

Table 4.2 Specifications of Parkes multibeam, Parkes PAF and UTMOST as used in our simulations to make FRB rate predictions at each facility.

Parameter	Unit	Parkes MB (Keith et al., 2010)	Parkes PAF[a]	UTMOST (Bailes et al. submitted)
Field-of-View	deg^2	0.55	2.2	4.64×2.14
Central beam Gain	K Jy^{-1}	0.7	0.9	3.5
Central beam T_{sys}	K	21	50	70
Bandwidth	MHz	340	340	16
Frequency	MHz	1352	1352	843
Channel width	MHz	0.390625	$\sim$1	0.78125
No. of polarisations	–	2	2	1
Polarisation feeds	–	Dual linear	Dual linear	Right circular

[a]http://www.atnf.csiro.au/management/atuc/2013dec/science_meeting/ATUC_PKS_receivers.pdf

Table 4.3 Minimum detectable flux density for a 10σ, 1 ms event and event rate assuming a Euclidean scaling for the Parkes multibeam, Parkes PAF and UTMOST.

Telescope/Receiver	$S_{\rm min}$ (Jy)	Rate (events day^{-1})
Parkes MB	0.4	0.08±0.03
Parkes PAF	0.6	0.10±0.04
UTMOST	1.6	0.16±0.06

specifications of UTMOST and Parkes for the soon to be installed phased array feed (PAF) receiver in comparison with the current multibeam receiver (MB) at Parkes. The FRB comoving density models, and energy distributions are the same as those described in Section 4.2. The effective pulse width of each event is computed using Equation 4.4. The S/N of the events were reduced by a factor of 4 for the events at UTMOST to account for the fact that it is less sensitive than the MB receiver at Parkes (see Caleb et al. (2016b) in Chapter 5). The Parkes PAF is estimated to have $\sim$ 50% of the sensitivity of the multibeam[4] which is accounted likewise. The S/Ns at both telescopes were further reduced by $\sqrt{W}$ before making the cut-off of S/N $\geqslant$ 10 and $W \leqslant 32.786$ ms.

Figure 4.10 shows the cumulative log$N$-log$\mathcal{F}$ curves at UTMOST and at Parkes for both the MB and phased array feed PAF. These curves do not include the effects of fluence completeness. All curves have been normalised to their respective FRB rates in Table 7.1, which have been calculated assuming a Euclidean Universe where the cumulative number density scales as $\propto \mathcal{F}^{\alpha}$ where $\alpha = -3/2$ (see Caleb et al. (2016b) in Chapter 5). This is a conservative option, as the slope of this relation is most likely flatter (as seen in the previous section), and underestimates the number of events expected. In Chapter 6 we see that the predicted rate at UTMOST at $\sim$ 14 percent sensitivity is underestimated by a factor of 3 from the measured rate, thereby supporting a flat log$N$-log$\mathcal{F}$ relation.

4.5 Discussion and Conclusions

We have simulated observational and derived properties of a cosmologically distributed population of FRBs, for comparison with the 9 FRBs seen in the HTRU/Hilat survey conducted at Parkes from 2008 - 2014. Two models for the spatial number density of the FRBs are examined: firstly, where the comoving density is a constant, and secondly, where the number of FRBs is proportional to the cosmic SFH. The properties of the ISM in the Milky Way and a putative host galaxy for the FRB are taken into account, and

[4]http://www.atnf.csiro.au/management/atuc/2013dec/ science_meeting/ATUC_PKS_receivers.pdf

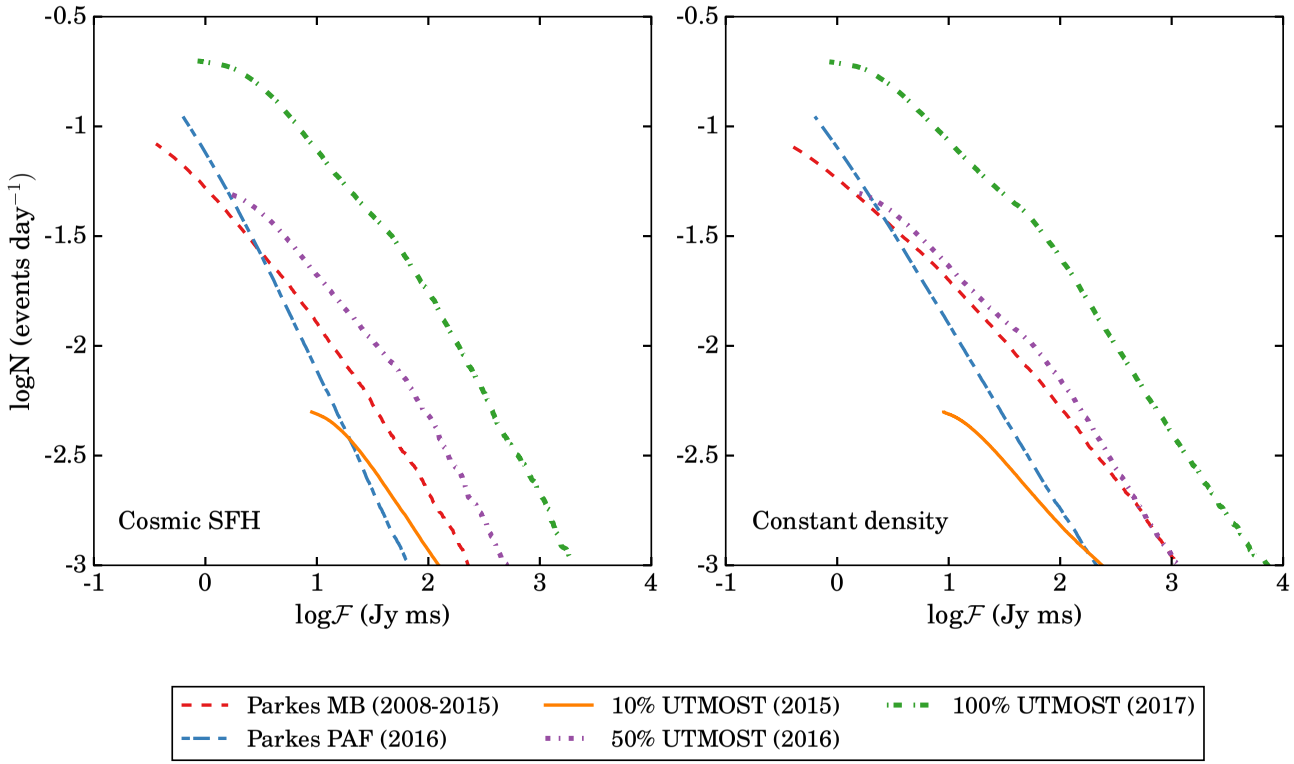

Figure 4.10 The log$N$-log$\mathcal{F}$ curves for different fractional sensitivities at UTMOST and MB and PAF receivers at Parkes. The left panel displays the log$N$-log$\mathcal{F}$ curves for the cosmic SFH (Hopkins & Beacom, 2006) model of the FRB space density with redshift and the right panel displays the curves for the constant density model. All curves include the ISM and IGM scattering and are normalised to the rate of ~ 1 event per 12 days at the Parkes MB and additionally to the ratio of their FOVs for UTMOST and the Parkes PAF. The measured rate at UTMOST is however 3 times higher than the one predicted here as discussed in Chapter 6. Uncertainty in the PAF design sensitivity makes prediction difficult, but its wider sky coverage can increase the Parkes discovery rate at lower fluences.

conservative assumptions are made about the properties of the IGM, the spectral index of FRBs and their luminosity function.

The simulated distributions of redshift, energy, DM, S/N, fluence and effective widths for both the cosmic SFH and constant density models were compared to the 9 observed FRBs. We achieved reasonable matches to the data for all these properties except the event widths, by adjusting only the typical FRB event energy at source (and scatter around this energy) i.e. by adjusting only their luminosity function. It proved difficult to fit the distribution of FRB widths without making *ad hoc* assumptions about scattering in the IGM or the intrinsic widths of the pulses. The simulations are intended to look at FRB properties with as simple an assumption set as possible; adding in poorly constrained properties as these for the FRBs and the IGM for the sake of fitting the pulse widths was not pursued. As the pulse widths probe completely different properties of FRBs and the IGM, this may prove more fruitful to understanding their origin as more FRBs are found.

The most interesting property of the simulated events is the distribution of log$N$-log$\mathcal{F}$, where N is the number of events detected above some fluence $\mathcal{F}$. If the sources have an even approximately "typical luminosity" (i.e. are standard candle-like) then the slope of this relation is a probe of their spatial distribution. For standard candles of flux S distributed uniformly in empty, Euclidean space, the slope of the closely related log$N$-log$S$ relation is well known to be exactly $-3/2$. For FRBs, the slope of the relation is affected substantially for 3 main factors: firstly by cosmology (space is non-Euclidean); secondly by propagation through the IGM (i.e. space is not empty) and thirdly by selection effects at the telescope (narrower events are detected more readily than broader ones). A major aim of the simulation is to quantify these effects.

The observed slope α of the log$N$-log$\mathcal{F}$ of the 9 FRBs analysed is $\alpha = -0.9 \pm 0.3$. Our simulations are able, in both scenarios for the number density of the sources with redshift, to match this slope well, yielding $\alpha = -0.8 \pm 0.3$ for the cosmic SFH and $\alpha = -0.7 \pm 0.2$ for the constant density case. We conclude that the properties of the observed FRBs are consistent with arising from sources at cosmological distances, with the important caveat that the pulse width distribution does not match our simulation results particularly well. The luminosity function of the FRBs is the main free parameter in the simulations. We adopt a log-normal luminosity function (LF) and adjust the mean energy E_0 and spread in energy $\sigma_{\log E}$. It is clear from the 9 observed events that a narrow, standard-candle like LF is an unacceptable fit, since their inferred intrinsic lumninosities has a spread of about an order of magnitude. We measure a mean energy E_0 of $\sim 10^{31.2}$ J with a spread of a factor of 10 in energy. As the observed FRBs very much sample only the high luminosity

tail of this distribution, other choices for the LF, such as a truncated power law would also adequately match the data. Our studies show that the beam pattern of the telescope has a strong effect only when the number of FRBs is large ($\gtrsim$ few $\times$ 100), which is then sensitive to the high luminosity tail of events. The LF choice affects the distributions strongly even for small samples : an LF with a significant spread in luminosity is required to model the 9 events. Finally, our simulations show that the adopted comoving density models for the FRBs has weak effects, and large sample sizes ($\gtrsim$ 100) are required to probe this. Future work could implement other LF choices and investigate the extent to which the LF and SFH and beam pattern affect the observed distributions analysed in this paper: the small number of FRBs detected to date do not warrant such work here.

Our simulations show that at least 50 FRB events are required to distinguish, at the 95% confidence level, between our two tested models for their cosmological spatial distributions for the specifications of the Parkes telescope. This argues strongly for projects to increase the detection rate of FRBs by using wide FOV instruments, such as UTMOST and CHIME (Bandura et al., 2014). Even more important in the immediate future is to localise events on the sky (to find putative host galaxies for FRBs as demonstrated by Chatterjee et al., 2017; Tendulkar et al., 2017; Marcote et al., 2017) and a number of experiments are ongoing to do this (eg: SUPERB project at Parkes). We have applied our simulations to the Medlat survey at Parkes (which is part of the HTRU survey), which surveyed a lower Galactic latitude region of the sky with longer integrations. Our simulations of this survey support the conclusion of Petroff et al. (2014) that the sky rate of FRBs in Thornton et al. (2013) is overestimated by about 50%, or that FRBs are not distributed isotropically on the sky. In case of the former, this latitude dependence of FRBs where they appear to favour high Galactic latitudes, could be explained by diffractive scintillation boosts at high latitudes (Macquart & Johnston, 2015). In case of the latter, it could mean that FRBs are indeed an extragalactic/cosmological population thus disproving Galactic progenitor theories (e.g. Flare stars; Loeb et al., 2014) in the process.

We simulate FRB rates at two other facilities: at UTMOST (first survey results of which are in the companion paper Caleb et al., 2016b) and at Parkes with the planned PAF, under conservative assumptions about the spectral index of FRBs, and the sensitivity of the instruments. UTMOST has the capability, at full design sensitivity to dominate the FRB detection rate. Uncertainty in the final PAF design sensitivity makes prediction difficult, but its wide sky coverage has the potential to increase the discovery rate of FRBs close to the fluence limit.

5

Fast transient searches with UTMOST at 843 MHz

This chapter (published as Caleb et al., 2016b) presents the upgrade to UTMOST and the initial FRB surveys performed with UTMOST at different fractional sensitivities as part of commissioning science. No FRBs were detected in 467 and 225 hours on sky at 7% and 14% sensitivity respectively. This non-detection was not unexpected, based on the sensitivity and time spent on sky, and places an upper limit on the detection rate at 843 MHz. Much of the work on event rate has been done at 1.4 GHz and this work is important to place constraints on the rates at lower frequencies and to determine the frequency at which the rate drops to zero.

5.1 Introduction

Only two dozen FRBs are known, and to date none have transient events or afterglows associated with them at other wavelengths despite major efforts to do so. Several cosmological and non-cosmological models for the origin of FRBs have been suggested, including radio emission from pulsars (Cordes & Wasserman, 2016; Connor et al., 2016b), collapsing gravitationally unstable supramassive neutron stars into black holes (Falcke & Rezzolla, 2014), hyper flares from magnetars (Lyubarsky, 2014) and dark matter induced collapse of neutron stars (Fuller & Ott, 2015).

In the previous chapter I describe Monte Carlo simulations of a cosmological population of FRBs to study the distributions of their observed and inferred properties and their log$N$-log$\mathcal{F}$ curve. From comparison of the slope of the log$N$-log$\mathcal{F}$ curves of the simulations with the slope of the log$N$-log$\mathcal{F}$ curve of the observations we conclude that FRBs are consistent with being of cosmological origin. If FRBs are indeed cosmological in origin, they could be potentially used to probe the 'missing baryon problem' (McQuinn, 2014), obtain rotation measures of the IGM along the LOS (Zheng et al., 2014) and also as an independent

measure of the dark energy equation of state (Zhou et al., 2014). Most of the FRBs that have been discovered to date i.e. between 2007 and 2015, have all been seen at 1.4 GHz using single dish antennas with relatively poor angular resolution. This means that their spatial localisation is poor and lacks the precision required to unequivocally associate them with possible host galaxies. Until 2013, FRBs had only been discovered in archival surveys, but since 2014 we have entered the era of real time detections with rapid multi-wavelength follow-up with a few already having been performed at Parkes (Petroff et al., 2015a; Keane et al., 2016; Petroff et al., 2017, Bhandari et al., submitted). Thornton et al. (2013) estimate the FRB event rate as $\mathcal{R}_{\rm FRB}(\mathcal{F} \sim 3\,{\rm Jy\,ms}) = 1.0^{+0.6}_{-0.5} \times 10^4 {\rm sky}^{-1}\ {\rm day}^{-1}$. Keane & Petroff (2015) have reanalyzed the Thornton et al. (2013) results and derive a fluence complete event rate of 2500 events ${\rm sky}^{-1}\ {\rm day}^{-1}$ above a fluence of 2 Jy ms.

There is clearly a need to discover FRBs more efficiently as the present discovery rate is only of order 1 per $\sim$ 12 days on sky at Parkes. The 50 year old Molonglo Observatory Synthesis Telescope in Australia is being refurbished (2014−2017) with a new digital backend system and increased bandwidth as part of an upgrade to transform it into a burst finding machine. This instrument being an interferometer will help discern if FRBs are truly a celestial population by placing a lower limit on the parallax to the sources. In this paper we introduce the Molonglo Observatory Synthesis Telescope and discuss its single pulse sensitivity in Section 5.2. The first FRB survey at 843 MHz using the UTMOST instrument and limits on the detectability of FRBs is discussed in Section 5.3. We make estimates of the FRB rates we can expect with the UTMOST instrument, showing that at full sensitivity it is considerably more effective than Parkes for doing FRB surveys due to its large FOV and high observing duty cycle (Section 5.4) under conservative assumptions for the FRB spectral index. At full sensitivity we expect to detect an event every few days. We constrain the FRB event rate and mean spectral index based on the non-detection of FRBs in these pilot surveys and draw our conclusions in Section 6.5.

5.2 The Molonglo Observatory Synthesis Telescope (MOST)

The Molonglo Observatory Synthesis Telescope (MOST) is being upgraded (2014−2017) both in the backend receivers and with the installation of a new graphics processing unit (GPU) based correlator, in a collaboration between Sydney and Swinburne Universities. See Chapter 2 for details on the telescope and the ongoing upgrade. The installation of high-performance GPUs at MOST has transformed it into a powerful instrument, the Swinburne University of Technology upgrade for the MOST (UTMOST ; Bailes et al., submitted). This has enlarged the FOV to twice that of the Sydney University Molonglo

Table 5.1 Comparison of Parkes multibeam (Manchester et al., 2001) and UTMOST (Bailes et al., submitted)

Parameter	Parkes	UTMOST
Field of View (deg^2)	0.55	4.64×2.14
Central beam Gain (K Jy^{-1})	0.7	3.6
Central beam $T_{\rm sys}$ (K)	21	70
Frequency (MHz)	1352	843
Bandwidth (MHz)	340	31.25
Channel width (kHz)	390.625	781.25
No. of polarisations	2	1
Polarisation feeds	Dual linear	Right circular
Fresnel limit (km)	~ 40	$\sim 14{,}000$

Sky Survey (SUMSS ; Bock et al., 1999) due to processing data from each 'module' rather than each 'bay'.

The sensitivity of UTMOST to FRB events (i.e. single pulse events) can be calculated using the radiometer equation,

$$S_{\rm min} = \beta \, \frac{\rm S/N \, (T_{rec} + T_{sky})}{G \sqrt{\Delta\nu \, t \, n_{\rm p}}} \tag{5.1}$$

where $S_{\rm min}$ is the minimum detectable flux for a given minimum signal-to-noise (S/N), β is the digitisation factor, $\Delta\nu$ is the bandwidth in Hz, $n_{\rm p}$ is the number of polarisations, t is the width in seconds, $T_{\rm rec}$ and $T_{\rm sky}$ are the receiver and sky temperatures in K respectively, and G is the system gain in K Jy^{-1}. For a pulse with S/N of 10 and width of 1 ms at Parkes, the sensitivity is $S_{\rm min} = 0.4$ Jy. At UTMOST, $S_{\rm min} = 1.6$ Jy. Thus UTMOST is about four times less sensitive to individual FRB events than Parkes. This is more than compensated for with its 14 times larger FOV indicating that UTMOST can be a very effective FRB discovery machine. In practice the sensitivity at UTMOST degrades depending on the scattering from the ISM and possibly the IGM at the lower UTMOST operating frequency. Detailed calculations of the event rate at UTMOST, taking into account the system sensitivity, sky temperature at our operating frequency, scattering effects due to the ISM and IGM, DM smearing due to channel bandwidth, beam pattern of the telescope and adopted FRB comoving space density are described in the previous chapter. The main properties of UTMOST and Parkes from the point of view of discovering FRBs are shown in Table 6.1.

5.3 FRB surveys at UTMOST

Two FRB searches have been performed at UTMOST at different fractional sensitivities during the ongoing upgrade. These two surveys are called V1.0 and V2.0. The antennas are aligned and fringe stopped to maintain stable and flat phases and then combined into a tied-array beam, centered on the primary beam boresight. This beam is then re-steered into 352 tied array beams called "fan beams" that are "tiled" across the 4 degree East-West axis of the primary beam. Time series from each fan beam are detected and integrated from 1.28 to 655.36 μs sampling and also requantised to 8-bits/sample.

The total data rate to the backend was 11 GBps, and the resulting output data rate from the 352 beams was approximately 10 MBps for both surveys. The input stream at UTMOST in FRB search mode is 16 MHz for survey V1.0 and 31.25 MHz for V2.0, of single polarisation baseband data from 352 antennas, in 20 frequency channels produced in a PFB. We upgraded to 40 coarse channels in FRB survey V2.0. After completion of V1.0, the rest of the GPUs were installed onsite (May 2015) so that the full 31.25 MHz could be processed for V2.0. As a consequence it is clear that roll-off at the edge of the bandpass is quite pronounced so that the extra bandwidth is not usable. We conservatively assume 16 MHz of final effective bandpass for all the results in this paper.

For both surveys the time-frequency data for each fan beam is initially dedispersed to trial DMs in the range 0 to 2000 $\mathrm{pc\,cm^{-3}}$. Each dedispersed time series is then convolved with a series of boxcar filters to maximise sensitivity to single pulses and optimised for processing on a GPU using HEIMDALL[1]. This package was originally designed for the program at the Parkes Observatory, and has been suitably modified to accommodate the specifications of UTMOST. HEIMDALL produces a list of candidates for each of the 352 fan beams, which are then carefully "coincidenced", by rejecting events if they occur simultaneously in more than 3 fan beams (of the 352). The output of the coincidencer is a final list of candidates for human inspection. The candidate list is then further filtered to only retain events which have S/N $\geqslant$ 10 (to reduce the false positive rate to manageable levels) and $W \leqslant 41.943$ ms ($W = 2^{\mathrm{N}} \times 0.65536$ ms, where N = 0,1,2...). For the purposes of labeling these as either RRAT, pulsar or FRB candidates we define all pulses with $W \leqslant 41.943$ ms and DM $\geqslant 100$ $\mathrm{pc\,cm^{-3}}$, as FRB candidates, the rest as RRAT/pulsar candidates.

A typical FRB search is made on the transiting sky, with the telescope being parked on the meridian at a declination of $\delta = -46°$. This declination has the advantage of

[1] http://sourceforge.net/projects/heimdall-astro/

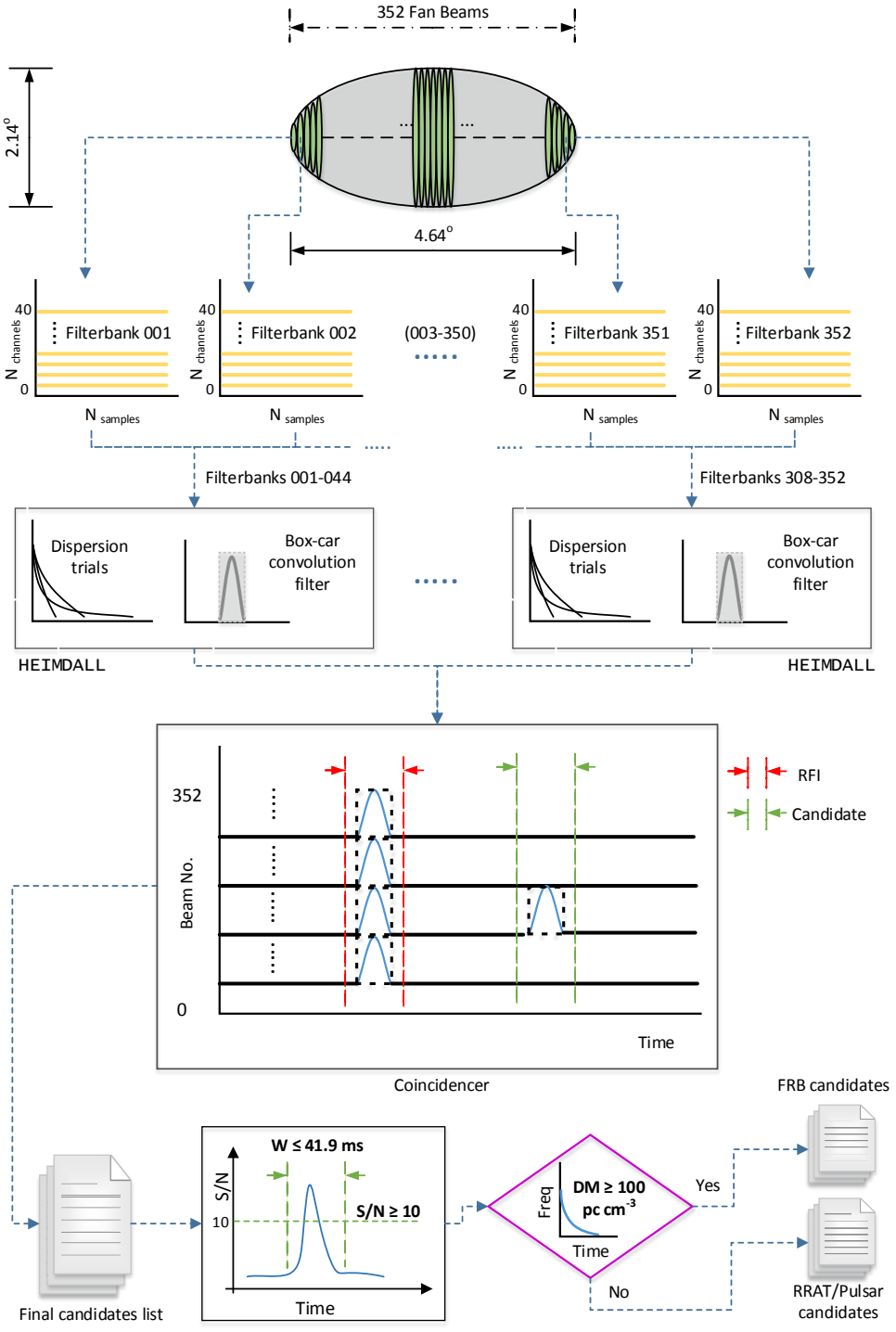

Figure 5.1 Fast transient search pipeline at UTMOST for FRB survey V2.0 (Caleb et al., 2016b). 352 data streams are obtained and the HEIMDALL single pulse pipeline dedisperses each time-frequency data stream to trial DMs in the range 0 to 2000 pc cm^{-3} and convolves the dedispersed time series with a series of boxcar filters to determine the width. The resulting data is then coincidenced to remove events that occur in multiple fan-beams at the same instant of time. The final list of candidates from HEIMDALL is then further filtered by applying additional cuts, before human scrutiny.

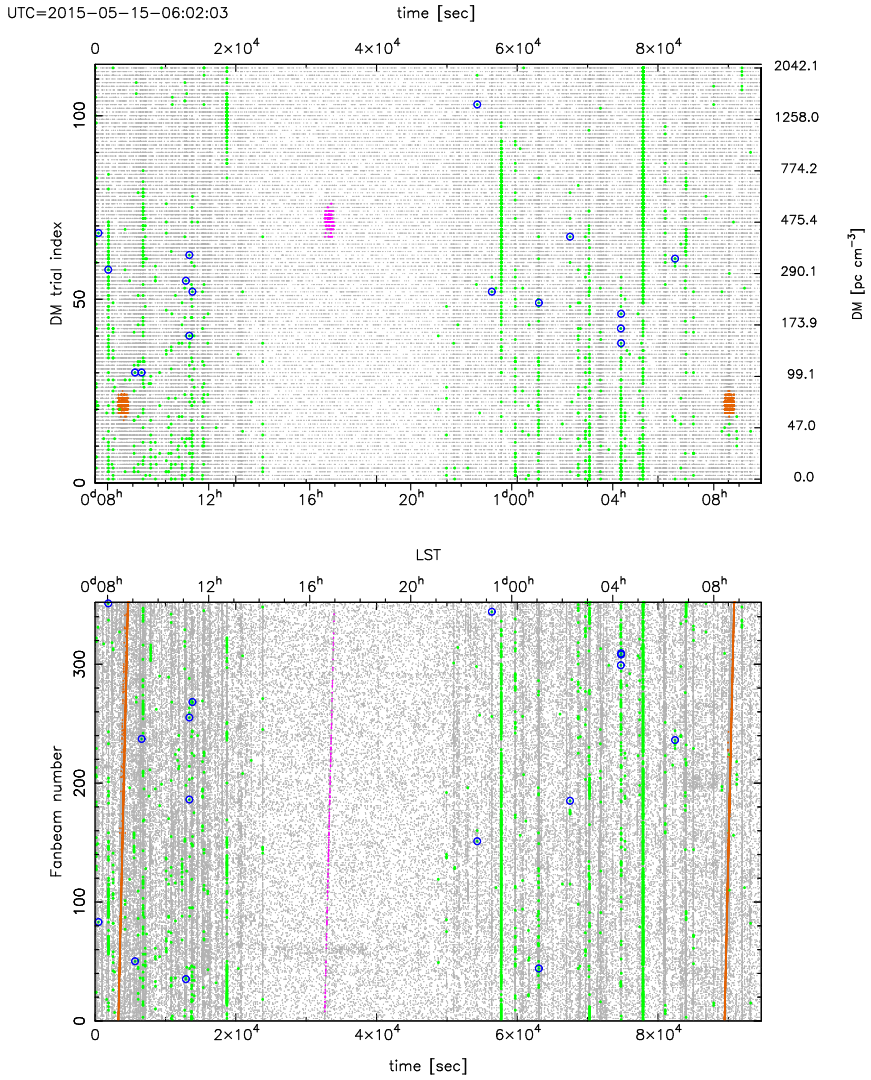

Figure 5.2 FRB transit search from survey V1.0 at UTMOST spanning 1.1 days, starting at UTC 2015-05-15-06:02:03. The telescope was parked on the meridian at $\delta = -46°$ Detections of the pulsars Vela and PSR J1644−4559 are shown by the orange and magenta points respectively. The lines are slanted at the sidereal rate as the objects pass through the fan beams on the sky. Events with a S/N < 10 are marked in grey, and FRB candidates by blue circles. Events with a S/N > 10 but which can be removed because they occur in 4 or more fan beams at the same time are marked in green. These are dominated by mobile phone calls in our observing band. Indicative DM values, for the DM trial indices are shown on the right side of the upper panel in pc cm^{-3}. All the FRB candidates turned out to be false positives from mobile phone calls, due usually to 20 ms narrow band emission. Events have been ignored if the total number seen in 10 second blocks exceeded 500 – this removes about half the events but only affects about 3% of the survey time-on-sky.

the bright Southern Hemisphere pulsars PSR J0835−4510 (Vela) and PSR J1644−4559 transiting through the beam once per sidereal period, as well as a bright unresolved phase calibrator, the radio galaxy J1935−4620, so that the phases and delays on the array can be checked every 24 hours. In practice, the array remains well phased over a few days, and the calibrator was merely used as a confirmation of phase stability. Individual pulses from both Vela and PSR J1644−4559 were routinely detected during each transit. The single pulses from PSR J1644−4559, with its rather high DM (478.8 $\mathrm{pc\,cm^{-3}}$) and widely spaced pulses ($P = 455$ ms), and average pulse fluence (29 Jy ms) have rather similar properties to FRB pulses, making it an excellent daily validation of the system performance. Figure 5.2 shows the passage of Vela (orange) and PSR J1644−4559 (magenta) through the 352 fan beams across the sky. Typically a few hundred candidates would be produced per 24 hours, and further analyses of these candidates is performed to look for FRBs.

The vast majority of the events in the search were RFI due to mobile phone handsets, which operate on 5 MHz bands in our frequency range. The false positive rate is of order 10^2 events per 12 hours across all beams in transit mode. Tests demonstrated that coincidencing is a very efficient means of rejecting RFI, primarily because UTMOST is an interferometer. Additionally techniques of spectral kurtosis and total power thresholding have been implemented to mitigate the RFI. The spectral kurtosis approach measures the similarity between the input signal and Gaussian noise. RFI typically is non-Gaussian and so this is useful in discriminating between the two (Bailes et al., submitted). The total power technique monitors and measures the median and median standard deviation for the preceding 8 seconds of data to determine when RFI causes the power levels to exceed pre-defined limits. The two techniques complement each other and result in relatively robust excision of transient RFI in an otherwise noisy environment.

Encouragingly, we redetected the bright pulsar PSR J1430−6623 in our FRB search V1.0, when the telescope was erroneously left surveying for 24 hours at its declination ($\delta = -66°$) in a true blind test of system performance. Pulse recovery tests were also performed by injecting fake FRBs by adding in total power at random positions into real filterbank data. The filterbank data chosen was RFI affected and contained bright pulses from the Vela pulsar. The fake events had injected S/Ns in the range 10 to 40, DMs in the range 300 to 2000 $\mathrm{pc\,cm^{-3}}$ and widths in the range 1 to 20 ms. Blind single pulse search techniques were used to process this fake data, identical to the method used for 'real' data processing. The injected FRBs were recovered with a success rate of order 95%. All the injected FRBs with relatively high S/Ns (S/Ns $\gtrsim 15$) were re-detected successfully and only a few with S/N = 10 were missed due to being amidst RFI.

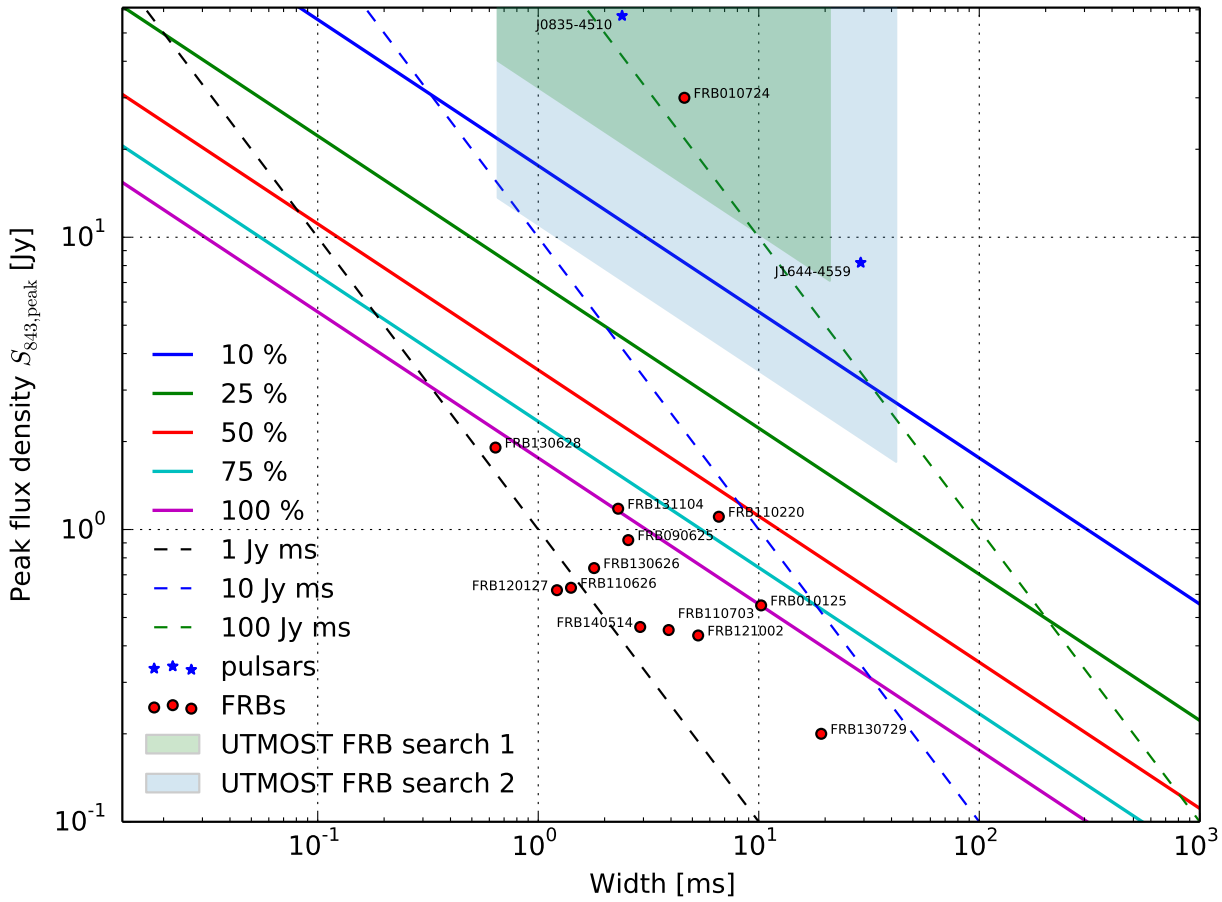

Figure 5.3 Single pulse sensitivities at UTMOST for FRB searches V1.0 (April 2015) and V2.0 (September 2015). Solid lines of constant S/N and dashed lines of constant fluence for different fractional sensitivities of the telescope are shown. Filled circles mark the FRBs published in literature and stars mark pulsars that have been detected through their single pulses by UTMOST. The green and blue shaded regions enclose the UTMOST surveys at the S/N limit for the sensitivities during the V1.0 and V2.0 surveys respectively.

5.3.1 FRB Survey V1.0

By April 2015, our upgrade of UTMOST had reached a sensitivity where we could perform an FRB survey as part of commissioning science. FRB searches commenced, covering the full UTMOST primary beam area of ~ 8 deg^2. The system was operated at only a fraction ($\sim 7\%$) of its final sensitivity, as not all modules had been recommissioned, only half the bandwidth was available (16 MHz of a final system bandwidth of 31.25 MHz ; with 20 coarse channels), and the individual modules were still in the process of being brought to full sensitivity. The data processing described in Section 5.3 involving dedispersion and box-car convolution by the HEIMDALL single pulse search software was performed offline by processing one filterbank at a time on a single GPU. We typically see of order 100 pulses from PSR J1644−4559, with single pulse S/Ns of ~ 20, when it transits the search area. From S/N measurements of the correlation amplitude of the quasar 3C 273 used to phase the array, we estimate $T_{\rm sys} = 400 \pm 100$ K. This $T_{\rm sys}$ yields a single pulse sensitivity of 23 $\pm$ 6 Jy ms for a millisecond duration even on boresight in the V1.0 search with UTMOST for a S/N of 10, using a gain of 1.4 K Jy^{-1} for 140 modules and a bandwidth of 16 MHz. We have attempted to verify the $T_{\rm sys}$ from transits of Vela, J1644−4559, J1731−4744 and J1752−2806. The uncertain flux densities yield a rather poor $T_{\rm sys}$ constraint with an uncertainty of a factor of 2. We set the $T_{\rm sys} = 400 \pm 100$ K for this survey.

At the time of FRB survey V1.0 the telescope was at about 7% of its design sensitivity. The search is thus sensitive to the brightest FRB reported to date referred to as a 'Lorimer' type burst (Lorimer et al., 2007), but not yet to the brightest of FRBs reported in Thornton et al. (2013). Assuming a Euclidean Universe, so that the cumulative number density of detectable events scales as $\mathcal{F}^{-3/2}$, we obtain a rate estimate of about one per 300 days with an error margin of 50%. With such a low sensitivity, our expectation of discovering an FRB was very low, but the survey allowed us to do many validation measurements on the FRB search pipeline. Our total search time on sky was 467 hours. No FRBs were detected down to a fluence of 23 Jy ms and a lower S/N limit of 10. Figure 5.3 displays this region (shaded in green) surveyed by UTMOST in survey V1.0. Assuming a 2σ upper limit of 4 events (Gehrels, 1986) on this null detection, 467 hours on sky and a search area of ~ 8 deg^2, this yields a 2σ upper limit on the FRB rate at UTMOST, of not more than 1000 events sky^{-1} day^{-1} at 843 MHz with a fluence greater than 23 Jy ms.

5.3.2 FRB Survey V2.0

In September 2015, we roughly doubled our search sensitivity by doubling the number of commissioned modules. In addition the installation of the second part of the GPU

correlator in May 2015 enabled us to process 31.25 MHz in 40 coarse channels. $T_{\rm sys}$ remained at 400 ± 100 K. The single pulses from the pulsar J1644−4559 were once again used to validate the system performance. On average we found the S/N of an individual pulse to be $\sim$ 40, a factor of 2 increase from the search V1.0, i.e. the searches were at about 14% of the design sensitivity. As previously mentioned, even though we are able to process the full 31.25 MHz bandwidth in this search, only 16 MHz of usable bandwidth resulted due to a sharp roll-off at the edges of the bandpass. The 10σ, 1 ms single pulse sensitivity during this search was 11 ± 3 Jy ms for a gain of 3.0 KJy^{-1}, bandwidth of 16 MHz and $T_{\rm sys}$ of 400 ± 100 K.

The FRB survey V2.0 was performed simultaneously with a pulsar timing programme. Additional coincidencing was performed by rejecting RFI induced events if they occurred in groups of 500 or more in 10 second intervals across all beams. The processes of dedispersion and box-car convolution by HEIMDALL, was performed in real-time by processing all 352 filterbank files in blocks of 44 on 8 GPUs. This increased sensitivity has enabled us to detect single pulses from several more pulsars. The RRAT J1819−1458 ($S_{\rm peak}$ = 3.6 Jy at 1.4 GHz) was also detected during commensal observations with Parkes at 1.4 GHz, and UTMOST at 843 MHz as shown in Figure 2.5. Figure 5.3 displays the area surveyed (blue and green) by UTMOST during the V2.0 FRB search with increased sensitivity. From Figure 5.3 we see that we are still only sensitive to 'Lorimer' type bursts. We spent 225 hours on sky and detected no FRBs down to the fluence limit of 11 Jy ms. From this null detection we obtain a 2σ upper limit of not more than 1000 events sky^{-1} day^{-1} at 843 MHz with a fluence greater than 11 Jy ms. We estimate the rate of FRBs given our current sensitivity at about 1 per 120 days with an uncertainty of 50%. Our non-detection is consistent with published FRB rate limits at Parkes, the Very Large Array (VLA) and the Allen Telescope Array (ATA) at 1.4 GHz, the Green Bank Telescope (GBT) at 800 MHz, the Low Frequency Array for Radio Astronomy (LOFAR) at 145 MHz and the Murchison Widefield Array (MWA) at 150 MHz (Figure 5.4) assuming the Euclidean scaling and 1 ms duration pulses. For comparison, the current estimated rate at 1.4 GHz at Parkes is $\sim$ 200 events sky^{-1} day^{-1} down to a fluence of 11 Jy ms (green circle in Figure 5.4) based on the rate of 2500 events sky^{-1} day^{-1} above 2 Jy ms by Keane & Petroff (2015). Using this scaled rate estimate at 1.4 GHz and our 2σ upper limit of 1000 events sky^{-1} day^{-1} at 843 MHz, we estimate the FRB spectra to be no steeper than a spectral index of −3.2, assuming FRBs were occurring during the duration of our observations and assuming a unbroken power-law spectral energy distribution (SED). We have also included the Thornton et al. (2013) rate of $1.0^{+0.6}_{-0.5} \times 10^4$ events sky^{-1} day^{-1} at 3 Jy ms (magenta

circle in Figure 5.4) and a lower limit of ~ 130 events sky^{-1} day^{-1} at 0.6 Jy ms (red circle in Figure 5.4) which is the event with the lowest fluence in Thornton et al. (2013). The rate of 5×10^3 events sky^{-1} day^{-1} above 1 Jy ms at 800 MHz from Masui et al. (2015) scaled to our 11 Jy ms fluence limit is $\sim$140 events sky^{-1} day^{-1}. From LOFAR at 145 MHz we estimate not more than ~ 1800 events sky^{-1} day^{-1} down to 11 Jy ms (green pentagon in Figure 5.4) based on the Coenen et al. (2014) upper limit of 150 events sky^{-1} day^{-1} brighter than 71 Jy ms. We obtain another upper limit with LOFAR at 145 MHz of $\sim 1.5 \times 10^4$ events sky^{-1} day^{-1} down to a fluence of 11 Jy ms (orange square in Figure 5.4) based on the Karastergiou et al. (2015) upper limit of 29 events sky^{-1} day^{-1} at 310 Jy ms assuming standard cosmological scaling for a fluence limited survey (viz. Section 5.4.3). The upper limit at 1.4 GHz at the VLA is $\sim 3.7 \times 10^3$ events sky^{-1} day^{-1} based on 7×10^4 events sky^{-1} day^{-1} on 0.9 Jy ms events (300 mJy events of 3 ms width - their Figure 9) (Law et al., 2015) and at the ATA is $\sim 7 \times 10^4$ events sky^{-1} day^{-1} based on an event rate of 48 events sky^{-1} day^{-1} above 440 Jy ms events (Siemion et al., 2012) scaled to the 11 Jy ms sensitivity at UTMOST. For the MWA we estimate a rate of not more than $\sim 3.5 \times 10^5$ events sky^{-1} day^{-1} down to a fluence of 11 Jy ms based on the upper limit of 700 events sky^{-1} day^{-1} at 150 MHz brighter than 700 Jy ms (Tingay et al., 2015).

5.4 Estimates of FRB rates at UTMOST

5.4.1 Extant estimates

Hassall et al. (2013) have estimated FRB rates that might be seen at a wide range of radio telescopes operating over a wide range of frequencies. They assumed the bursts to be standard candles, to have a constant spectral index and a constant co-moving space density. They estimated a detection rate of ~ 3 per day at MOST, but this is an overestimate for the present system being installed. The MOST telescope specifications they adopt from Green et al. (2012) are for a more ambitious upgrade path than the current UTMOST design, which has a bandwidth factor of 6 smaller and an FOV smaller by 60% (Bailes et al., submitted). We now estimate the rate of FRBs for the current upgrade at UTMOST using two methods, in both cases scaling from the event rate at Parkes.

5.4.2 Empirical scaling from events at Parkes

We compute what fraction of the Parkes FRBs would be detectable at UTMOST given its sensitivity for a pulse of S/N = 10 and $W = 1$ ms is $S_{\rm min} = 1.6$ Jy compared to $S_{\rm min} = 0.4$ Jy at Parkes. Thornton et al. (2013) discovered 4 FRBs in 24% of the high latitude

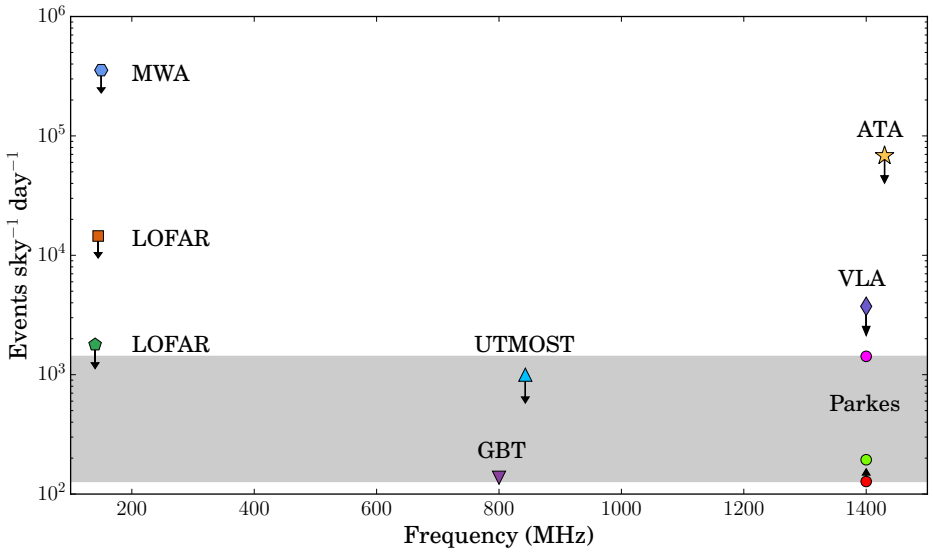

Upper limit of 48 events at 440 Jy ms at 1.4 GHz scaled to 11 Jy ms (Siemion et al. 2012)
Rate of 10^4 events at ∼3 Jy ms at 1.4 GHz scaled to 11 Jy ms (Thornton et al. 2013)
Lower limit of 10^4 events above 0.6 Jy ms at 1.4 GHz scaled to 11 Jy ms (Thornton et al. 2013)
Upper limit of 150 events at 71 Jy ms at 140 MHz scaled to 11 Jy ms (Coenen et al. 2014)
Upper limit of 29 events at 310 Jy ms at 145 MHz scaled to 11 Jy ms (Karastergiou et al. 2015)
Rate of 2500 events above 2 Jy ms at 1.4 GHz scaled to 11 Jy ms (Keane & Petroff. 2015)
Upper limit of 7 x 10^4 events at 0.9 Jy ms at 1.4 GHz scaled to 11 Jy ms (Law et al. 2015)
Rate of 5000 events above 1 Jy ms at 800 MHz scaled to 11 Jy ms (Masui et al. 2015)
Upper limit of 700 events at 700 Jy ms at 150 MHz scaled to 11 Jy ms (Tingay et al. 2015)
Upper limit of 10^3 events at 11 Jy ms at 843 MHz (This work)

Figure 5.4 Comparison of the non-detection of UTMOST with the published rate limits at different frequencies scaled to 11 Jy ms. Using the scaled rate of $\sim$ 200 events sky^{-1} day^{-1} at 1.4 GHz down to a fluence of 11 Jy ms (green circle) and our 2σ upper limit of 1000 events sky^{-1} day^{-1} at 843 MHz (blue triangle), we set a lower limit on the mean spectral index of FRBs of $\alpha > -3.2$ over this frequency range.

(Hilat) sub-survey of the high time resolution Universe survey and estimated a rate of $1.0^{+0.6}_{-0.5} \times 10^4$ events sky^{-1} day^{-1}. Champion et al. (2016) have discovered 5 more FRBs in the remaining 75% of the survey. Thus 9 of the known FRBs were discovered in the Hilat survey alone. To estimate their detectability at UTMOST, we reduce the S/Ns of these 9 FRBs by a factor of 4 due to UTMOST's lower sensitivity and account for reduction in their S/N by width-broadening due to the difference in observing frequency between Parkes and UTMOST. Only one Parkes event is found to be detectable at UTMOST.

The 9 FRBs at Parkes were discovered after processing 100% of Hilat. This corresponds to a rate of $R_{\rm Parkes} = 0.08 \pm 0.03$ events day^{-1}. Since only one of the nine Parkes FRBs is detectable at UTMOST, and the FOV is larger by a factor of 14, this yields an event rate estimate at UTMOST of $R_{\rm UTMOST} = 0.11 \pm 0.09\,{\rm events\,day^{-1}}$.

5.4.3 Event rate based on surveyed volume

Following (Hassall et al., 2013) we assume FRBs have flat spectral indices and are distributed through space in a Euclidean Universe, so that the cumulative number density of events with fluence $\mathcal{F}$, scales as $\propto \mathcal{F}^{\alpha}$ where $\alpha = -3/2$. Since the sensitivity of UTMOST is ~ 0.25 times that of Parkes, the events are expected to occur $4^{3/2} = 8$ times less often at UTMOST than at Parkes. Since the area surveyed at UTMOST by the beam is 14 times that of Parkes, the overall rate is 2 times higher. Thus a rate of 0.08±0.03 events day^{-1} at Parkes scales to a rate $R_{\rm UTMOST} = 0.16 \pm 0.06$ events day^{-1}. In Chapter 4, I show using Monte Carlo simulations of a cosmological population of FRBs, that the log$N$-log$\mathcal{F}$ relation for the Parkes events has a slope $\alpha \sim -1.0$, not as steep as the standard $\alpha = -3/2$ relation — adopting this shallower relation would elevate the rate at Molonglo, but we prefer to be conservative and use $\alpha = -3/2$, to estimate the UTMOST detection rate.

5.5 Discussion and Conclusions

The discovery of FRBs has opened up numerous exciting possibilities for the exploration of the extragalactic Universe: but their extragalactic/celestial origin is yet to be decisively established. With the newly upgraded UTMOST array, we will be able to affirm if these sources are truly extraterrestrial when we detect one (as we show in Chapter 6), as the array's Fresnel zone is at $\sim$ 14,000 km. FRB searches at two different fractional sensitivities (7% and 14%) were performed as part of commissioning science with the telescope parked at at $\delta = -46°$. The chosen declination was to allow the diurnal passage of bright southern

pulsars Vela and PSR J1644−4559 and a bright calibrator, radio galaxy J1935−4620, so that the system performance, phases and delays could be monitored. No FRBs were detected down to fluence limits of 23 Jy ms and 11 Jy ms after spending 467 and 225 hours on sky respectively.

We estimate FRB rates at UTMOST by scaling from the observed events at Parkes and by assuming a Euclidean flux distribution. Most importantly we assume a flat spectral index for both methods. The rates from the two methods at full sensitivity: 0.11 ± 0.09 events day^{-1} and 0.16 ± 0.06 events day^{-1}, are consistent within their uncertainties. We have used the simplest assumption sets one can apply to yield a rate at UTMOST which shows that at full sensitivity it will detect FRBs at twice the rate as at Parkes, and yet more effective still because of our near 24×7 access to the telescope. Given the duty cycle of Parkes and the estimated event rate, only a fully dedicated survey will be capable of detecting FRBs in sufficient numbers for interesting science to be performed. UTMOST is potentially the FRB discovery machine which will do this, as we see in the next chapter.

6

The first interferometric detections of Fast Radio Bursts

This Chapter (published as Caleb et al., 2017) presents the first interferometric detections of 3 FRBs with UTMOST. These detections place the origin of the bursts beyond the far-field region of the telescope thus ruling out local sources of interference as a possible origin. The predicted rate in the previous Chapter ($\sim 0.008 \pm 0.017$ events beam^{-1} day^{-1}) is found to be two times smaller than the observed rate at UTMOST ($0.017^{+0.03}_{-0.01}$ events beam^{-1} d^{-1}) but is consistent within the uncertainties, thus providing insights into their integral source count distribution and/or average SED (spectral index).

6.1 Introduction

The 18 FRBs published to date (refer to the FRBCAT repository[3] for the complete list) have been discovered in either post-processing of archival surveys or, in real-time, using the Parkes radio telescope with the exception of two, detected at the Arecibo (Spitler et al., 2014) and Green Bank telescopes (GBT; Masui et al., 2015) All but one of the bursts have been found at 1.4 GHz, with the exception being the GBT burst, which was seen at 800 MHz.

The observed FRB all-sky rate is very high. Champion et al. (2016) derive a rate of $7^{+5}_{-3} \times 10^3$ events sky^{-1} d^{-1} at 1.4 GHz for bursts between 0.13 and 1.5 Jy ms in fluence and widths in the range 0.128 ms to 16 ms. The high FRB rate is a major constraint on theories for their origin. Until recently, such theories have generally assumed they are cataclysmic events, in which the progenitor is obliterated. However, one FRB is now known to repeat in a non-periodic manner (FRB 121102, Spitler et al., 2016), opening up possibilities for other progenitor models. Following the discoveries reported

in this Chapter, Chatterjee et al. (2017) have achieved sub-arsecond localisation of the FRB 121102 using radio interferometric observations from the Very Large Array. The source has been localised to a $m_{r'} = 25.1$ AB mag low-metallicity, star-forming dwarf galaxy at $z = 0.19273(8)$ (Tendulkar et al., 2017). The precise localisation shows that the source is either co-located with a 180 μJy active galactic nucleus or an unresolved type of extragalactic source. However, the exact nature of the FRB progenitor is still unknown.

Despite concerted follow-up efforts for almost all FRBs, FRB 121102 is the only one seen to repeat. These efforts have been quite substantial. For instance, $\approx$ 80 hrs of followup for the Lorimer burst (Lorimer et al., 2007), and $\approx$ 110 hrs of selected FRB positions (Petroff et al., 2015b) at the Parkes radio telescope yielded no repeats. This suggests the possibility of there being two independent classes of FRBs – repeating and non-repeating – with two classes of possible progenitors (Keane et al., 2016). It is possible that the lack of repetition of pulses for the FRB discoveries at the Parkes radio telescope is merely due to limited sensitivity and follow-up time, and that all FRBs have a common origin (Scholz et al., 2016). FRB 010724 is an exception to this however: its extreme brightness ($\sim$ 30 Jy) far outweighs the lower gain of Parkes relative to Arecibo, so that one cannot infer its lack of repeat bursts is due to limited sensitivity. Recently, Ravi et al. (2016) have reported the detection of FRB 150708, which is of comparable brightness ($\sim$ 12 Jy) to FRB 010724, and exhibits 100 percent polarisation and suggests weak turbulence in the ionised IGM. DeLaunay et al. (2016) have associated a γ-ray transient with the FRB 131104 discovered by Ravi et al. (2015). However Shannon & Ravi (2017) in contrast, report on the discovery of a variable source (consistent with an AGN) temporally and spatially coincident with the FRB 131104 but not spatially coincident with the γ-ray burst, and rule out the association of the γ-ray burst with the FRB using probabilistic reasoning.

Most published FRBs have been detected with single dish antennas, with relatively poor angular resolution, and we are unable to indisputably rule out a near-field or atmospheric origin for the one-off events until now. The FRB detections made with the multi-beam receiver at the Parkes radio telescope however, are likely to originate at $\gtrsim 20$ km (Vedantham et al., 2016). Also FRB 150418 has been proposed to be associated with a galaxy at $z \sim 0.5$. However this association has been called into question by Williams & Berger (2016) and Vedantham et al. (2016), and other models like giant pulses from extragalactic pulsars which could account for the excess DM in the local environment, have been proposed (Connor et al., 2016b). Better localisation during discovery in the radio requires an interferometric detection.

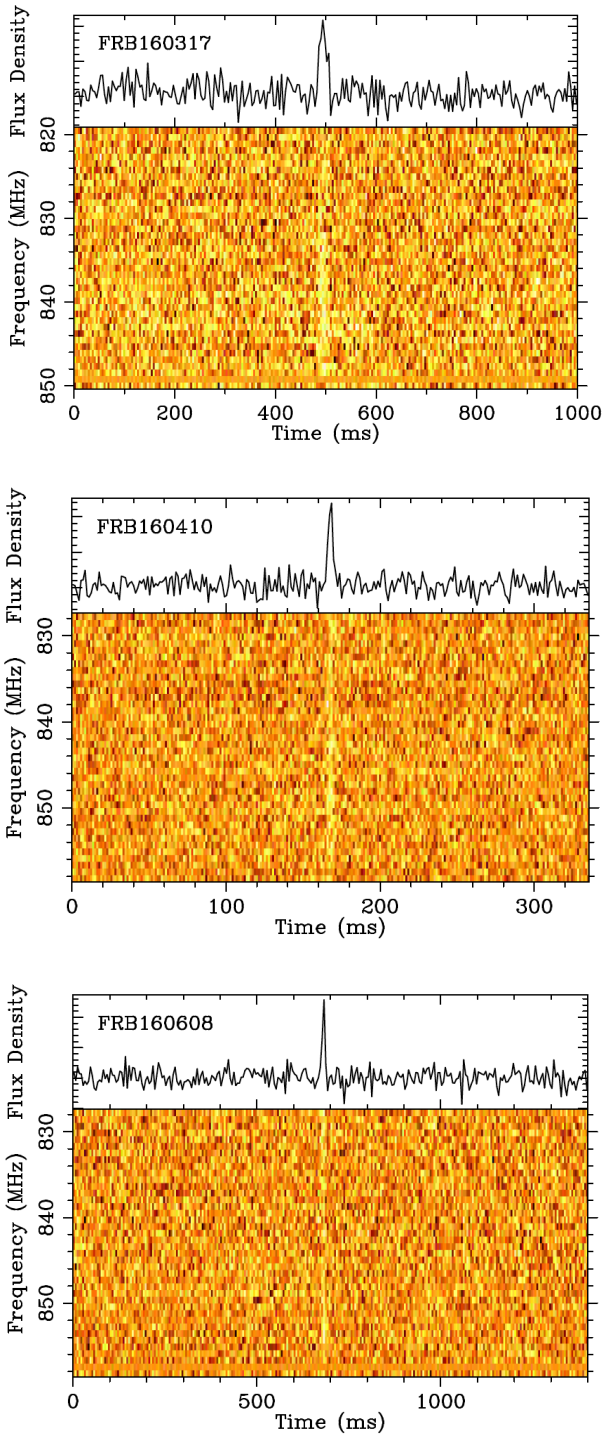

Figure 6.1 Frequency vs time behaviour of FRBs 160317, 160410 and 160608 detected at UTMOST at the centre frequency of 834.765 MHz. The top panel in each case shows the frequency-averaged pulse profile. The bottom panel shows that narrow-band RFI has been excised and the effects of inter-channel dispersion have been removed assuming DMs of 1165 ± 11, 278 ± 3 and 682 ± 7 pc cm^{-3} respectively. The data are uncalibrated as the bandpass of the system varies as a function of meridian angle, and the flux densities are in arbitrary units. Note the different time range on the abscissa for FRB 160410.

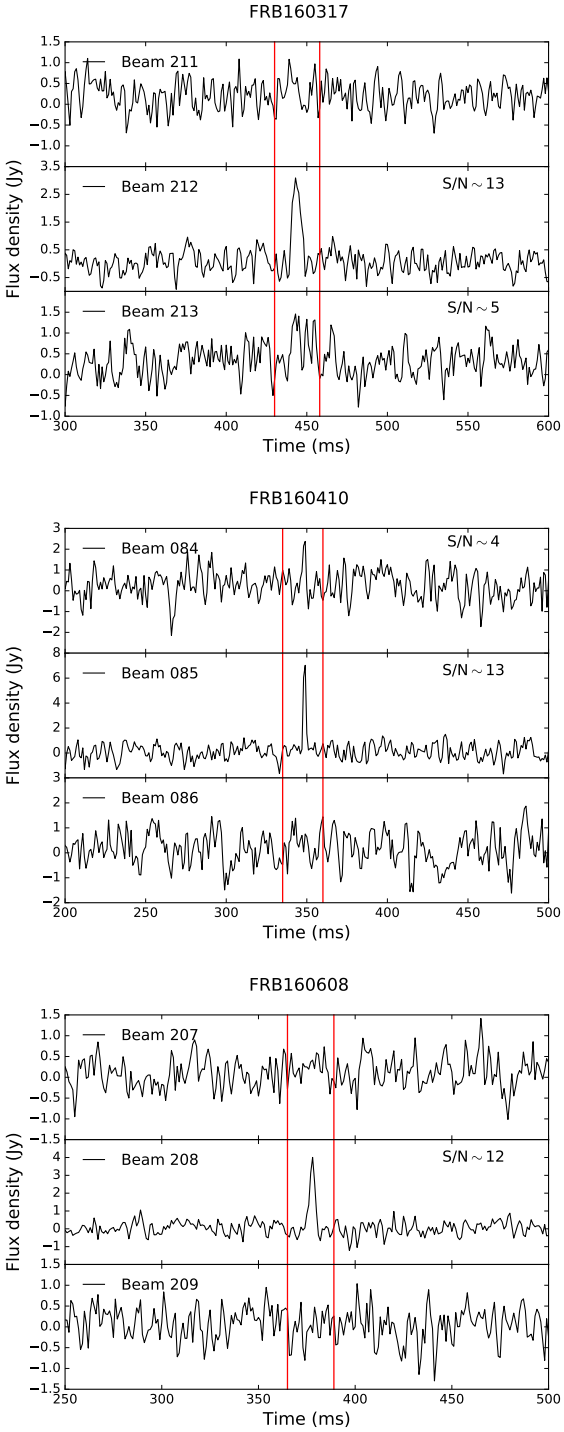

Figure 6.2 The three panels display the total power pulse profiles for one polarisation in three adjacent fan-beams. FRBs 160317 and 160410 were also detected as sub-threshold events in neighbouring fan-beams (in addition to the high S/Ns in the primary detection fan-beams), indicating that they did not occur near the centres of the primary fan-beam. On the contrary, FRB 160608 was only detected in one fan-beam suggesting that it occurred close to the centre of beam 208 (see bottom panel).

In Chapter 5, I describe how the Molonglo Observatory Synthesis Telescope (sited near Canberra in Australia) is currently undergoing a major upgrade, with the addition of a state-of-the-art correlator to transform it into an FRB finding machine (Bailes et al., submitted). Two FRB searches were performed with UTMOST in 2015 during the upgrade, when the system was operating at a small fraction of the final expected sensitivity, and only yielded an upper limit of the FRB rate of $\sim 10^3$ events sky^{-1} d^{-1} at 843 MHz (Caleb et al., 2016b). We have now undertaken a third FRB survey at UTMOST and discovered 3 FRBs. These are the first FRBs observed with an interferometer, further strengthening the case for an astronomical origin in addition to the detections at other telescopes and in the expected number of beams at Parkes for far-field events, as detection with UTMOST implies the events are in the far-field region $\gtrsim 10^4$ km. Section 6.2 of this chapter briefly outlines the telescope specifications, survey properties and the transient detection pipeline (see Figure 5.1). We present the bursts' properties and their follow-up observations and localisation areas in Section 6.3. The event rate estimates of the FRBs at 843 MHz based on the detections of the 3 FRBs and constraints on their spectral index are detailed in Section 6.4 followed by our conclusions in Section 6.5.

6.2 UTMOST specifications and survey properties

Since late 2015, we have been using UTMOST to search for fast radio transients for an average of 18 hours a day, while simultaneously timing more than 300 pulsars weekly (Bailes et al., submitted, Jankowski et al., submitted). In FRB search mode, the 4.0 degrees FWHP of the primary beam is tiled in the E-W direction by 352 elliptical, coherent, tied-array beams (called 'fan-beams', each 46″ wide), spaced 41″ apart and overlapping at very close to their half power points at 843 MHz. In the N-S direction the resolution of the fan-beams is the same as that of the primary beam (≈ 2.8 degrees). The fan-beams are numbered from 1 to 352 running from East to West across the primary beam, with fan-beam 177 directly centred on boresight. The sensitivity of the telescope to bursts can be estimated using the radiometer equation 2.5.

We define S/N as the ratio of the sum of the on-pulse flux to the product of the rms of the off-pulse flux and square root of the number of on-pulse bins ($\mathrm{S/N} = \frac{\mathrm{I_{on}}}{\sqrt{\mathrm{nbin}}\,\mathrm{I_{off}}}$). For the fully upgraded instrument, we expect $S_{\mathrm{min}} = 1.6$ Jy ms for a 10σ 1-ms wide pulse, 3.5 K Jy^{-1} gain, 100 K system temperature and 31.25 MHz bandwidth. The system bandwidth is however only about half of the initially anticipated 31.25 MHz bandwidth, as the ring antennas have a significant roll-off in sensitivity away from 843 MHz. This has been measured using integrated pulses from the pulsar J1644−4559. We find that

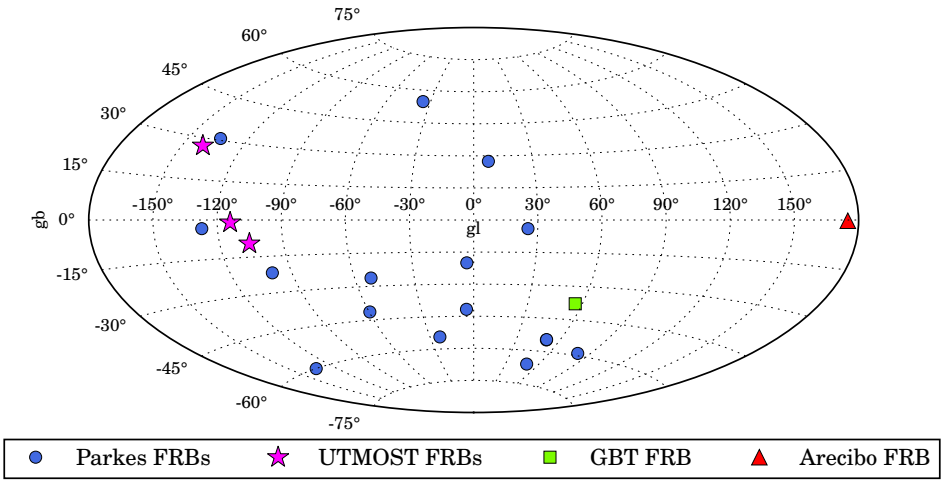

Figure 6.3 The sky distribution of the 18 FRBs published to date in Galactic coordinates. Dots mark the positions of the FRBs detected at the Parkes telescope, the triangle represents FRB 121102 detected at the Arecibo telescope and the square represents FRB 110523 discovered at the GBT. Stars mark the positions of the UTMOST FRBs. Two of the Parkes FRBs have positions separated by $9'$ which is not resolved in this figure. It should be noted that there are large biases in this distribution due to very different sky coverages and survey depths.

on average ~ 86 percent of the total S/N is concentrated in the upper half of the band ($\sim 836 - 850$) as the antennas are tuned to maximum sensitivity at 843 MHz. We adopt a bandwidth of 16 MHz for the sensitivity calculations in the work, to be conservative.

During the upgrade, we characterise the system sensitivity by a fraction of the final expected gain ϵ. This factor encompasses systemic losses due to (1) pointing errors (from physical misalignment in the modules N-S, and phasing errors in the antenna system E-W), (2) self-generated radio frequency interference (RFI) mainly due to improperly shielded electronics in the receiver boxes near the telescope, (3) coherent noise in the receiver boxes, which affects some sets of adjacent modules, and other inefficiencies in the system performance that we are still characterising, such as systematic errors in the phase/delay solutions across the interferometer (Bailes et al. in submitted).

At present (October 2016), we estimate $\epsilon \approx 0.14$, based on observations of strong calibrators of known flux densities and a number of high DM pulsars with relatively stable flux densities. This implies an effective $T_{\rm sys}$ of 400 ± 100 K. This is significantly higher than the system temperature seen on the best performing modules, which can be as low as 100 K. We note that ϵ can vary from day to day as modules are either serviced in the field or have electronics maintenance in the workshops, and typically lie in the range $0.15 < \epsilon < 0.20$. Occasionally, if only one arm is operational, we have the option to

continue surveys at half sensitivity (i.e. $0.07 < \epsilon < 0.10$). The telescope can access the Southern sky for $\delta < +18°$, and for most parts of the sky we tend to observe reasonably close to the meridian, in order to maximise sensitivity. The sensitivity is reduced by projection effects away from the meridian.

In November 2015, we commenced our third FRB survey "V3.0". It ran for a total of 159.0 days on sky (between 01-11-2015 and 30-11-2016), at $\epsilon \approx 0.14$ of the final target telescope sensitivity. Our fluence limit of the survey, that is the fluence of the narrowest detectable pulse $\mathcal{F}_{\rm lim}$ can be parametrized as,

$$\mathcal{F}_{\rm lim} \approx 11 \left(\frac{W}{\rm ms} \right)^{1/2} \rm Jy\,ms \tag{6.1}$$

where, 11 Jy is the UTMOST flux limit for S/N = 10, $G = 3.0$ K Jy^{-1}, $\Delta\nu = 16$ MHz, $W = 1$ ms, $N_{\rm p} = 1$ and $T_{\rm sys} = 400$ K. It should be noted that this is not the same as the fluence completeness limit $\mathcal{F}_{\rm complete}$. Between $\mathcal{F}_{\rm lim}$ and $\mathcal{F}_{\rm complete}$ we are incomplete and not all FRBs with fluences in this range are detectable. This incompleteness region corresponds to the pink shaded region in Figure 6.7. The two previous surveys (V1.0 and V2.0) reported in Caleb et al. (2016b) yielded no FRB events. Relative to V3.0, V1.0 ran for 19.5 days at lower sensitivity ($\epsilon = 0.07$), while V2.0 operated for 9.4 days at the same sensitivity ($\epsilon = 0.14$).

FRB survey V3.0 consists primarily of pointings taken commensally during pulsar timing observations. In this mode, the time series data from 352 fan-beams are searched for dispersed single pulses in real time, using a custom version of the heimdall software on 8 Nvidia GeForce GTX TITAN X (Maxwell) GPUs with a latency of 8-s. The resulting candidates were then processed offline, typically the following morning for overnight pulsar timing (RFI is much reduced at night, and the telescope is made available for maintenance on week days). On weekends, the telescope is usually operated continuously. The candidate processing pipeline used is described in detail in Caleb et al. (2016b). The process followed is:

1. obtain 352 data streams (8-bits/sample), one for each fan-beam, at 655.36-μs sampling

2. search time series for single pulses with width, $0.65536 < W < 41.943$ ms ($W = 2^{\rm N} \times 0.65536$ ms, where N = 0,1,2...) and DMs in the range $100 <$ DM < 2000 pc cm^{-3},

3. remove events occurring simultaneously in more than 3 fan-beams at a given instant

in time,

4. classify only events with S/N $\geq$ 10, DM $\geq$ 100 pc cm^{-3} and $W \leq$ 41.943 ms as potential FRB candidates. These then require human scrutiny of the diagnostic plots, to remove candidates that were RFI, almost always due to narrow-band mobile handset emissions in our operating passband and single pulses from known pulsars.

6.3 Results

The false positive rate at UTMOST is high due to RFI caused by mobile phone handsets, which produce narrow band (5-MHz) emission in our band, typically in $\approx$ 20 ms pulses. These can be eliminated because celestial pulses are expected to be broadband, modulated by a frequency dependent response across the 31.25 MHz bandwidth. This process has been validated using individual pulses from about 20 bright pulsars seen to date. We are presently automating this process using machine learning algorithms, so that pulses can trigger a full voltage dump of the raw data while they are still in the $\approx$ 30 seconds of ring buffer storage, with alerts issued in near real-time. RFI occurs predominantly at low DM, but the rate is high enough to produce a few hundred spurious candidates above our DM limit of 100 pc cm^{-3} daily. Candidates were typically vetted each morning after data taking.

In 2016 March, April and June we made the first interferometric detections of FRBs at 843 MHz: FRB 160317, FRB 160410 and FRB 160608, as shown in Figure 6.1. The independent discovery of FRB 160608 by Wael Farah using a separate processing pipeline, validated our single pulse pipeline. All 3 bursts show the characteristics attributed to FRBs, namely a broadband dispersive sweep and a clear distinction from other candidates in the single-pulse search pipeline (described in Section 6.2). Comments on the individual observations which yielded FRBs follow:

6.3.1 FRB 160317

This was detected on 2016 March 17 at 09:00:36.530 UTC while observing an X-ray magnetar SGR 0755−23, in response to an Astronomers Telegram (Barthelmy et al., 2016). The burst occurred about 0.4 degrees East of the magnetar, and was detected $\sim$1° off the Galactic plane with a DM of 1165(11) pc cm^{-3}. The DM due to the ISM at this sight-line is $\sim$ 320 pc cm^{-3} from the NE2001 model by Cordes & Lazio (2002) and $\sim$ 395 pc cm^{-3} from the YMW16 model (Yao et al., 2017). The burst with S/N $\sim$ 13, occurred

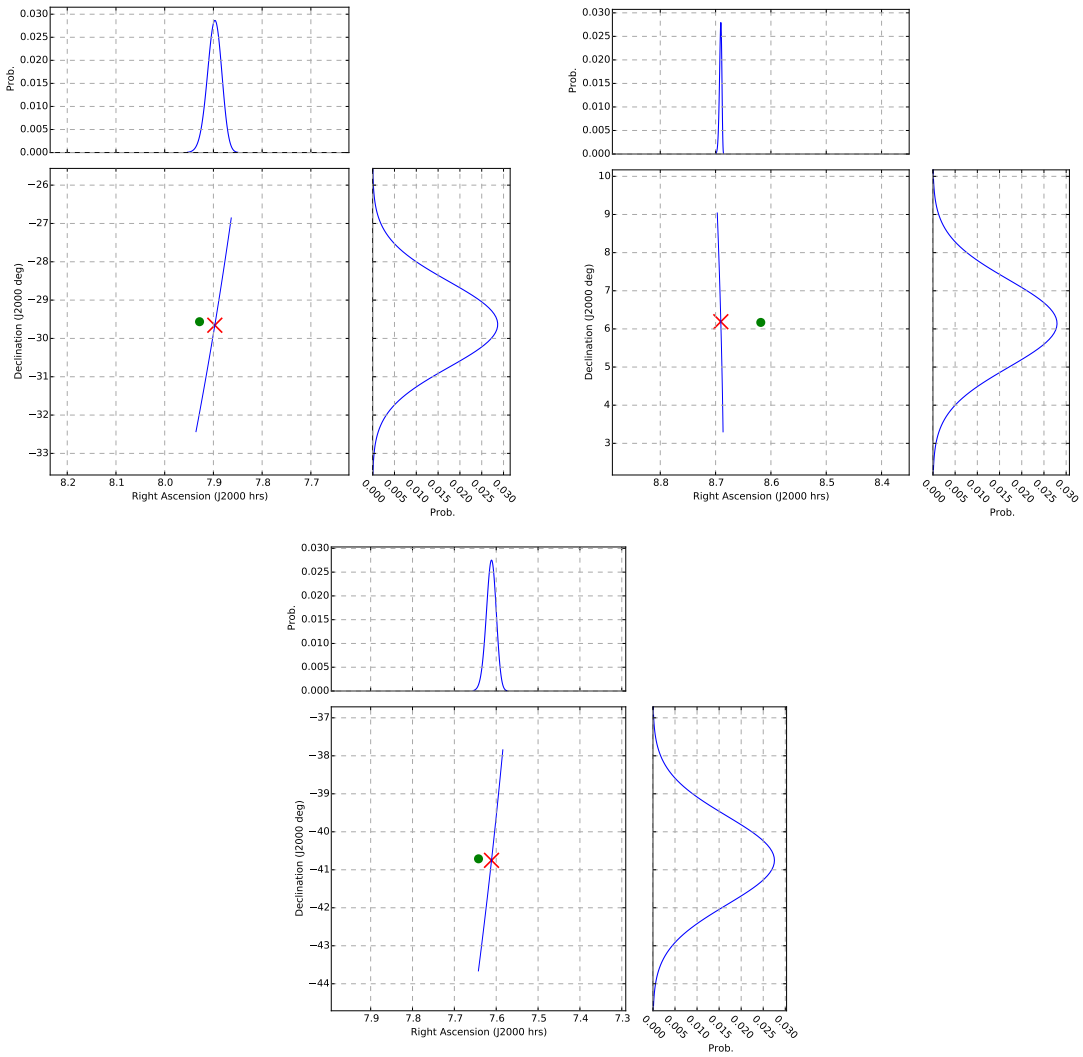

Figure 6.4 We show 3σ ($15'' \times 8.4°$) localisation ellipses of FRB 160317 (top-left), FRB 160410 (top-right) and FRB 160608 (bottom-centre). The maximum probability in RA (J2000) and DEC (J2000) assuming a Gaussian probability density function gives the most likely position of the FRB, and is marked by the cross. The dot indicates the position of the "boresight" pointing of the telescope. Typically, a pulsar is being timed at this position in the telescope beam. In 2 out of 3 cases, the pulsar at this position was bright enough to see individual pulses during the observation when a FRB was detected. The coordinates of the ellipses are given in Table B.1.

East of the centre of the primary fan-beam of detection (Beam 212) since it appeared weakly in the adjacent fan-beam with S/N ~ 5 (Beam 213) as shown in Figure 6.2.

6.3.2 FRB 160410

Similarly to FRB 160317, this FRB was also detected in two adjacent fan-beams (Beam 085 with S/N $\sim$ 13 and Beam 084 with S/N $\sim$ 4) as seen in Figure 6.2. A single dispersed pulse was discovered on 2016 April 04 at 08:33:39.680 UTC, in an observation of the pulsar J0837+0410 at the telescope's boresight. This pulsar is so bright that individual pulses were seen from it as the FRB occurred, meaning the flux density scale and bandpass response of the observation were well understood. The FRB was seen $\sim 1^\circ$ away from boresight. This pulse was detected at Galactic latitude, $\sim 27^\circ$ with the LOS DM accounting for only $\sim$ 58 pc cm^{-3} of the total observed DM from the NE2001 model. The YMW16 model estimates $\sim$ 63 pc cm^{-3}. FRB 160410 has the lowest DM excess $\sim$ 220 pc cm^{-3} of any published FRB, potentially making it the closest FRB discovered to date and an excellent candidate to search for repeat pulses.

6.3.3 FRB 160608

The burst occurred in an observation of the pulsar J0738−4042 at $l = 254.11$ deg and $b = -9.54$ deg on 2016 June 06 at 03:53:01.088 UT with a total DM of $\sim$ 682 pc cm^{-3} and $\sim$ 238 pc cm^{-3} contribution from the Milky Way (NE2001). The YMW16 model's estimate however is $\sim$ 310 pc cm^{-3}. It was seen $\sim 0.5^\circ$ from the boresight position. FRB 160608 was detected with S/N $\sim$ 12, just above the detection threshold of 10 and it occurred towards the centre of the primary detection fan-beam (Beam 208). No pulse was detected in the adjacent fan-beams (see Figure 6.2). This was initially of concern, but tests with the Vela pulsar placed sufficiently far South of the telescope boresight, to produce an individual pulse with the same S/N showed that detection in a single fan-beam occurred $\approx$ 20% of the time. The localisation of this FRB is thus slightly poorer ($21'' \times 8.4^\circ$) than for the other two FRBs, for which 2 fan-beam detections allow more accurate positions.

The primary advantage of the array is that a pulse from a far-field point source is detected in a maximum of 3 adjacent fan-beams at any given time, confirmed by extensive

[1] https://github.com/evanocathain/destroy_gutted
[2] http://psrchive.sourceforge.net/
[3] https://github.com/frbcat/FRBCAT_analysis

Table 6.1 Table of observed and inferred properties of the 3 FRBs in this work. The UTCs are the barycentric start times of the observations and the times at which the events occurred. Sky coordinates are the most likely positions of the FRB event within a narrow error ellipse (see Figure 6.4). The peak fluxes ($S_{\rm peak,obs}$) are computed using the radiometer equation and the DM contribution from the Milky Way ($\rm DM_{Gal}$) is calculated using the NE2001 model (Cordes & Lazio, 2002). The "boresight fluence" is the detected fluence corrected for the primary beam and fan-beam responses. They are shown as lower limits, for the unknown correction to higher fluence along the semi-major axis of the detection fan-beam. The isotropic energy E_0, is the energy at source and $\tau_{843\,\rm MHz}$ is the DM smearing due to the pulse broadening caused by the incoherent dedispersion at the observing frequency. The observed widths and their uncertainties shown in parentheses are measured using the DESTROY[1] single pulse search software, PSRCHIVE[2] and scripts made publicly available through the FRBCAT repository[3]. The redshift z is computed as $(\rm DM_{FRB} - DM_{Gal,NE2001})/1200$ (Ioka, 2003; Inoue, 2004). The luminosity and co-moving distances are calculated for a standard, flat-universe ΛCDM cosmology using COSMOCALC (Wright, 2006). The boresight sources are the magnetar or pulsars that were being observed during the time the FRB occurred.

Parameter	FRB 160317	FRB 160410	FRB 160608
UTC start	2016-03-17-08:30:58	2016-04-10-08:16:54	2016-06-08-03:52:24
UTC event	2016-03-17-09:00:36.530	2016-04-10-08:33:39.680	2016-06-08-03:53:01.088
RA J2000 (hh:mm:ss)	07:53:47	08:41:25	07:36:42
DEC J2000 (dd:mm:ss)	−29:36:31	+06:05:05	−40:47:52
l (deg)	246.05	220.36	254.11
b (deg)	−0.99	27.19	−9.54
Detection S/N	13	13	12
$S_{\rm peak,obs}$ (Jy)	> 3.0	> 7.0	> 4.3
Boresight Fluence (Jy ms)	> 69	> 34	> 37
Isotropic energy, E_0 (J)	$\sim 10^{34}$	$\sim 10^{32}$	$\sim 10^{33}$
Observed width, W (ms)	21(7)	4(1)	9(6)
DM smearing, $\tau_{843\,\rm MHz}$ (ms)	12.6	3.0	7.4
$\rm DM_{FRB}$ (pc cm^{-3})	1165(11)	278(3)	682(7)
$\rm DM_{Gal,NE2001}$ (pc cm^{-3})	319.6	57.7	238.3
$\rm DM_{Gal,YMW16}$ (pc cm^{-3})	394.6	62.5	310.3
Inferred redshift, z	0.7	0.2	0.4
Luminosity Distance (Gpc)	4.30	0.89	1.97
Co-moving Distance (Gpc)	2.52	0.75	1.44
Boresight source	SGR 0755−2933	J0837+0610	J0738−4042

pulsar observations. RFI is typically near-field (with the exception of satellite based RFI), and predominantly appears in more than 3 adjacent fan-beams, meaning that it can be reliably excised to reduce false positive rates when searching for transients. Using the adjacent fan-beam detections of FRB 160317, we have modelled the point of separation between the near-field or Fresnel region and the far-field or Fraunhofer region of the telescope. Assuming a point source at a range of distances from $1 - 10^6$ km, we compute the S/N for a tied-array beam (e.g. fan-beam 212) phased at an offset of 0.3 from the centre of the beam to ensure a two fan-beam detection. We compute the path length to each module, the phase of the signal along the array and perpendicular to the array, and add all these as a vector sum weighted by the module performance, to get the "boresight" S/N. We see that in Figure 6.5 at a distance of $\gtrsim 10^4$ km, we achieve a two fan-beam detection with S/N ~ 13 in the primary detection beam and S/N ~ 5 in the secondary detection beam, similar to the FRB being modeled. Detections of FRBs in 1 or 2 fan-beams only, thus allow us to identify them as sources more distant than this, placing them well away from the Earth and hence effectively rule out sources of local origin.

The discovery observations containing the FRBs were carefully inspected to check for similar events at the same time and with the same DM as the FRB, in other fan-beams. No other broadband pulses were detected in any other fan-beams within approximately 60 seconds of the bursts. Moreover, in addition to all the tied array fan-beams, we form a single special fan-beam as the incoherent sum of all the other fan-beams. This "total power" fan-beam was also searched for events near the UTC of the 3 bursts. For the 3 FRBs, this fan-beam contained no unusual sources of RFI. Only twice during the 3 surveys did we find FRB-like candidates (i.e. appearing across the band and showing an apparent DM sweep) which were identified as RFI upon closer analysis. In each case, similar events could be found in dozens to hundreds of fan beams, and were thus obvious near-field RFI. These false candidates also had 'patchy' power across the observing band, indicative of RFI generated from different carrier handsets operating at the same time in our band.

Two of the three FRBs have been discovered relatively close to the Galactic plane, with the locations marked as stars in Figure 6.3. All three have DMs significantly in excess (by at least a factor of 3) of the Galactic contribution, suggesting an extragalactic or cosmological origin. Under this assumption, the contribution from the IGM to the DM can be used to infer a redshift, using the scaling relation in Ioka (2003) and Inoue (2004). This places FRBs 160317, 160410 and 160608 at redshift upper limits of 0.7, 0.2 and 0.4 respectively, assuming zero contribution from any potential host galaxy. Any contribution from a host galaxy or the immediate vicinity of an associated source, could be a significant

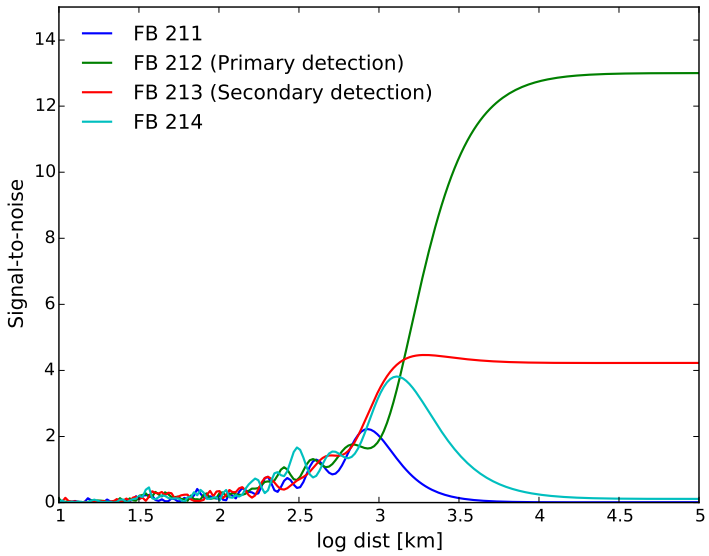

Figure 6.5 Simulations of the detections of FRB 160317 in adjacent fan-beams (FB) to determine the Fresnel limit of the telescope. At a distance of $\gtrsim 10^4$ km, the S/Ns of the modeled pulse in FB 212 and FB 213, match that of the observations with non-detections in the other fan-beams.

fraction of the total DM depending on its orientation and location. The average DM for elliptical galaxies is 37 pc cm^{-3} and for spiral galaxies it is 45 pc cm^{-3} based on the probability distribution of DMs computed for a range of host galaxies (Xu & Han, 2015). For spirals, the weighted average over a range of inclination angles is estimated to be 142 pc cm^{-3}. However the host contribution to the DM from high redshift galaxies can be small due to cosmological time dilation and the corresponding redshifting of frequency (Zhou et al., 2014). It also does not account for any bias in FRB locations within galaxies.

The S/Ns, DMs and widths of all three FRBs have been computed using the DESTROY single pulse search software, PSRCHIVE, and with scripts made publicly available through the FRBCAT repository. The observed widths of all three FRBs are dominated by dispersion smearing as shown in Table 6.1. This is due to our small bandwidth and limited number of channels (40 channels). We have now implemented a fine channel mode (320 channels) which will potentially increase our sensitivity and the FRB detection rate by a factor of $\sqrt{8}$. Our total bandwidth of only 31.25 MHz is too narrow to permit a measurement of dispersion index. Single pulses from the Vela pulsar were used to test our sensitivity to the DM index. The DM and the DM index δ where

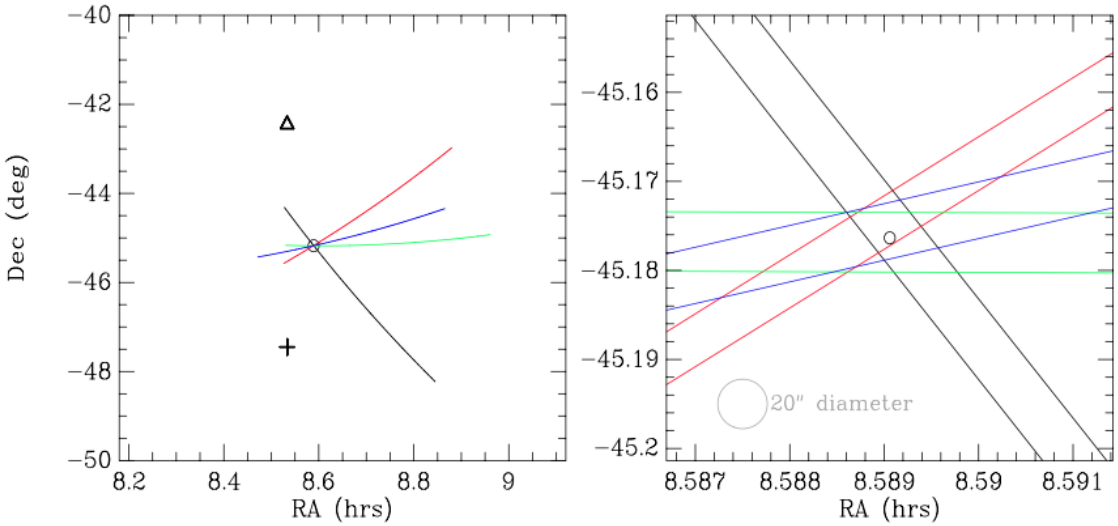

Figure 6.6 Left panel: Localisation contours for four single pulses from Vela, observed over different hour angles and distances from the telescope boresight. The triangle marks the boresight position for the black fan-beam and the cross marks the boresight position for the three other fan-beams. Right panel: A zoom into the 3σ error ellipse for the position of the source on the sky. The circle indicates the position of the pulsar. Even a single repeat of an FRB at a different hour angle, could constrain the position to a few arcsec radius shown in localisation contours in the right panel.

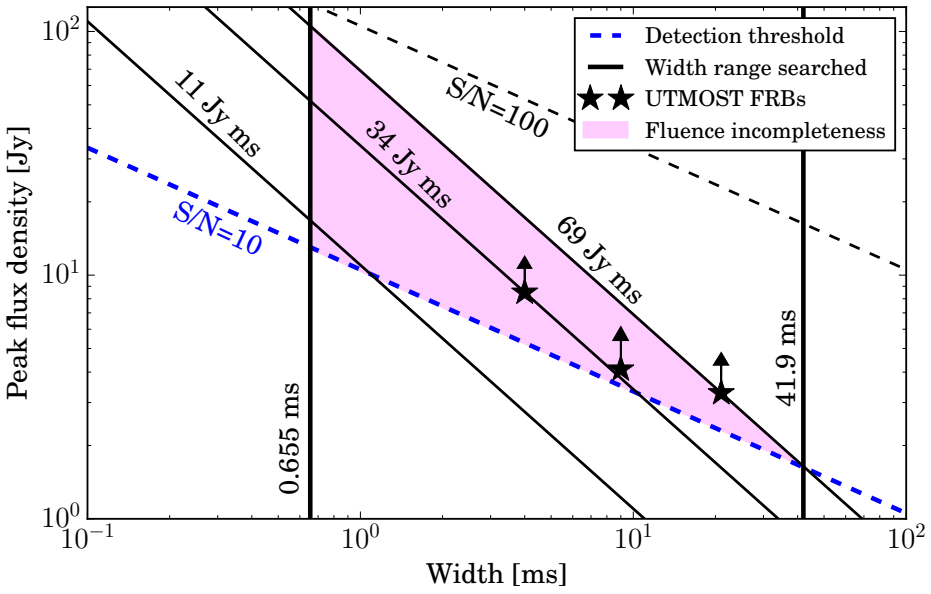

Figure 6.7 Boresight corrected peak flux density versus observed width for the 3 FRBs. Dashed lines represent lines of constant S/N and solid lines represent lines of constant fluence. The range of widths searched is enclosed by the solid vertical lines. The pink region is the fluence incomplete region which indicates that pulses with the same fluence but different widths are not equally detectable. Only pulses above 69 Jy ms are detectable across the entire width range searched at UTMOST.

the dispersive delay is given by,

$$\Delta t \propto \Delta\nu^{-\delta} \tag{6.2}$$

are found to be highly correlated, so that we can place no practical limit on δ. We therefore set the DM index to $\delta = -2$.

6.3.4 Localisation

All 3 FRBs were discovered while following up known sources, which were at "boresight", and thus centred on Beam 177. We localise each FRB's position on the sky, using the angular separation between the FRB's position in fan-beam space from the boresight fan-beam. The 1σ uncertainty in the direction of the semi-major axis is defined by the primary beam ($\sim 2.8°$) while the uncertainty in the semi-minor axis is controlled by the fractional S/N measured from the adjacent fan-beam detections. For FRBs detected in adjacent fan-beams, we perform a simple linear interpolation based on the S/N to localise the event in the fan-beam grid. For the FRB with a single fan-beam detection only, we assume the

centre of the fan-beam for the localisation. This allows us to construct a trace on the sky relative to the boresight (RAJ, DECJ), taking into account the meridian angle of the observation at the time of the FRB, and the known, slight skew and tilt of the East-West arms relative to true East-West and horizontal. The trace is a strong function of the hour angle of the observation, as one would expect in an East-West array. The uncertainty in the direction of the semi-minor axis was confirmed observationally using single pulse detections from bright pulsars. Single pulses that were detected in two adjacent fan-beams with S/N similar to our FRBs were chosen to estimate our localisation accuracy on the sky. These fan-beam localisations were then compared to the true position of the pulsar. The 1σ scatter of the calculated position of the pulsar from individual pulses, compared to the known position of the pulsar, is ~ 0.1 fan-beams or $\sim 5''$, in the direction perpendicular to the fan-beam. For single fan-beam detections at low S/N, a similar analysis yielded a slightly poorer localisation precision of $7''$. Two of the FRBs found with UTMOST have FWHP error ellipses of $5'' \times 2.8^\circ$ (~ 11 arcmin^2) on the sky as seen, in Figure 6.4. For comparison, single beam FRB detections (with FWHP beamwidth of $14.0''$) at Parkes, are localised to ~ 160 arcmin^2. The probability density of the localisation is shown in right ascension (RA) and declination (DEC), with the cross marking the most likely position of the burst for each FRB.

One of the advantages of UTMOST is that we can localise pulses to a few arcsec radius if the source is observed at different hour angles. The tilt of the error ellipses seen in Figure 6.4 demonstrates this and is a result of the geometry of the telescope. The most likely position of the FRB is marked by the cross. The fan-beams rotate in position according to the hour angle pointing of the telescope. A repeat FRB pulse, at a significantly different hour angle, allows us to localise the bursts to a few arcsec, depending on the S/N of the event. We have tested this scenario using individual pulses from four different pulsars, with results for four different hour angles (and offsets from boresight) for the Vela pulsar shown in Figure 6.6. Localisations to about $5''$ accuracy, or 0.1 fan-beam widths, should be possible for a bright, repeating FRB.

UTMOST is part of the shadowing campaign of the SUrvey for Pulsars and Extragalactic Radio Bursts (SUPERB) at the Parkes radio telescope (Keane et al., 2017). An FRB detected simultaneously with Parkes and UTMOST will yield a good localisation (few arcmin $\times$ few arcsec) even if the burst does not repeat. The sky positions of the 3 FRBs were also re-observed at different HAs, to look for additional bursts. We spent 105 hours following FRB 160317, 43 hours on FRB 160410 and 35 hours on FRB 160608. The data were searched offline for pulses with S/N ≥ 10 and with

±20% of the DM of the FRB, using the pipeline described in Section 6.2. No repeat pulses were found from any of the FRB positions.

6.4 FRB event rate at UTMOST

6.4.1 Event rate analysis

Connor et al. (2016a) present detailed analyses constraining FRB rates at various telescopes, scaling from a single FRB discovered at 800 MHz at the GBT (FRB 110523) (Masui et al., 2015). They estimate a rate of $0.42^{+1.96}_{-0.32}$ d^{-1} at UTMOST operating at its design sensitivity, based on comparisons between the sensitivities and areas surveyed by the two telescopes. This estimate is consistent with Caleb et al. (2016b). Using the same method as outlined in Connor et al. (2016a) we calculate a rate of $0.014^{+0.05}_{-0.013}$ d^{-1}, which agrees with the rate we measure at UTMOST. We have spent a total of 180 days on sky and discovered 3 FRBs with a FOV of 8.8 deg^2. Based on this, we measure a detectable event rate of ($\mathcal{R}$),

$$\mathcal{R}\left(\mathcal{F} \gtrsim 11\,\mathrm{Jy\,ms}\right) \gtrsim 0.78^{+1.24}_{-0.57} \times 10^2\,\mathrm{events\ sky^{-1}\,d^{-1}} \tag{6.3}$$

at the 95% confidence level (Gehrels, 1986), above a full power boresight fluence of 11 Jy ms as parametrised by Equation 6.1, at the half-power FOV. The rate is given as a lower limit since all searches are incomplete in the fluence-width plane. Following Keane & Petroff (2015), our fluence complete rate is

$$\mathcal{R}\left(\mathcal{F} \gtrsim 69\,\mathrm{Jy\,ms}\right) \sim 5.0^{+18.7}_{-4.7}\,\mathrm{events\ sky^{-1}\,d^{-1}}, \tag{6.4}$$

as shown in Figure 6.7.

In chapters 4 & 5 we have made estimates of the event rate expected at UTMOST, scaling from the event rate at Parkes, under assumptions about the integral source count distribution (log$N$-log$\mathcal{F}$ relation) and the spectral index of FRBs. To do this we assume that the spectral energy distribution is flat between the Parkes 1.4 GHz and UTMOST's 843 MHz operating frequencies, and that the source count distribution scales as,

$$N(>\mathcal{F}_{\mathrm{lim}}) = \mathcal{F}_{\mathrm{lim}}^{\alpha} \tag{6.5}$$

where $\alpha = -3/2$ for events populated in a Euclidean Universe. Under these assumptions, Caleb et al. (2016b) predict a rate of $\gtrsim 0.008(0.004)$ events d^{-1} for a 10σ, 1-ms wide FRB

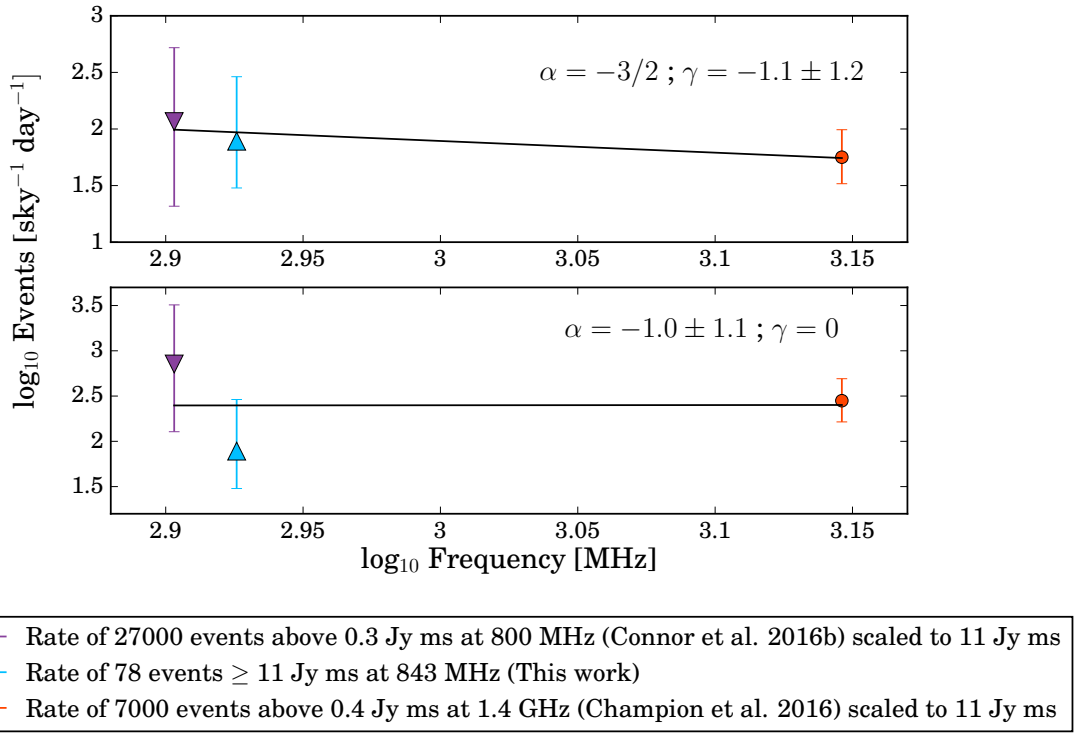

Figure 6.8 All-sky rates at the GBT and Parkes telescope, scaled to the measured UTMOST fluence limit of 11 Jy ms. For events to be detectable at UTMOST's present sensitivity, either 1) the spectral index should be steep or 2) the slope of $\log N$-$\log \mathcal{F}$ should be flat. Top panel: Constraint on γ assuming $\alpha = -3/2$. Bottom panel: Best fit for α assuming $\gamma = 0$.

to a minimum detectable fluence of $\mathcal{F}_{\rm lim} = 11$ Jy ms at boresight (see Equation 6.1). If we correct this rate for the measured primary beam dimensions being 10% larger (Bailes et al., submitted) than adopted in Caleb et al. (2016b) we get a rate of $\gtrsim 0.007(0.004)$ events d^{-1} which translates to being able to detect 1.3 events in 180 days on sky. This is in mild tension with our discovery of 3 events in the survey. We quantify this tension by calculating the probability of observing 3 or more events to be 14.3%, assuming Poisson statistics with a mean of 1.3. Note that the predicted rate at UTMOST takes into account pulse-width broadening in the current implementation of the backend (channel widths ~ 780 kHz) but does not account for possibly highly atypical scintillation properties along specific lines of sight to FRB events. The difference in the estimated and measured rates could be due to FRBs being brighter than expected at 843 MHz, and/or the slope of the source count distribution α, being shallower than the assumed value. Simultaneous broad-band detection of an FRB (e.g. Parkes + UTMOST) would help constrain the spectral index and resolve the question, if the pulse exhibits a power-law spectrum. In Caleb et al. (2016a), we measured $\alpha \approx -0.9 \pm 0.3$, from 9 FRBs discovered in the high latitude sub-survey of the HTRU survey at Parkes. This is consistent with the events occurring at cosmological distances in a ΛCDM Universe, in which the Euclidean value for α does not hold. Assuming a flat spectral index for FRBs ($\gamma = 0$), if we scale the rate at UTMOST from Equation 6.3, assuming $\alpha = -1.0$ for the slope of the log$N$-log$\mathcal{F}$ relation based on the best-fit from the bottom panel in Figure 6.8, we obtain a rate of $\gtrsim 2.1 \times 10^3$ events sky^{-1} d^{-1} at 1.4 GHz, consistent with the observed Parkes rate at the 2σ level (Champion et al., 2016).

6.4.2 Constraints on spectral and source count distribution indices

As discussed in the previous section, the observed FRB rate at UTMOST at 843 MHz can be brought to consistency with the rate found at 1.4 GHz at Parkes if we assume FRBs are flat spectrum sources on average, and that the log$N$-log$\mathcal{F}$ relation has slope $\alpha = -1.0$ (best-fit for α assuming $\gamma = 0$, in bottom panel of Figure 6.8). Alternatively, we can relax the flat spectrum assumption, and ascribe the higher than expected rate to FRBs being brighter at 843 MHz than at 1.4 GHz. Assuming the log$N$-log$\mathcal{F}$ relation has slope α and that the FRBs have a power law spectral energy distribution with index γ such that $S \propto \nu^{\gamma}$, we examine the following scenarios:

1. $\alpha = -3/2$: Based on the detection rates at the Parkes, GBT and UTMOST telescopes, we can constrain a spectral index for FRBs as shown in Figure 6.8. The rate of ~ 7000 events sky^{-1} d^{-1} at 1.4 GHz at Parkes, above a fluence limit of 0.4

Jy ms (Champion et al., 2016) scales to ~ 56 events sky^{-1} d^{-1} above UTMOST's fluence limit of 11 Jy ms, and assuming the spectral index to be flat ($\gamma = 0$) (see Section 6.4.1). Similarly, the rate of $\sim 2.7 \times 10^4$ events sky^{-1} d^{-1} at 800 MHz at the GBT, above a fluence threshold of 0.3 Jy ms (Connor et al., 2016a) and scaled to UTMOST's fluence threshold of 11 Jy ms is ~ 116 events sky^{-1} d^{-1}. Using these values we fit for the FRB spectra to be $\gamma = -1.1(1.2)$ (top panel of Figure 6.8). This is found to be consistent with the observed constraint in Keane et al. (2016) albeit for just one FRB assuming that FRBs exhibit power-law spectra.

2. $\gamma = 0$: A similar analysis can be done to constrain the index α of the integral source count distribution assuming a flat spectral index. We constrain a value of $\alpha = -1.0(1.1)$ for $\gamma = 0$ (bottom panel of Figure 6.8). This value of α gives scaled rates of ~ 270 events sky^{-1} d^{-1} at 1.4 GHz at Parkes and ~ 690 events sky^{-1} d^{-1} at 800 MHz at GBT.

Another possible scenario is that FRBs are giant pulses from pulsars (Cordes & Wasserman, 2016). The average observed spectral index for pulsars is $\gamma = -1.6$ (Bates et al., 2013, Jankowski et al., in submitted). If we assume this to be typical of FRBs, we fit a slope of $\alpha = -1.76$ for their log$N$-log$\mathcal{F}$ distribution. We note that the repeat FRB pulses from the Arecibo FRB 121102 exhibit a wide range of spectral indices ($\gamma \sim -10$ to $+14$; Spitler et al., 2016), similar to giant pulses from the Crab pulsar. For example giant pulses from the Crab pulsar exhibit spectral volatility in their broad range of spectral indices ($\gamma \sim -15$ to $+10$; Karuppusamy et al., 2010), therefore it will be difficult to estimate the mean of the spectral indices until the numbers are sufficiently high. From simultaneous observations of FRB 150418 with Parkes at 1.4 GHz and the Murchison Widefield Array (MWA) at 150 MHz (Keane et al., 2016), the non-detection at the MWA places a limit of $\gamma > -3.0$. Burke-Spolaor et al. (2016) estimate a weak constraint of $-7.6 < \gamma < 5.8$ based on the detection sensitivity of Champion et al. (2016) which is consistent with our estimated values. These constraints are only valid if the spectral energy distribution (SED) is an unbroken broadband power law and insignificantly affected by scintillation. This remains to be observationally proven. Future broadband instruments like CHIME (Bandura et al., 2014) should have high FRB discovery rates and spectral coverage to definitively test this. Using the method in Caleb et al. (2016b) we scale the observed rate at UTMOST for a boresight fluence of 11 Jy ms, to estimate the rates at CHIME and HIRAX (Newburgh et al., 2016) under a Euclidean Universe assumption. We expect CHIME to detect ~ 70 events beam^{-1} d^{-1} for $T_{\rm sys} = 50$ K, S/N = 10, $G = 1.38$ K Jy^{-1}, $n_{\rm p} = 2$ and FOV = 250 deg^2 (Connor et al., 2016b; Ng

et al., 2017). Similarly, we expect 350 events beam^{-1} d^{-1} at HIRAX for $T_{\rm sys}$ = 50 K, S/N = 10, G = 10.5 K Jy^{-1}, $n_{\rm p}$ = 2 and FOV = 56 deg^2 (Newburgh et al., 2016).

6.5 Conclusions

In this chapter we present the first interferometric detections of FRBs, found during 180 days on sky at UTMOST. The events are beyond the $\approx 10^4$ km near-field limit of the telescope, ruling out local (terrestrial) sources of interference as a possible origin. We demonstrate with pulsars that a repeating FRB seen at UTMOST has the potential to be localised to $\approx 15''$ diameter error circle, an exciting prospect for identifying the host.

An all-sky rate of $\mathcal{R}(\gtrsim 11$ Jy ms$) \gtrsim 0.78^{+1.24}_{-0.57} \times 10^2$ events sky^{-1} d^{-1} at 843 MHz is calculated from our 3 events, at the boresight fluence out to the half-power FOV. Based on the time spent on sky and the number of detections made, we measure a rate of $0.017^{+0.03}_{-0.01}$ events beam^{-1} d^{-1} at UTMOST, for the sensitivity achieved during the upgrade. The rates estimated by Caleb et al. (2016b) for the present sensitivity, is only 14.3% unlikely assuming Poisson statistics with a mean of 1.3. One possibility could be due to the log$N$-log$\mathcal{F}$ relation for events being flatter than for a Euclidean Universe, having a slope $\alpha \approx -1.0$, rather than $\alpha = -3/2$. In this case, searching for FRBs with a less sensitive, but wider field of view instrument, appears to be a competitive strategy (e.g. Vedantham et al., 2016). Alternatively, FRBs may simply be brighter at 843 MHz on average than at 1.4 GHz, implying a steeper spectral index for FRBs. Assuming a Euclidean Universe scaling, we find a best fit spectral index of $\gamma = -1.1(1.2)$. Our ongoing work, and the work of others at many other facilities, will settle these questions once sufficient numbers of FRBs are detected over a broad frequency range. Understanding the spectra and log$N$-log$\mathcal{F}$ distributions are vital in the quest to understand this enigmatic population.

7

Conclusions, recent results and future prospects

7.1 Summary of the key findings and questions answered by this thesis

This thesis outlined and discussed the high time resolution radio Universe, concentrating on single pulses from rotating radio transients (RRATs) and Fast Radio Bursts (FRBs). We reviewed transient radio sources (Chapter 1) and the instrumentation and single pulse processing pipelines of the UTMOST and Parkes radio telescopes (Chapter 2). Here we briefly summarise the findings of Chapters $3-6$.

Single pulse polarimetry

The last decade in radio astronomy has seen the discovery of two similar yet distinctly different sources of transient radio emission : Rotating radio transients (RRATs) and fast radio bursts (FRBs). RRATs can be defined as sources with an underlying periodicity that emit sporadic bursts of radiation, whereas FRBs are short, bright bursts of radio emission which have mostly been observed as singular events. The two classes of sources have similar properties in terms of their pulse widths, observed flux densities and cold-plasma dispersion sweeps. The primary distinguishing factors are their DMs and implied peak luminosities. The RRATs are a population with DMs between $9.2-786$ pc cm^{-3} which can fully be accounted for by the ISM in the Galaxy, and are consequently mainly seen in the Galactic plane. FRBs on the contrary have a close to isotropic distribution on the sky with most having been found at high latitude (see Figure 7.1) with observed DMs (currently in the range $267-2596\,\mathrm{pc\,cm^{-3}}$) well in excess of the Galactic contribution along that LOS. The FRBs have implied luminosities of $\sim 10^{13}$ Jy kpc^2 (assuming upper limits on redshifts from equation 1.16) compared to RRATs which have luminosities of 10 Jy kpc^2 (see Figure 1.1). This huge factor of 10^{12} Jy kpc^2 is currently the major challenge

for modelling the source of FRBs.

In the study in Chapter 3 we analysed the single pulses from RRATs to study their polarisation properties through Faraday rotation measurements in an attempt to better understand the application of the method to FRBs. Eighteen known RRATs with peak flux densities $S_{\rm min} > 100$ mJy were chosen and observed as part of the P864 project at the Parkes radio telescope. The RRAT J1819−1458 is the only one known to have a RM estimated using Faraday rotation studies of its integrated pulse (Karastergiou et al., 2009). In our study, we estimated the weighted average of the distribution of RMs obtained from single pulses of RRAT J1819−1458 to be 320(10) rad m^{-2} and the RM of the integrated pulse profile obtained by integrating all the single pulses together to be 327(3) rad m^{-2}. Both values are consistent with the published value of 330(30) rad m^{-2} in Karastergiou et al. (2009) with‘ much smaller uncertainties thus proving that single pulse RMs can be accurately determined. This study has resulted in the the first ever RM measurements for 18 published RRATs and a similar analysis has also been applied to several FRBs detected at the Parkes radio telescope (Petroff et al., 2015a; Keane et al., 2016; Petroff et al., 2017, Caleb et al., in prep).

Are FRBs cosmological?

An outstanding question in FRB astronomy is regarding their physical origin. We have performed Monte Carlo simulations of a cosmological population of FRBs in Chapter 4, based on assumptions consistent with observations of their energy distribution, their spatial density as a function of redshift and the properties of the interstellar and intergalactic media, for comparison with the 9 FRBs discovered in the Hilat sub-survey of the High Time Resolution Universe (HTRU) survey (Keith et al., 2010; Champion et al., 2016). We achieved acceptable fits to the data with the exception of the width distribution. Our model suggests that widths of the pulses are not due to a LOS dependent inhomogeneous IGM but may be due to interaction with the ISM of an intervening galaxy or an intracluster medium along the LOS. As the pulse widths probe completely different properties of FRBs and the IGM, this may prove more fruitful to understanding their origin as more FRBs are found. The observed slope α of the integral source count distribution of the 9 FRBs analysed is $\alpha = -0.9 \pm 0.3$ and is found to match the slope of the simulations, $\alpha = -0.8 \pm 0.3$. We conclude that the properties of the observed FRBs are consistent with those arising from sources at cosmological distances, with the important caveat that the pulse width distribution does not match our simulation results particularly well. Our conclusions are consistent with Katz (2016)

that the log$N$-log$S$ and N versus DM distributions are consistent (except for the anomalously bright Lorimer burst) with cosmological distances inferred from their DM in a simple approximation to standard cosmology

Statistical analyses indicate that at least 50 events at Parkes are required to distinguish between a constant comoving FRB source density, and a FRB source density that evolves with redshift like the cosmological star formation rate density.

FRB surveys with UTMOST at 843 MHz

We report the first radio interferometric search at 843 MHz for fast transients, particularly Fast Radio Bursts (FRBs) in Chapter 5. The recently recommissioned Swinburne University of Technology's digital backend for the Molonglo Observatory Synthesis Telescope array (the UTMOST) with its large collecting area (18,000 m^2) and wide instantaneous FOV ($\sim$ 8 deg^2) is expected to be an efficient tool to detect FRBs. As an interferometer, it will be capable of discerning whether the FRBs are probably a celestial population or $< 10^4$ km away. We show that UTMOST at its full design sensitivity might detect an event approximately every few days. We report on 2 preliminary FRB surveys at about 7% and 14% respectively of the array's final sensitivity. Several pulsars have been detected via single pulses and no FRBs were discovered with pulse widths (W), in the range 655.36 μs $< W <$ 41.9 ms and dispersion measures (DMs) in the range 100 $\leq$ DM $\leq$ 2000 pc cm^{-3}. This non-detection sets a 2σ upper limit of the sky rate of not more than 1000 events sky^{-1} day^{-1} at 843 MHz down to a flux limit of 11 Jy for 1 ms FRBs. We show that this limit is consistent with previous survey limits at 1.4 GHz and 145 MHz and set a lower limit on the mean spectral index of FRBs of $\alpha > -3.2$.

First interferometric detections of FRBs with UTMOST

In Chapter 6 we present a 159 day survey of the Southern sky conducted from November 2015 - November 2016, in which we discovered 3 FRBs at 843 MHz with the UTMOST array, as part of commissioning science during a major ongoing upgrade. The primary beam ($\sim$ 8 deg^2) is covered by 352 fan-beams (each $\sim 46''$ wide), spaced $41''$ apart and overlapping very close to the half-power points, each of which is searched for FRBs in real time with parameters similar to those listed in the previous section. Detections of FRBs with the UTMOST array places a lower limit on their distances of $\approx 10^4$ km (limit of the telescope near-field) strengthening the case for an astronomical origin. From the detected position, we present 3σ error ellipses of $15'' \times 6^\circ$ on the sky for the point of origin for

each FRB. Repeating FRBs at UTMOST or an FRB detected simultaneously (say) with the Parkes radio telescope and UTMOST, would allow a few arcsec localisation, thereby providing an excellent chance of identifying FRB host galaxies, if present. Up to 100 hours of follow-up for each FRB has been carried out with the UTMOST, with no repeat bursts seen. We measure an all-sky FRB rate of $\mathcal{R}(\gtrsim 11\ \mathrm{Jy\,ms}) \gtrsim 0.78^{+1.24}_{-0.57} \times 10^2$ events sky^{-1} d^{-1} at 843 MHz above at the 95% confidence level. Based on the time spent on sky and the number of detections made, we measure a rate of $0.017^{+0.03}_{-0.01}$ events beam^{-1} d^{-1} at UTMOST, for the sensitivity achieved during the upgrade. The rates estimated by Caleb et al. (2016b) for the present sensitivity, is only 14.3% unlikely assuming Poisson statistics with a mean of 1.3. We conclude that it can be explained by FRBs having a steeper spectral index and/or a flatter log$N$-log$\mathcal{F}$ distribution than expected for a Euclidean Universe.

7.2 Open questions in FRB astronomy and Future Directions

It is a decade since the discovery of FRBs and despite many developments, no consensus has emerged regarding their origin. Despite all the pulses having been broadly classified as "Fast Radio Bursts" and exhibiting certain characteristics in common with astronomical sources, not all FRBs are the same. For instance not all FRBs exhibit scatter tails nor do all FRBs (for which we have polarisation measurements) exhibit the same kind of polarisation. Also only one FRB is known to repeat, disfavouring cataclysmic progenitors (for at least one FRB). It is clear that in order to understand their nature, we need a sample size much larger than the presently known 26, with much better localisation (to a few arcseconds). A larger sample in turn requires a dedicated instrument with a larger FOV and better localisation requires the use of interferometers.

Outlined below are some of the present outstanding questions in FRB astronomy and possible approaches to answering them.

What is the sky distribution of FRBs?

A still unresolved characteristic of the FRB population is the possible dependence of detection rate on Galactic latitude (see Figure 7.1). This result is based on the dearth of FRB detections in the low- and mid-latitude components of the 1.4 GHz Parkes HTRU survey, despite the large fraction of survey time spent at these latitudes. The dearth of detections at low Galactic latitude despite correcting for effects such as scattering and sky temperature, disfavours a Galactic origin for these bursts. This is however far from established given the small number of FRBs known. The year 2015 broke the pattern of FRBs being regarded as one-off events and thus cataclysmic, when the FRB 121102 was

found to repeat often over a monitoring period of a few months (Spitler et al., 2016; Scholz et al., 2016), suggesting that at least a subset of FRBs have progenitors that can survive the energetic events causing them. A large number of FRBs together with their density on sky and intensity distribution will be useful for statistical studies of the population. Some of the currently unsolved questions regarding their sky distribution are,

- whether they have a Galactic latitude dependence (Macquart & Johnston, 2015) or are isotropically distributed over the sky?
- whether they are all produced by the same physical mechanisms and progenitors or if there are more than one class of FRB?
- whether they all repeat?
- whether the observed DM is dominated by the component due to the IGM or the material in the associated host galaxy?

The next generation telescopes like the Square Kilometer array (SKA; Macquart et al., 2015), Canadian Hydrogen Intensity Mapping Experiment (CHIME; Bandura et al., 2014), Deep Synoptic Array (DSA10; V. Ravi, private communication), MeerKAT[1], Australian SKA Pathfinder (ASKAP; Bannister et al., 2017) and UTMOST, with their large FOVs are well suited to answer whether FRBs are isotropically distributed or not.

Table 7.1 shows the predicted detection rates at various telescopes and upcoming surveys based on system temperature, number of polarisations, bandwidth, operating frequency and assumptions about the SED and the integral source count distribution of the FRB population. The other FRB search programmes in Table 7.1 are expected to come online in the next few years and most are aiming at FRB detection rates well in excess of what is currently possible at Parkes or UTMOST. CHIME and ASKAP are distinguished by spectacular FRB rates but poor localisation, so they will be particularly well equipped to constrain the FRB source count distribution and searches for FRBs with ASKAP are already underway (Bannister et al., 2017). MeerKAT has a similar FRB rate to Parkes and UTMOST at present but with much better localisation.

Do they emit at other wave-bands? How well can we localise them?

Of the 27 known FRBs (Lorimer et al., 2007; Thornton et al., 2013; Burke-Spolaor & Bannister, 2014; Petroff et al., 2015a; Ravi et al., 2015; Champion et al., 2016; Spitler et al., 2014; Keane et al., 2016; Spitler et al., 2016; Masui et al., 2015; Ravi et al., 2016;

[1] `http://www.trapum.org/`

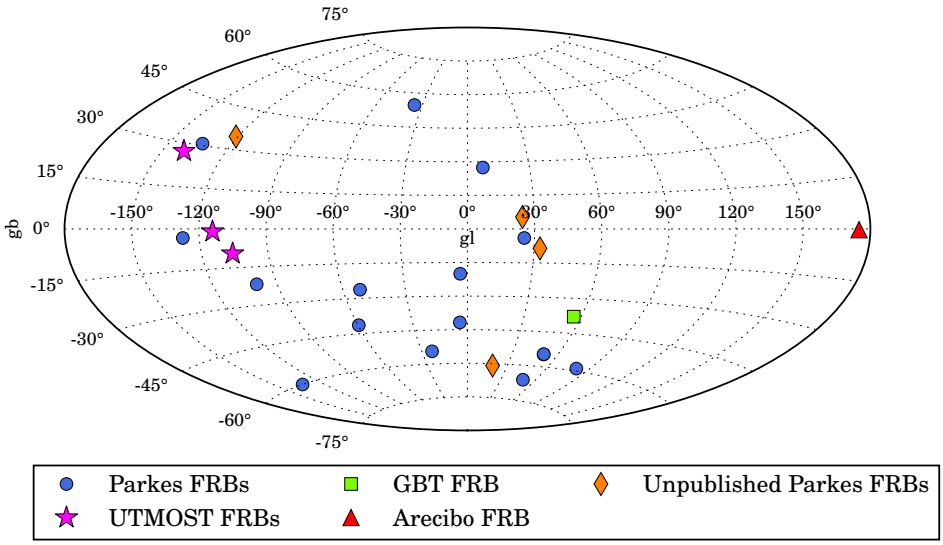

Figure 7.1 The sky distribution of all known FRBs to date, shown in Galactic coordinates. Filled circles mark the positions of the published FRBs detected at the Parkes telescope and diamonds mark the positions of the unpublished ones. The triangle represents FRB 121102 detected at the Arecibo telescope and the square represents FRB 110523 discovered at the GBT. Stars mark the positions of the UTMOST FRBs. It should be noted that there are large biases in this distribution due to very different sky coverages and survey depths. There is still an underlying Galactic latitude dependence in the FRB distribution even with the inclusion of the unpublished Parkes FRBs.

Table 7.1 Expected FRB detection rates at various upcoming telescopes. The minimum detectable fluence at a telescope is computed for a 10σ, 1-ms wide pulse given its specifications. The rate is estimated for a $\log N$-$\log \mathcal{F}$ index of $\alpha = -1.0$ (i.e.) $N > \mathcal{F}^{-1}$. All the estimated rates have been scaled to the present Parkes rate of 1 per 12 days. The first three rows are currently operating experiments.

Survey Telescope	Gain (K Jy^{-1})	$T_{\rm sys}$ (K)	$\mathcal{F}_{\rm min}/\sqrt{W}$ (Jy ms)	Area (deg^2)	Days event^{-1}
Parkes	0.65	23.0	0.43	0.55	12
UTMOST	3.00	400.0	10.54	8.00	20
Arecibo	10.4	30.0	0.04	0.022	26
DSA10	0.01	60.0	64.50	6.25	160
DSA256	1.00	60.0	0.84	6.25	2
CHIME	1.60	50.0	0.35	250.00	0.02
MeerKAT	0.30	18.0	0.46	1.00	7
ASKAP	0.03	65.0	27.97	30.00	14

Petroff et al., 2017; Caleb et al., 2017; Bannister et al., 2017, Bhandari et al., submitted) only 8 have been detected in real time so far (Petroff et al., 2015a; Ravi et al., 2015; Keane et al., 2016; Ravi et al., 2016; Petroff et al., 2017, Bhandari et al., in prep) and this has allowed prompt follow-up with other telescopes. With the larger sample of FRBs expected with next generation telescopes (see Section 7.2) we can create opportunities for follow-up with existing radio telescopes, high-energy and gravitational wave observatories for follow-up at other wave-bands. We can expect breakthroughs in our understanding of FRBs through this approach as was demonstrated in the case of GRBs and in the recent FRB 121102 using Arecibo, the Very Large Array (VLA) and the European VLBI Network (EVN) (Chatterjee et al., 2017; Tendulkar et al., 2017; Marcote et al., 2017). This FRB is believed to be co-located with a low-luminosity AGN or a neutron star powering its parent supernova remnant in a low-metallicity dwarf galaxy at $z = 0.19273 \pm 0.0008$ (Tendulkar et al., 2017). However the exact nature of the progenitor remains unknown. This association of an FRB with a dwarf galaxy will influence future follow-up strategies. An FRB localised to a host galaxy and redshift can potentially aid in measuring the missing baryonic content of the Universe along the LOS in the low-z Universe (McQuinn, 2014). A detection of a counterpart at another wavelength would not only provide valuable insights regarding their progenitors but also about possible emission mechanisms. Unfortunately the type of multi-wavelength detections expected of FRBs is largely uncertain since not all FRBs have been seen to repeat. Commensal observing and shadowing offer great potential for the identification of an FRB progenitor. The SUPERB project at the Parkes telescope uses the MWA telescope ($\sim$ 200 MHz) and the Giant Metrewave Radio Telescope (GMRT; $\sim$ 600 MHz) for shadowing observations. In the case of FRB 150418, no statistically significant counterpart was identified during simultaneous observations with the MWA (Keane et al., 2016). The non-detection of the burst at the MWA telescope at the time of occurrence resulted in a spectral index constraint of $\gamma > -3.0$.

Observations with multi-element interferometers or phased array feeds (PAFs) are the future of FRB localisations. We can expect localisation to a positional accuracy of a few arcsec as new FRBs are found in the next few years, with next generation interferometers coming online. Already, the adjacent fan-beam localisations of the FRBs with the present UTMOST system yields 3σ ellipses of $15'' \times 6^{\circ}$ on the sky, with a HA dependent orientation. This localisation area of ~ 56 arcmin^2 at UTMOST is ~ 3 times better than that of Parkes ($\sim$ 160 arcmin^2) and we are able to well constrain the measured properties in the direction of the semi-minor axis. There is still however, a large uncertainty in the direction of the semi-major-axis. The UTMOST-2D project (PI:

Adam Deller) is a planned upgrade to UTMOST in 2017 to refurbish the N-S arm of the telescope to provide better spatial localisation. With the upgrade and inclusion of the N-S arm, FRBs discovered at UTMOST can be constrained to a few arcseconds localisation thus enabling unambiguous association with a host galaxy for which redshifts and host properties can be obtained in the optical and infrared. The DSA10 prototype array currently being built in the Owens Valley in California is a 'large N - small D' project consisting of ten 5-m commercial off-the-shelf single dishes operating between 1 - 2 GHz. The primary science goal of the project is to localise FRBs to $< 3''$ by post processing buffered raw voltages (V.Ravi, private communication). The TRAPUM project for fast transients at MeerKAT is expected to localise FRBs to $\sim$ arcsec resolution (Obrocka et al., 2015).

What is their integral source count distribution?

The integral source count distribution of FRBs can be described as $N(> \mathcal{F}_{\rm min}) = \mathcal{F}_{\rm min}^{\alpha}$ where $\alpha = -3/2$ for standard-candle-like events populated in a Euclidean Universe. From 9 FRBs discovered in the Hilat sub-survey of the High Time Resolution Universe survey at Parkes, the index has been estimated to be $\alpha = -0.9 \pm 0.3$ (see Chapter 1; Caleb et al., 2016a). This is consistent with the events occurring at cosmological distances in a ΛCDM Universe, in which the Euclidean value for α does not hold. At a redshift of $z \sim 0.7$ (estimated from equation 1.16 assuming negligible contributions host galaxies to the observed DM), typical of FRBs found to date, standard candles yield a relation with a slope of $\alpha \sim -1$ as seen observationally. For this value of α and the assumption of a flat FRB spectrum, if we scale the all-sky rate of $\mathcal{R}(\gtrsim 11\,{\rm Jy\,ms}) \sim 78$ events sky^{-1} day^{-1} at UTMOST at 843 MHz to 1.4 GHz at Parkes, we obtain a rate of $\gtrsim 2.1 \times 10^3$ events sky^{-1} d^{-1} at 1.4 GHz, consistent with the observed Parkes rate at the 2σ level Champion et al. (2016). Under these assumptions, the UTMOST FRB discoveries support the hypothesis and measurement that the log$N$-log$\mathcal{F}$ relation for FRBs is flatter than Euclidean, and also the search for FRBs with telescopes having large FOVs (Vedantham et al., 2016). This is particularly favourable for the upcoming next generation telescopes. These telescopes with their high discovery rates given in Table 7.1 and high duty cycles can be expected to resolve this question of source count distribution.

Can we probe cosmic magnetism?

If FRBs are indeed identified to be cosmological, their polarisation properties could provide

the first measurements of the extragalactic magnetic fields along the LOS and also insight into the magnetic field associated with the source. Polarimetric information has only been measured in 7 FRBs of which only 4 are published. For FRB 140514 observed at Parkes (Petroff et al., 2015a), a significant circularly polarized component was observed. For FRB 110523 observed at the GBT (Masui et al., 2015), the signal was significantly linearly polarized with a large rotation measure of $-186.1 \pm 1.4\,\mathrm{rad\,m^{-2}}$. FRB 150807 discovered at Parkes (Ravi et al., 2016), was found to be 100% linearly polarised with an RM of 12.0 ± 7 rad m^{-2}. However, the measured RM of the FRB is dominated by the same contributions seen towards the slightly o set pulsar J2241−5236 in the FOV during the observation. The FRB 160102 discovered as part of the SUPERB collaboration with a DM of $2593.7 \pm 1.0\,\mathrm{pc\,cm^{-3}}$, was found to be 100 percent polarised with a linear polarisation fraction of 84 ± 14 percent and a circular fraction of 30 ± 11 percent (see Figure 7.3). An extensive RM search was performed $|\mathrm{RM_{max}}| = 1.18 \times 10^5$ rad m^{-2} and the burst was found to have an RM $= -220.5 \pm 6.4$ rad m^{-2} (Caleb et al., in prep) implying a line-of-sight magnetic field strength of $B \gtrsim 0.1\,\mu$G. The observed B is a lower limit due possible LOS magnetic field reversals due to intervening components like filaments or galaxies.

This FRB is similar to FRB 110523 discovered at the GBT in terms of its RM value and average position angle. The foreground contribution to FRB 160102 was estimated in three different ways using RM maps, nearby extragalactic polarised sources and from RMs of pulsars in our Galaxy. In the first method, the RM of the closest known NRAO VLA Sky Survey (NVSS; Taylor et al., 2009) source NVSS J224509−301243, to the position of the FRB was found to be $+28.7 \pm 6.3$ rad m^{-2}. In the second method, the RM of the closest known pulsar J2155−3118 from PSRCAT[2] is found to be $+21 \pm 3$ rad m^{-2}. In the third method, the contribution from the smoothed Galactic foreground Oppermann et al. (2015) maps was computed to be $+22 \pm 6$ rad m^{-2}. The foreground contributions from all three methods are seen to be consistent with a weighted average of +24.6 rad m^{-2}. The same map shows that the IGM can contribute $\lesssim \pm 7$ rad m^{-2} along a typical LOS. From Equation 1.35 we can estimate the intrinsic RM contribution. Given a weighted average of +24.6 rad m^{-2} from the three methods detailed above for the Galactic foreground contribution and assuming a value of +7 rad m^{-2} for the IGM contribution, we expect the source to have an intrinsic RM of −252.1 rad m^{-2} under the assumption that it is extragalactic to a few 100 Mpc (i.e.) not taking into account the redshifting of frequency.

This FRB could either be due to a young pulsar associated with its parent supernova remnant or due to a circumnuclear magnetar, as discussed in Section 1.4.1. Both models

[2] `http://www.atnf.csiro.au/people/pulsar/psrcat/`

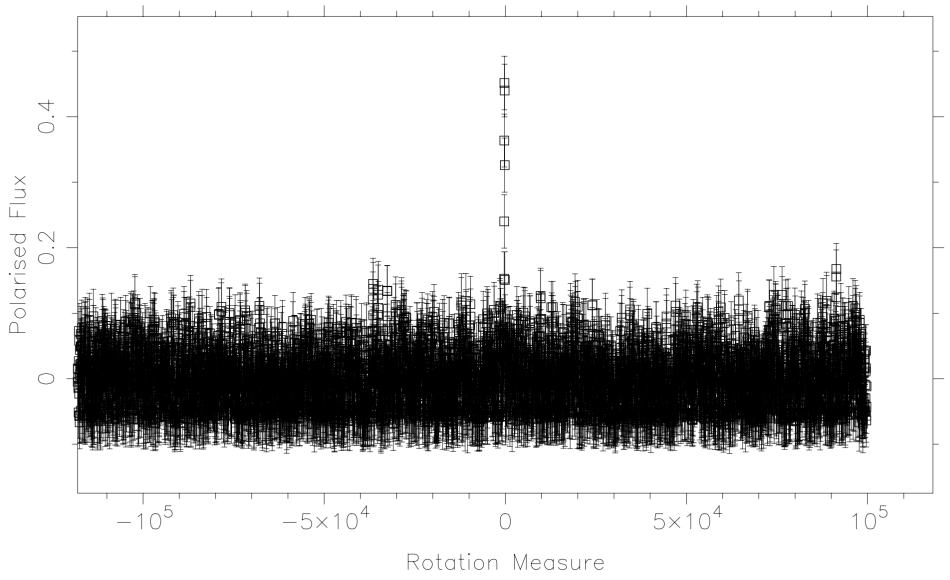

(a)

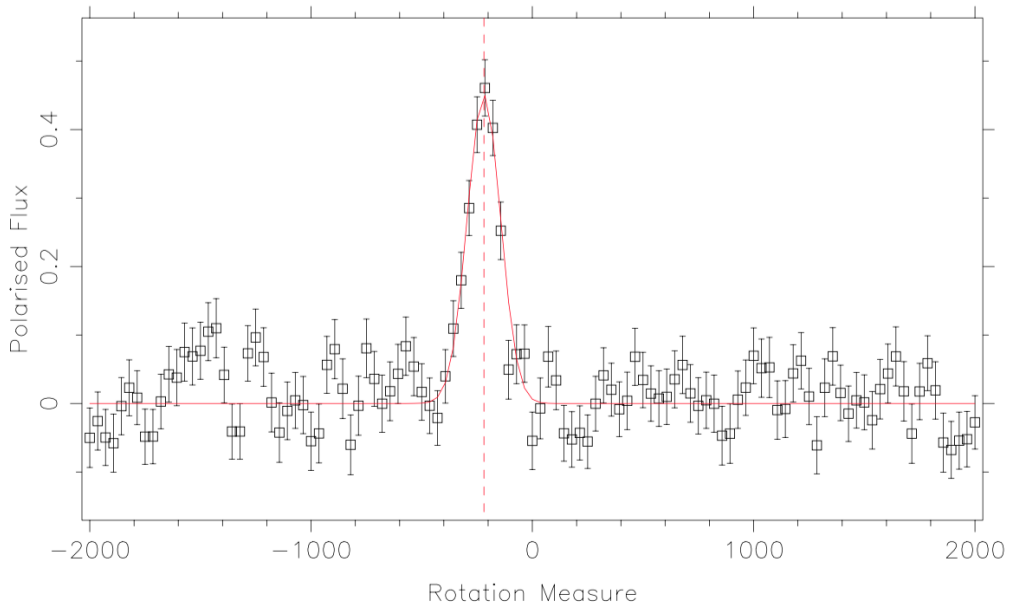

(b)

Figure 7.2 Brute force search for RM using RMFIT by searching for a peak in the linearly polarised flux. Panel (a): Trial RMs in the range $|\mathrm{RM_{max}}| = 1.18 \times 10^5$ rad m^{-2} in steps of 1 rad m^{-2} were used and a peak in the linearly polarised intensity is seen at RM $= -220.5 \pm 6.4$ rad m^{-2}. Panel (b): Zoomed in version of Panel (a) for trial RMs in the range -2000 rad m^{-2} to +2000 rad m^{-2} in steps of 20 rad m^{-2}.

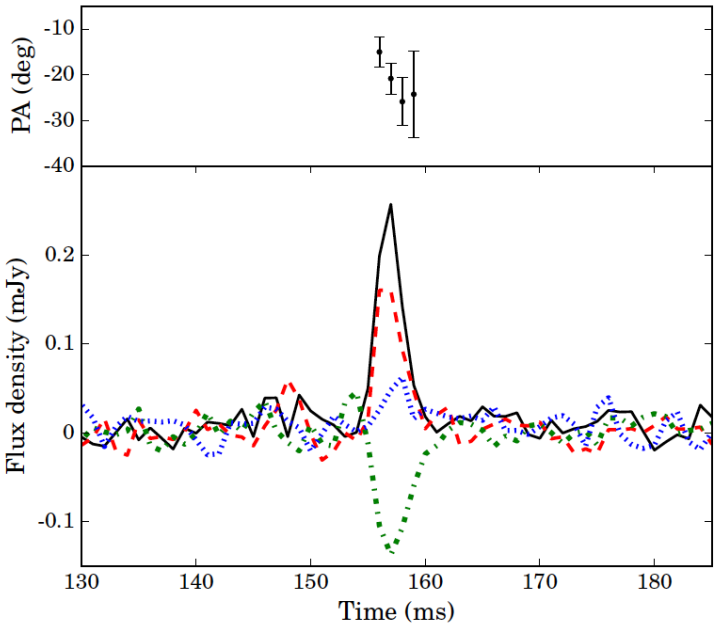

Figure 7.3 Polarisation profile of FRB160102. Top panel: Polarisation position angle (Ψ) of the electric field vector. Bottom panel: The black, red, green and blue curves represent the total intensity and Stokes Q, U and V. The pulse has a linear polarisation fraction of 84 ± 14 percent and a circular fraction of 30 ± 11 percent (Caleb et al., in prep).

can account for the high DM, observed RM and PA (Pen & Connor, 2015; Piro, 2016; Lyutikov et al., 2016). Since the observed RM and PA are similar to the FRB 110523 discovered at the GBT, we might assume FRB 160102 to be from a similar progenitor, but at higher z and with a higher luminosity (see Figure 7.5). FRB 110523 has an observed RM and DM of $-186.1 \pm 1.4\,\mathrm{rad\,m^{-2}}$ and 623.30(5) $\mathrm{pc\,cm^{-3}}$ respectively. Under the assumption that the two FRBs are produced by similar progenitors, for FRB 160102, 623.30 $\mathrm{pc\,cm^{-3}}$ of DM can be assumed to account for $\sim$200 rad $\mathrm{m^{-2}}$ of RM. According to Equation 1.15, this implies that $\mathrm{DM_{MW}} + \mathrm{DM_{IGM}} = 1970.4\,\mathrm{pc\,cm^{-3}}$. Using the NE2001 model by Cordes & Lazio (2002), the $\mathrm{DM_{MW}}$ is estimated to be 34.4 $\mathrm{pc\,cm^{-3}}$ which gives $\mathrm{DM_{IGM}} = 1936\,\mathrm{pc\,cm^{-3}}$. This value of $\mathrm{DM_{IGM}}$ translates to $z = 1.6$ using Equation 1.16. Taking into account the redshifting of frequency, the DM and RM will be higher than the observed values, by $(1+z)$ and $(1+z)^2$ respectively. The DM and RM are therefore 6749.6 $\mathrm{pc\,cm^{-3}}$ and -1656.8 $\mathrm{rad\,m^{-2}}$ respectively.

Figure 7.4 shows a comparison of the RM of FRB160102 and it's corresponding inferred upper limit on redshift to the distribution of residual rotation measures (RRM; the difference between the observed RM and the Galactic RM contribution) of extragalactic radio galaxies and quasars as a function of their measured redshifts from

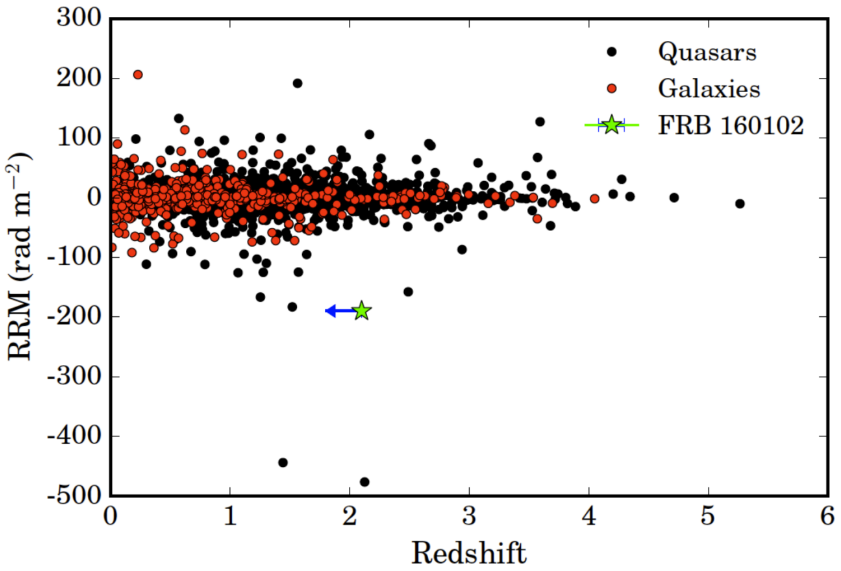

Figure 7.4 Comparison between extragalactic residual RMs and the RM of FRB160102 as a function of redshift. The Galactic contributions to the extragalactic RMs have been subtracted from the observed RMs. The FRB redshift is an upper limit calculated from the empirical scaling relation in equation 1.16.

Hammond et al. (2012). The FRB RM could maybe be similar to the RMs of quasars with $|\mathrm{RRM}| > 100$ rad m^{-2}. In case of the FRB, a DM will accompany any RM and there may be multiple gas components which will contribute to both DM and RM with varying proportions. Hence we cannot infer anything concrete from this comparison. Analyses of this FRB is still ongoing and will be presented in Caleb et al., in prep.

Further examples of FRB polarimetry are urgently required to compare with expectations for known source classes such as magnetars and pulsars. For example significant linear polarization is consistent with observations of known pulsars. A large sample of FRB RMs obtained through full polarisation observations with upcoming telescopes and the corresponding redshifts via photometric and spectroscopic optical surveys could enable us to map the progression of the magnetic field of the Universe out to $z \sim 3$ (Gaensler, 2007) if FRBs are cosmological and have magnetic fields dominated by the IGM.

The relatively high all-sky rate of FRBs poses constraints on possible progenitor models. Since their discovery, several models have been proposed ranging from flare stars (Loeb et al., 2014), binary white dwarf mergers (Kashiyama et al., 2013), hyperflares from soft gamma-ray repeaters (Popov & Postnov, 2010; Lyubarsky, 2014), and radio emission from pulsars (Cordes & Wasserman, 2016) to the more exotic 'Blitzars' (Falcke

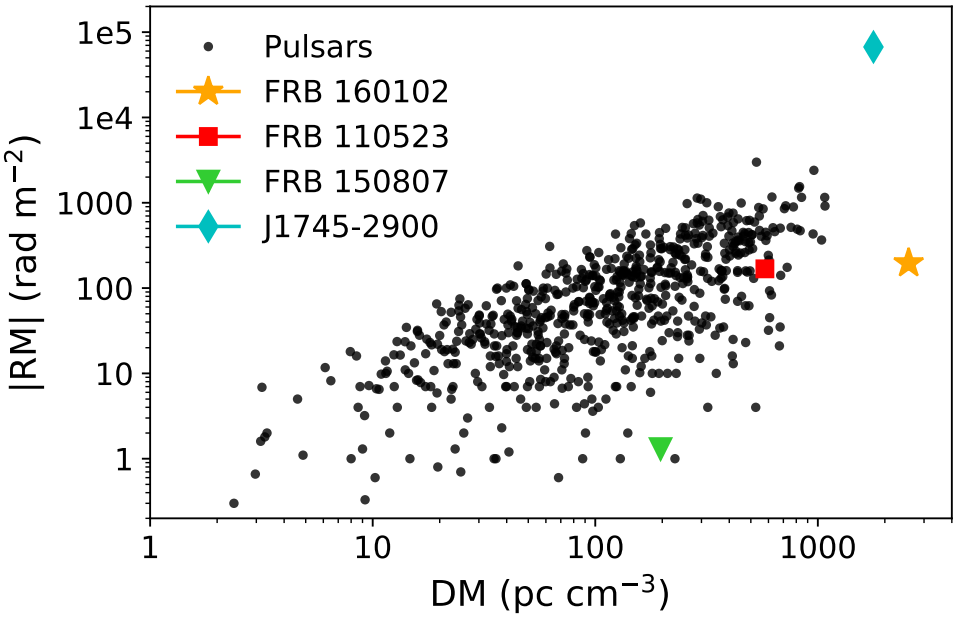

Figure 7.5 Comparison between the RMs and DMs of pulsars, FRBs and magnetar J1745−2900. The square, triangle, star and diamond represent FRBs 110523, 150807, 160102 and the Galactic centre magnetar J1745−2900 respectively. The Galactic contributions have been subtracted from the total observed DMs of the FRBs and plotted against the difference between the observed RM and the foreground contribution to it. FRB 160102 is seen to be similar to FRB 110523 in RM but with higher DM.

& Rezzolla, 2014), caused by the collapse of a supramassive NS into a black hole. Most theories support cataclysmic events with exceptions of a few which cater to repeating FRBs. It is possible that the lack of repetition of pulses for the FRB discoveries at the Parkes radio telescope is merely due to limited sensitivity and follow-up time, and that all FRBs have a common origin (Spitler et al., 2016; Scholz et al., 2016). The present leading theories for FRBs are hyperflares from soft gamma-ray repeaters and giant pulses from pulsars both of which have been discussed in Section 1.4.1. Both theories are presently able to account for properties such as the large DMs, RMs and PAs and can be consistent with timescales for repetition in the known FRBs (Connor et al., 2016b; Cordes & Wasserman, 2016). Importantly, FRBs would be not more than a few hundred Mpc away in these models.

Given the relatively high all-sky rate of FRBs and the possibility of a flat source count distribution, telescopes with large FOVs are ideal for searches. The key to understanding these enigmatic bursts lies in localisation, preferably with commensal observing with telescopes at other wavelengths. Presently, human intervention is required between the detection of an event and triggering other telescopes for follow-up at the UTMOST. However this can lead to an unsatisfactory time lag between detection and trigger. Machine learning is one potential method to robustly excise RFI and identify and isolate FRB candidate events. It can be used as a powerful tool to search for FRBs as is currently being implemented at UTMOST by the UTMOST collaboration. Various types of custom designed experiments can be performed once we understand the FRB population, given the large discovery rates expected from future and present telescopes. We can expect the next decade to answer some if not all the open questions in FRB astronomy.

Bibliography

Amy, S. W., Large, M. I., & Vaughan, A. E. 1989, Proceedings of the Astronomical Society of Australia, 8, 172

Armstrong, J. W., Rickett, B. J., & Spangler, S. R. 1995, ApJ, 443, 209

Baade, W., & Zwicky, F. 1934, Proceedings of the National Academy of Science, 20, 254

Bai, T., & Sturrock, P. A. 1989, ARA&A, 27, 421

Bandura, K., Addison, G. E., Amiri, M., et al. 2014, in Society of Photo-Optical Instrumentation Engineers (SPIE) Conference Series, Vol. 9145, Society of Photo-Optical Instrumentation Engineers (SPIE) Conference Series, 22

Bannister, K. W., Shannon, R. M., Macquart, J.-P., et al. 2017, ApJ, 841, L12

Barsdell, B. R. 2012, PhD thesis, Swinburne University of Technology

Barthelmy, S. D., D'Elia, V., Gehrels, N., et al. 2016, The Astronomer's Telegram, 8831

Bastian, T. S., Benz, A. O., & Gary, D. E. 1998, ARA&A, 36, 131

Bates, S. D., Lorimer, D. R., & Verbiest, J. P. W. 2013, MNRAS, 431, 1352

Beck, R., & Wielebinski, R. 2013, Magnetic Fields in Galaxies, ed. T. D. Oswalt & G. Gilmore, 641

Bhat, N. D. R., Cordes, J. M., Camilo, F., Nice, D. J., & Lorimer, D. R. 2004, ApJ, 605, 759

Blaauw, A. 1985, in Astrophysics and Space Science Library, Vol. 120, Birth and Evolution of Massive Stars and Stellar Groups, ed. W. Boland & H. van Woerden, 211–223

Bock, D. C.-J., Large, M. I., & Sadler, E. M. 1999, AJ, 117, 1578

Burke, B. F., & Graham-Smith, F. 2014, An Introduction to Radio Astronomy

Burke-Spolaor, S., & Bailes, M. 2010, MNRAS, 402, 855

Burke-Spolaor, S., Bailes, M., Ekers, R., Macquart, J.-P., & Crawford, III, F. 2011, ApJ, 727, 18

Burke-Spolaor, S., & Bannister, K. W. 2014, ApJ, 792, 19

Burke-Spolaor, S., Trott, C. M., Brisken, W. F., et al. 2016, ApJ, 826, 223

Caleb, M., Flynn, C., Bailes, M., et al. 2016a, MNRAS, 458, 708

Caleb, M., Flynn, C., Bailes, M., et al. 2016b, MNRAS, 458, 718

Caleb, M., Flynn, C., Bailes, M., et al. 2017, MNRAS, 468, 3746

Camilo, F., Ransom, S. M., Halpern, J. P., et al. 2006, Nature, 442, 892

Campbell-Wilson, D., Davidson, G., & Large, M. I. 1997, PASA, 14, 265

Cane, H. V., & Reames, D. V. 1988, ApJ, 325, 895

Champion, D. J., Petroff, E., Kramer, M., et al. 2016, MNRAS, 460, L30

Chandra, P., & Frail, D. A. 2012, ApJ, 746, 156

Chatterjee, S., Law, C. J., Wharton, R. S., et al. 2017, ArXiv e-prints

Coenen, T., van Leeuwen, J., Hessels, J. W. T., et al. 2014, A&A, 570, A60

Connor, L., Lin, H.-H., Masui, K., et al. 2016a, MNRAS, 460, 1054

Connor, L., Sievers, J., & Pen, U.-L. 2016b, MNRAS, 458, L19

Cordes, J. M., & Lazio, T. J. W. 2002, ArXiv Astrophysics e-prints

Cordes, J. M., & McLaughlin, M. A. 2003, ApJ, 596, 1142

Cordes, J. M., Romani, R. W., & Lundgren, S. C. 1993, Nature, 362, 133

Cordes, J. M., & Wasserman, I. 2016, MNRAS, 457, 232

DeLaunay, J. J., Fox, D. B., Murase, K., et al. 2016, ApJ, 832, L1

Dicke, R. H., & Beringer, R. 1946, ApJ, 103, 375

Djorgovski, S., & King, I. R. 1984, ApJ, 277, L49

Eatough, R. P., Falcke, H., Karuppusamy, R., et al. 2013, Nature, 501, 391

Ergun, R. E., Carlson, C. W., McFadden, J. P., et al. 1998, Geophys. Res. Lett., 25, 2061

Esamdin, A., Lyne, A. G., Graham-Smith, F., et al. 2005, MNRAS, 356, 59

Falcke, H., & Rezzolla, L. 2014, A&A, 562, A137

Fukugita, M., & Peebles, P. J. E. 2004, ApJ, 616, 643

Fuller, J., & Ott, C. D. 2015, MNRAS, 450, L71

Gaensler, B. 2007, in From Planets to Dark Energy: the Modern Radio Universe, 66

Gehrels, N. 1986, ApJ, 303, 336

Gold, T. 1968, Nature, 218, 731

Goldreich, P., & Julian, W. H. 1969, ApJ, 157, 869

Gould, D. M., & Lyne, A. G. 1998, MNRAS, 301, 235

Green, A., Madsen, G. J., Campbell-Wilson, D., et al. 2012, in Resolving The Sky - Radio Interferometry: Past, Present and Future

Grégoire, T., & Knödlseder, J. 2013, A&A, 554, A62

Gurnett, D. A. 1974, J. Geophys. Res., 79, 4227

Hallinan, G., Antonova, A., Doyle, J. G., et al. 2008, ApJ, 684, 644

Hamilton, P. A., McCulloch, P. M., Manchester, R. N., Ables, J. G., & Komesaroff, M. M. 1977, Nature, 265, 224

Hammond, A. M., Robishaw, T., & Gaensler, B. M. 2012, ArXiv e-prints

Han, J. L., Manchester, R. N., Lyne, A. G., Qiao, G. J., & van Straten, W. 2006, ApJ, 642, 868

Hankins, T. H., & Eilek, J. A. 2007, ApJ, 670, 693

Hankins, T. H., & Rickett, B. J. 1975, in Methods in Computational Physics. Volume 14 - Radio astronomy, ed. B. Alder, S. Fernbach, & M. Rotenberg, Vol. 14, 55–129

Haslam, C. G. T., Salter, C. J., Stoffel, H., & Wilson, W. E. 1982, A&AS, 47, 1

Hassall, T. E., Keane, E. F., & Fender, R. P. 2013, MNRAS, 436, 371

Heiles, C., Perillat, P., Nolan, M., et al. 2001, PASP, 113, 1274

Hewish, A., Bell, S. J., Pilkington, J. D. H., Scott, P. F., & Collins, R. A. 1968, Nature, 217, 709

Hopkins, A. M., & Beacom, J. F. 2006, ApJ, 651, 142

Hotan, A. W., van Straten, W., & Manchester, R. N. 2004, PASA, 21, 302

Inoue, S. 2004, MNRAS, 348, 999

Ioka, K. 2003, ApJ, 598, L79

Jackson, J. D. 1962, Classical Electrodynamics

Johnston-Hollitt, M., Govoni, F., Beck, R., et al. 2015, Advancing Astrophysics with the Square Kilometre Array (AASKA14), 92

Kaiser, M. L., & Alexander, J. K. 1976, Geophys. Res. Lett., 3, 37

Karastergiou, A., Hotan, A. W., van Straten, W., McLaughlin, M. A., & Ord, S. M. 2009, MNRAS, 396, L95

Karastergiou, A., Chennamangalam, J., Armour, W., et al. 2015, MNRAS, 452, 1254

Karuppusamy, R., Stappers, B. W., & van Straten, W. 2010, A&A, 515, A36

Kashiyama, K., Ioka, K., & Mesaros, P. 2013, ApJ, 776, L39

Kaspi, V. M., & Helfand, D. J. 2002, in Astronomical Society of the Pacific Conference Series, Vol. 271, Neutron Stars in Supernova Remnants, ed. P. O. Slane & B. M. Gaensler, 3

Kaspi, V. M., Roberts, M. S. E., & Harding, A. K. 2006, Isolated neutron stars, ed. W. H. G. Lewin & M. van der Klis, 279–339

Katz, J. I. 2014, Phys. Rev. D, 89, 103009

Katz, J. I. 2016, ApJ, 818, 19

Keane, E. F. 2015, ArXiv e-prints

Keane, E. F. 2016, MNRAS, 459, 1360

Keane, E. F., & Kramer, M. 2008, MNRAS, 391, 2009

Keane, E. F., Ludovici, D. A., Eatough, R. P., et al. 2010, MNRAS, 401, 1057

Keane, E. F., & McLaughlin, M. A. 2011, Bulletin of the Astronomical Society of India, 39, 333

Keane, E. F., & Petroff, E. 2015, MNRAS, 447, 2852

Keane, E. F., Stappers, B. W., Kramer, M., & Lyne, A. G. 2012, MNRAS, 425, L71

Keane, E. F., Johnston, S., Bhandari, S., et al. 2016, Nature, 530, 453

Keane, E. F., Barr, E. D., Jameson, A., et al. 2017, ArXiv e-prints

Keith, M. J., Jameson, A., van Straten, W., et al. 2010, MNRAS, 409, 619

Kellermann, K. I., & Moran, J. M. 2001, ARA&A, 39, 457

Kramer, M., Lyne, A. G., O'Brien, J. T., Jordan, C. A., & Lorimer, D. R. 2006a, Science, 312, 549

Kramer, M., Stairs, I. H., Manchester, R. N., et al. 2006b, Science, 314, 97

Kulkarni, S. R., Ofek, E. O., Neill, J. D., Zheng, Z., & Juric, M. 2014, ApJ, 797, 70

Kulkarni, S. R., Frail, D. A., Wieringa, M. H., et al. 1998, Nature, 395, 663

LaBelle, J., Treumann, R. A., Yoon, P. H., & Karlicky, M. 2003, ApJ, 593, 1195

Large, M. I., Vaughan, A. E., & Wielebinski, R. 1968, Nature, 220, 753

Lattimer, J. M., & Prakash, M. 2004, Science, 304, 536

Lattimer, J. M., & Prakash, M. 2007, Phys. Rep., 442, 109

Law, C. J., Bower, G. C., Burke-Spolaor, S., et al. 2015, ApJ, 807, 16

Li, J., Spitkovsky, A., & Tchekhovskoy, A. 2012, ApJ, 746, 60

Loeb, A., Shvartzvald, Y., & Maoz, D. 2014, MNRAS, 439, L46

Lorimer, D. R., Bailes, M., McLaughlin, M. A., Narkevic, D. J., & Crawford, F. 2007, Science, 318, 777

Lorimer, D. R., Karastergiou, A., McLaughlin, M. A., & Johnston, S. 2013, MNRAS, 436, L5

Lorimer, D. R., & Kramer, M. 2012, Handbook of Pulsar Astronomy

Luan, J., & Goldreich, P. 2014, ApJ, 785, L26

Lyne, A. G., McLaughlin, M. A., Keane, E. F., et al. 2009, MNRAS, 400, 1439

Lyne, A. G., & Smith, F. G. 1989, MNRAS, 237, 533

Lyubarsky, Y. 2014, MNRAS, 442, L9

Lyutikov, M., Burzawa, L., & Popov, S. B. 2016, MNRAS, 462, 941

Macquart, J.-P., & Johnston, S. 2015, MNRAS, 451, 3278

Macquart, J.-P., & Koay, J. Y. 2013, ApJ, 776, 125

Macquart, J. P., Keane, E., Grainge, K., et al. 2015, Advancing Astrophysics with the Square Kilometre Array (AASKA14), 55

Manchester, R. N., Lyne, A. G., Taylor, J. H., et al. 1978, MNRAS, 185, 409

Manchester, R. N., Lyne, A. G., Camilo, F., et al. 2001, MNRAS, 328, 17

Marcote, B., Paragi, Z., Hessels, J. W. T., et al. 2017, ApJ, 834, L8

Masui, K., Lin, H.-H., Sievers, J., et al. 2015, Nature, 528, 523

McLaughlin, M. A., Lyne, A. G., Lorimer, D. R., et al. 2006, Nature, 439, 817

McQuinn, M. 2014, ApJ, 780, L33

Melrose, D. B. 1980, Sol. Phys., 67, 357

Melrose, D. B. 1992, Philosophical Transactions of the Royal Society of London Series A, 341, 105

Miller, J., McLaughlin, M., Rea, N., et al. 2011, in American Institute of Physics Conference Series, Vol. 1357, American Institute of Physics Conference Series, ed. M. Burgay, N. D'Amico, P. Esposito, A. Pellizzoni, & A. Possenti, 161–164

Mitra, D., Melikidze, G., & Gil, J. 2015, in Astronomical Society of India Conference Series, Vol. 12, Astronomical Society of India Conference Series

Mottez, F., & Zarka, P. 2014, A&A, 569, A86

Mutel, R. L., Gurnett, D. A., & Huff, R. L. 2000, in ESA Special Publication, Vol. 449, Cluster-II Workshop Multiscale / Multipoint Plasma Measurements, ed. R. A. Harris, 197

Netzer, H. 2015, ARA&A, 53, 365

Newburgh, L. B., Bandura, K., Bucher, M. A., et al. 2016, in Proc. SPIE, Vol. 9906, Ground-based and Airborne Telescopes VI, 99065X

Ng, C., Vanderlinde, K., Paradise, A., et al. 2017, ArXiv e-prints

Nita, G. M., & Gary, D. E. 2010a, PASP, 122, 595

Nita, G. M., & Gary, D. E. 2010b, MNRAS, 406, L60

Noutsos, A., Johnston, S., Kramer, M., & Karastergiou, A. 2008, MNRAS, 386, 1881

Obrocka, M., Stappers, B., & Wilkinson, P. 2015, A&A, 579, A69

Oppenheimer, J. R., & Volkoff, G. M. 1939, Physical Review, 55, 374

Oppermann, N., Junklewitz, H., Greiner, M., et al. 2015, A&A, 575, A118

Osten, R. A. 2008, ArXiv e-prints

Osten, R. A., & Bastian, T. S. 2008, ApJ, 674, 1078

Pacini, F. 1967, Nature, 216, 567

Pen, U.-L., & Connor, L. 2015, ApJ, 807, 179

Petroff, E., Bailes, M., Barr, E. D., et al. 2015a, MNRAS, 447, 246

Petroff, E., van Straten, W., Johnston, S., et al. 2014, ApJ, 789, L26

Petroff, E., Johnston, S., Keane, E. F., et al. 2015b, MNRAS, 454, 457

Petroff, E., Keane, E. F., Barr, E. D., et al. 2015c, MNRAS, 451, 3933

Petroff, E., Burke-Spolaor, S., Keane, E. F., et al. 2017, MNRAS, 469, 4465

Pick, M., Démoulin, P., Krucker, S., Malandraki, O., & Maia, D. 2005, ApJ, 625, 1019

Piro, A. L. 2016, ApJ, 824, L32

Popov, S. B., & Postnov, K. A. 2010, in Evolution of Cosmic Objects through their Physical Activity, ed. H. A. Harutyunian, A. M. Mickaelian, & Y. Terzian, 129–132

Radhakrishnan, V., & Cooke, D. J. 1969, Astrophys. Lett., 3, 225

Ravi, V., Shannon, R. M., & Jameson, A. 2015, ApJ, 799, L5

Ravi, V., Shannon, R. M., Bailes, M., et al. 2016, Science, 354, 1249

Rea, N., McLaughlin, M. A., Gaensler, B. M., et al. 2009, ApJ, 703, L41

Redman, S. L., Wright, G. A. E., & Rankin, J. M. 2005, MNRAS, 357, 859

Reich, P., & Reich, W. 1988, A&AS, 74, 7

Reynolds, S. P., Borkowski, K. J., Gaensler, B. M., et al. 2006, ApJ, 639, L71

Rickett, B. J. 1977, ARA&A, 15, 479

Robertson, J. G. 1991, Australian Journal of Physics, 44, 729

Robles, J. A., Lineweaver, C. H., Grether, D., et al. 2008, ApJ, 684, 691

S. Longair, M. 1992, High Energy Astrophysics (Cambridge University Press)

Savage, B. D., Kim, T.-S., Wakker, B. P., et al. 2014, ApJS, 212, 8

Scholz, P., Spitler, L. G., Hessels, J. W. T., et al. 2016, ApJ, 833, 177

Shannon, R. M., & Ravi, V. 2017, ApJ, 837, L22

Siemion, A. P. V., Bower, G. C., Foster, G., et al. 2012, ApJ, 744, 109

Spitler, L. G., Cordes, J. M., Hessels, J. W. T., et al. 2014, ApJ, 790, 101

Spitler, L. G., Scholz, P., Hessels, J. W. T., et al. 2016, Nature, 531, 202

Staveley-Smith, L., Wilson, W. E., Bird, T. S., et al. 1996, PASA, 13, 243

Taylor, A. R., Stil, J. M., & Sunstrum, C. 2009, ApJ, 702, 1230

Taylor, J. H., Fowler, L. A., & McCulloch, P. M. 1979, Nature, 277, 437

Tendulkar, S. P., Bassa, C. G., Cordes, J. M., et al. 2017, ApJ, 834, L7

Teukolsky, A. S., & Shapiro, L. S. 1983 (Wiley)

Thornton, D., Stappers, B., Bailes, M., et al. 2013, Science, 341, 53

Tingay, S. J., Trott, C. M., Wayth, R. B., et al. 2015, AJ, 150, 199

Totani, T. 2013, PASJ, 65, L12

Tsuruta, S. 1964, Neutron star models.

Ulrich, M.-H., Maraschi, L., & Urry, C. M. 1997, ARA&A, 35, 445

van Leeuwen, A. G. J., Kouwenhoven, M. L. A., Ramachandran, R., Rankin, J. M., & Stappers, B. W. 2002, A&A, 387, 169

van Paradijs, J., Kouveliotou, C., & Wijers, R. A. M. J. 2000, ARA&A, 38, 379

van Straten, W., Manchester, R. N., Johnston, S., & Reynolds, J. E. 2010, PASA, 27, 104

Vedantham, H. K., Ravi, V., Hallinan, G., & Shannon, R. M. 2016, ApJ, 830, 75

Wang, N., Manchester, R. N., & Johnston, S. 2007, MNRAS, 377, 1383

Weiler, K. W., Panagia, N., Montes, M. J., & Sramek, R. A. 2002, ARA&A, 40, 387

Weiler, K. W., Sramek, R. A., van der Hulst, J. M., & Panagia, N. 1982, in NATO Advanced Science Institutes (ASI) Series C, Vol. 90, NATO Advanced Science Institutes (ASI) Series C, ed. M. J. Rees & R. J. Stoneham, 281–291

Weisberg, J. M., Nice, D. J., & Taylor, J. H. 2010, ApJ, 722, 1030

Whiteoak, J. B. Z., & Green, A. J. 1996, A&AS, 118, 329

Widrow, L. M. 2002, Reviews of Modern Physics, 74, 775

Wild, J. P., Smerd, S. F., & Weiss, A. A. 1963, ARA&A, 1, 291

Williams, P. K. G., & Berger, E. 2016, ApJ, 821, L22

Wright, E. L. 2006, PASP, 118, 1711

Xu, J., & Han, J. L. 2015, ArXiv e-prints

Yao, J. M., Manchester, R. N., & Wang, N. 2017, ApJ, 835, 29

Zarka, P. 1998, J. Geophys. Res., 103, 20159

Zensus, J. A. 1997, ARA&A, 35, 607

Zheng, Z., Ofek, E. O., Kulkarni, S. R., Neill, J. D., & Juric, M. 2014, ApJ, 797, 71

Zhou, B., Li, X., Wang, T., Fan, Y.-Z., & Wei, D.-M. 2014, Phys. Rev. D, 89, 107303

Bibliography

Appendices and glossary of terms

A

The working of RMFIT

This is an updated model for estimating the change in position angle, $\Delta\Psi$, and its uncertainty. Let

$$P_k = Q_k + iU_k = L_k \exp i2\Psi_k \tag{A.1}$$

represent the linear polarization of the kth phase bin in one profile and

$$P'_k = Q'_k + iU'_k = L'_k \exp i2\Psi'_k \tag{A.2}$$

the same in the other profile.

Consider the **weighted** cross-correlation, $\bar{Z} = \bar{C} + i\bar{S}$, where $\bar{C}$ and $\bar{S}$ are the weighted mean values of the real and imaginary components of

$$z_k = c_k + is_k = P^*_k P'_k = L_k L'_k \exp i2(\Psi'_k - \Psi_k). \tag{A.3}$$

That is, where

$$c_k = Q_k Q'_k + U_k U'_k, \qquad s_k = Q_k U'_k - U_k Q'_k, \tag{A.4}$$

and

$$\sigma^2_{c_k} = Q'^2_k \sigma^2_{Q_k} + U'^2_k \sigma^2_{U_k} + Q^2_k \sigma^2_{Q'_k} + U^2_k \sigma^2_{U'_k} \tag{A.5}$$

$$\sigma^2_{s_k} = U'^2_k \sigma^2_{Q_k} + Q'^2_k \sigma^2_{U_k} + U^2_k \sigma^2_{Q'_k} + Q^2_k \sigma^2_{U'_k} \tag{A.6}$$

$$\sigma_{s_k c_k} = Q'_k U'_k (\sigma^2_{Q_k} - \sigma^2_{U_k}) + Q_k U_k (\sigma^2_{U'_k} - \sigma^2_{Q'_k}) \tag{A.7}$$

the weighted means and their variances and covariance are given by

$$\bar{C} = \sigma^2_{\bar{C}} \sum_{k=1}^{N} \frac{c_k}{\sigma^2_{c_k}} \qquad \bar{S} = \sigma^2_{\bar{S}} \sum_{k=1}^{N} \frac{s_k}{\sigma^2_{s_k}} \tag{A.8}$$

and

$$\sigma_{\bar{C}}^2 = \left[\sum_{k=1}^{N} \frac{1}{\sigma_{c_k}^2}\right]^{-1} \qquad \sigma_{\bar{S}}^2 = \left[\sum_{k=1}^{N} \frac{1}{\sigma_{s_k}^2}\right]^{-1}$$
$$\sigma_{\bar{S}\bar{C}} = \sum_{k=1}^{N} \left[\frac{\sigma_{\bar{S}}\sigma_{\bar{C}}}{\sigma_{s_k}\sigma_{c_k}}\right]^2 \sigma_{s_k c_k} \tag{A.9}$$

The expectation value of $\Delta\Psi = \Psi_k' - \Psi_k$ is given by

$$\langle \Delta\Psi \rangle = \frac{1}{2} \tan^{-1}\left(\frac{\bar{S}}{\bar{C}}\right). \tag{A.10}$$

and the variance of the expectation value

$$\mathrm{var}(\langle \Delta\Psi \rangle) = \frac{\bar{C}^2\sigma_{\bar{S}}^2 + \bar{S}^2\sigma_{\bar{C}}^2 + 2\bar{S}\bar{C}\sigma_{\bar{S}\bar{C}}}{\left(\bar{C}^2 + \bar{S}^2\right)^2} \tag{A.11}$$

B

Positional coordinates of FRBs 160317, 160410 and 160608

The coordinates of the FRB localisation ellipses in Figure 6.4 are given in Table B.1.

Table B.1 Sky coordinates of the 3 UTMOST FRBs. For each FRB, the first two columns are the J2000 right ascensions (RAs) and declinations (DECs) of the coordinates of the line defining the major axis of the 3σ FRB localisation contours in Figure 6.4, given in units of degrees. The third column gives the probability of the event occurring at this point along the localisation arc.

FRB 160317			FRB 160410			FRB 160608		
RA (hrs)	DEC (deg)	Prob.	RA (hrs)	DEC (deg)	Prob.	RA (hrs)	DEC (deg)	Prob.
7.9506	−33.4021	1.9217e−06	8.6857	2.3316	2.7070e−06	7.6531	−44.5497	3.8135e−06
7.9469	−33.1596	7.6284e−06	8.6859	2.5740	1.0085e−05	7.6502	−44.3073	1.3671e−05
7.9431	−32.9172	2.7612e−05	8.6861	2.8165	3.4461e−05	7.6473	−44.0648	4.5038e−05
7.9394	−32.6748	0.0001	8.6863	3.0589	0.0001	7.6445	−43.8224	0.0001
7.9358	−32.4324	0.0003	8.6865	3.3013	0.0003	7.6416	−43.5800	0.0004
7.9322	−32.1899	0.0008	8.6868	3.5437	0.0008	7.6388	−43.3376	0.0010
7.9286	−31.9475	0.0019	8.6870	3.7862	0.0020	7.6361	−43.0951	0.0023
7.9251	−31.7051	0.0043	8.6873	4.0286	0.0044	7.6334	−42.8527	0.0049
7.9217	−31.4627	0.0090	8.6876	4.2710	0.0089	7.6307	−42.6103	0.0098
7.9182	−31.2202	0.0171	8.6879	4.5134	0.0167	7.6281	−42.3679	0.0179
7.9148	−30.9778	0.0297	8.6882	4.7559	0.0286	7.6254	−42.1254	0.0300
7.9115	−30.7354	0.0470	8.6886	4.9983	0.0448	7.6229	−41.8830	0.0464
7.9082	−30.4930	0.0679	8.6890	5.2407	0.0645	7.6203	−41.6406	0.0658
7.9049	−30.2505	0.0897	8.6894	5.4831	0.0852	7.6178	−41.3982	0.0858
7.9017	−30.0081	0.1080	8.6898	5.7256	0.1033	7.6153	−41.1557	0.1029
7.8985	−29.7657	0.1188	8.6902	5.9680	0.1147	7.6128	−40.9133	0.1135
7.8954	−29.5233	0.1192	8.6906	6.2104	0.1169	7.6104	−40.6709	0.1150
7.8923	−29.2808	0.1093	8.6911	6.4528	0.1093	7.6080	−40.4285	0.1073
7.8893	−29.0384	0.0915	8.6915	6.6953	0.0937	7.6057	−40.1860	0.0919
7.8862	−28.7960	0.0699	8.6920	6.9377	0.0736	7.6033	−39.9436	0.0725
7.8832	−28.5536	0.0488	8.6925	7.1801	0.0531	7.6010	−39.7012	0.0525
7.8803	−28.3111	0.0311	8.6930	7.4225	0.0351	7.5987	−39.4588	0.0350
7.8774	−28.0687	0.0181	8.6936	7.6649	0.0213	7.5965	−39.2163	0.0215
7.8745	−27.8263	0.0096	8.6941	7.9074	0.0118	7.5942	−38.9739	0.0121
7.8717	−27.5839	0.0047	8.6947	8.1498	0.0060	7.5920	−38.7315	0.0063
7.8689	−27.3414	0.0021	8.6953	8.3922	0.0028	7.5899	−38.4891	0.0030
7.8661	−27.0990	0.0008	8.6959	8.6346	0.0012	7.5877	−38.2467	0.0013
7.8634	−26.8566	0.0003	8.6966	8.8771	0.0005	7.5856	−38.0042	0.0005
7.8607	−26.6142	0.0001	8.6972	9.1195	0.0002	7.5835	−37.7618	0.0002
7.8580	−26.3717	3.2671e−05	8.6979	9.3619	0.0001	7.5814	−37.5194	0.0001
7.8554	−26.1293	9.2354e−06	8.6985	9.6043	1.7269e−05	7.5794	−37.2770	2.0978e−05
7.8528	−25.8869	2.3859e−06	8.6992	9.8468	4.8054e−06	7.5774	−37.0345	6.0539e−06
7.8503	−25.6445	5.6329e−07	8.7000	10.0892	1.2261e−06	7.5754	−36.7921	1.6069e−06